國 立 交 通 大 學

光電工程學系
博 士 論 文

陽極氧化鋁薄膜基板及具溝槽之 PDMS 基板

用於液晶配向及其配向特性之研究

Study on the Alignment Properties of Liquid Crystal

on the Substrate with Anodic Aluminum Oxide Films

and the Grooved PDMS Substrate

研 究 生：湯宗達

指導教授：潘犀靈　教授

趙如蘋　教授

中 華 民 國 九 十 八 年 九 月

陽極氧化鋁薄膜基板及具溝槽之 PDMS 基板
用於液晶配向及其配向特性之研究

Study on the Alignment Properties of Liquid Crystal
on the Substrate with Anodic Aluminum Oxide Films
and the Grooved PDMS Substrate

研 究 生：湯宗達

指導教授：潘犀靈 教授

趙如蘋 教授

Student: Tsung-Ta Tang

Advisors: Prof. Ci-Ling Pan

Prof. Ru-Pin Pan

國 立 交 通 大 學

光 電 工 程 學 系

博 士 論 文

A Thesis

Submitted to Department of Photonics and Institute of Electro-Optical Engineering

College of Electrical Engineering and Computer Science

National Chiao Tung University

in Partial Fulfillment of the Requirements

for the Degree of Doctor of Philosophy

in

Photonics

September 2009

Hsinchu, Taiwan, Republic of China

中 華 民 國 九 十 八 年 九 月

陽極氧化鋁薄膜基板於液晶配向
及其配向特性之研究

學生：湯宗達　　　　　　　　　　　　　指導教授：潘犀靈教授
　　　　　　　　　　　　　　　　　　　　　　　　趙如蘋教授

國立交通大學光電工程學系博士班

中文摘要

液晶顯示器為目前市面上最為廣泛使用的顯示器。為了提供液晶分子在未驅動狀態下能夠整齊排列，通常使用傳統的磨刷聚亞醯胺薄膜作為液晶配向薄膜。由於傳統磨刷方式會產生靜電殘留、雜質顆粒污染及損壞驅動薄膜電晶體，且聚亞醯胺薄膜容易被強背光模組中的紫外光波段改變其配向特性。因此研究新穎的非接觸式配向法或無機的配向材料是最為迫切的研究主題。

本論文利用具多孔性的陽極處理氧化鋁薄膜做為液晶顯示元件的配向膜。陽極處理氧化鋁薄膜為一種無機且具有奈米孔洞陣列的透明薄膜。利用表面結構的液晶配向機制，此陽極處理氧化鋁薄膜具有很高的潛能可以作為液晶顯示元件的配向膜。本論文成功利用此一薄膜使液晶分子產生垂直配向。利用改變陽極處理電壓進而改變薄膜上之奈米孔洞大小，此薄膜之極角錨定強度也隨之改變。其極角錨定強度約為 15×10^{-6} J/m^2，約略小於傳統的垂直配向膜 DMOAP 之極角錨定強度 38×10^{-6} J/m^2。

除了改變奈米孔洞大小外，本論文中也利用蝕刻一次陽極處理氧化鋁薄膜並控制蝕刻時間，得到具有相同孔洞密度且具有不同孔洞寬深比之奈米孔洞陣列。由實驗發現具有較高寬深比之奈米孔洞陣列可以提供較大的極角錨定強度。此外在特定蝕刻時間下所產生的陽極處理氧化鋁薄膜可提供液晶分子水平配向能力。關於此一現象之配向機制，更多的研究及探討仍須進行。

此外利用兆赫波時域分析系統，對於陽極處理氧化鋁薄膜的光學特性，包括折射率與吸收特性進行分析。本論文研發一套配合兆赫波時域分析系統的光學係數分析程式。利用此程式可直接由兆赫波時域訊號計算出待測物的折射率及吸收

特性，並大幅消除待測物所造成的多重反射雜訊。陽極處理氧化鋁薄膜的折射率會隨孔洞密度而改變且在兆赫波波段並沒有明顯的吸收峰。因此陽極處理氧化鋁薄膜也適合作為兆赫波下液晶元件的配向薄膜。

雖然水平錨定強度對於垂直樣品並不是指標參數，但本論文也討論對於水平錨定強度的量測修正。利用量測楔形樣品的強度變化條紋所計算出來之旋性液晶週期，來計算水平錨定強度可大幅減少因雙折射係數所造成的誤差由 10% 至 1%。

除了利用多孔洞陽極處理氧化鋁薄膜作為垂直配向薄膜，本論文也嘗試使用奈米壓印技術，於 PDMS 基板上轉印出 U 型微溝槽結構，並使用氧電漿作表面改質作為水平配向薄膜。此一方式可以成功製作出可橈式的配向基板。

最後本論文已經成功嘗試將陽極處理氧化鋁薄膜製作於 ITO 透明導電薄膜上，並製作出可電控的液晶顯示元件。未來可以利用此一方式來製作以陽極氧化鋁薄膜作為配向膜之元件，並量測其電性反應或利用外加電場來量測其極角錨定強度。

Study on the Alignment Properties of Liquid Crystal
on the Substrate with Anodic Aluminum Oxide Films

Student: Tsung-Ta Tang

Advisors: Prof. Ci-Ling Pan

Prof. Ru-Pin Pan

Doctor of Philosophy in Department of Photonics and
Institute of Electro-optical Engineering
National Chiao-Tung University

Abstract

In the past decades, the liquid crystal displays (LCDs) have been widely used in different applications. The rubbed polyimide thin film is the most common alignment layer for aligning liquid crystal without any applied field. The rubbing method usually introduces the static charge, dust contamination, and damages the driving thin-film transistors (TFT) devices. Because of the chemical structure of the polyimide, it is easy to be modified by the UV-light or the back light module. Therefore, the novel alignment method, which is non-contact and uses the inorganic alignment material, is desired.

In this thesis, the porous anodic aluminum oxide (AAO) thin film is used as the alignment layer of the LCDs. The AAO thin film is an inorganic and transparent thin film with nanopores array. Because of the nanopores array, the AAO thin film is an excellent candidate of the alignment layer. By controlling the anodizing voltage, the pore diameter of the AAO thin film can be varied between 15 nm and 65 nm, and the polar anchoring strength can also be modified. The polar anchoring strength of the AAO thin film is around 15×10^{-6} J/m^2, which is smaller than one of the DMOAP, 38×10^{-6} J/m^2.

Besides controlling the anodizing voltage and changing the pore diameter, the one-step AAO thin film can be etched with different etching time. Because the etching solution etches both the top and the wall of the AAO thin film, the etched AAO thin film has different aspect ratio with the same pore density. The AAO thin

film with higher aspect ratio has the higher polar anchoring strength. In some specific etching time, the etched AAO thin film performs as a homogenous alignment layer. Further works are progressing to understand the mechanism of the homogenous alignment on the etched AAO thin film.

The optical properties of the AAO thin film, such as the complex refractive constants and the attenuation constant, are investigated by using the Terahertz Time-Domain Spectroscopy (THz-TDS). The optical constants analysis program is developed for calculating the optical constants by analyzing the time-domain signal directly. The multiple reflections have been considered in the program to cancel out the Febry-Perot effect. The refractive constant of the AAO thin film depends on the pore density of the AAO thin film. There is no obvious absorption peak in THz region. Therefore, the AAO thin film is suitable for THz application.

Although the azimuthal anchoring strength is not an important indication of the vertical alignment cell, it is also discussed in this thesis. The pitch value used in calculating the azimuthal anchoring strength can be modified by counting the fringes of the wedge cell. By using the modified pitch value, the error of the azimuthal anchoring strength can be reduced from 10% to 1%.

On the other hand, the grooved PDMS substrates are used as the homogenous alignment substrates. The PDMS substrates with the U-shape groove are imprinted by the nanoimprinting technology, and then treated by O_2 plasma to change the surface property. The flexible LCDs are demonstrated by using the grooved PDMS substrates as the alignment substrates.

Finally, the prototypical electrically controllable LCDs with the AAO thin film as the alignment layer have been demonstrated in this thesis. In the future, the electric performance and the polar anchoring strength can be measured by applying the electric field.

誌　　謝

Table of Contents

List of Figures

xiii

List of Tables

Chapter 1
Introduction

1.1 Liquid crystals

In the fundamental physics, such as high school physics or university physics, everyone has been taught that substance only exists three phases: solid, liquid, and gas. In particular, some organic materials do not show a single transition from solid phase to liquid phase. The mechanical and the symmetry properties of these new phases are intermediate between those of a liquid and those of a solid. Therefore, these new phases are often called "*liquid crystals*". Liquid crystals can be divided into three different phase depending on the physical properties, such as thermotropic, lyotropic and metallotropic phases. The thermotropic liquid crystals exhibit a phase transition into the liquid crystal phase as temperature is changed. The phase transition of the lyotropic liquid crystals depends on both temperature and concentration of the liquid crystal molecules in a solvent, such as water. Most of the thermotropic and lyotropic liquid crystals consist of organic molecules. The metallotropic liquid crystals are composed of not only organic but also inorganic molecules. The liquid crystal transition of the metallotropic liquid crystal depends not only on temperature and concentration, but also on the inorganic-organic composition ratio.

According to the different arrangement of liquid crystal molecules, the thermotropic liquid crystals can also be distinguished into three different types: nematic, smectic, and cholesteric. Figure 1-1 shows the schematic of liquid crystal alignment in these three different phases. In the nematic phase, the liquid crystal molecules have no positional order, but have long-range orientational order. Therefore, the center of mass positions of the liquid crystal molecules are randomly distributed as a liquid, but they all point to the same direction. The smectic phase usually forms several well-defined layers, and is usually found at

lower temperature than the nematic phase. There are many different smectic phases. All of these smectic phases are characterized by different types and degrees of positional and orientational order. [1] The cholesteric phase, also called the chiral nematic phase, exhibits chirality or handedness. The first cholesteric phase was observed for cholesterol derivatives. Most of the liquid crystals which have the cholesteric phase are chiral molecules that are without inversion symmetry.[1] In this work, nematic liquid crystal is used in most of our experiment.

The well arrangement of the anisotropic rodlike molecules directly results in the anisotropy of mechanical, electric, magnetic, and optical properties. In the liquid crystal displays applications, the most important anisotropic properties are the optical and electric properties. As a result of the orientational ordering of the nematic liquid crystals molecules, the nematic liquid crystals are uniaxial with the symmetric axis parallel to the axes of the molecules, called the director $\hat{n}$. Because of the uniaxial symmetry, the dielectric constants are different in value parallel to ($\varepsilon_{//}$) and perpendicular to ($\varepsilon_{\perp}$) the director. The dielectric anisotropy is defined as

$$\Delta\varepsilon = \varepsilon_{//} - \varepsilon_{\perp}.$$
(1-1)

The sign and magnitude of the dielectric anisotropy are both important in liquid crystal displays application by using the various electric fields to control the liquid crystal displays. Usually, the macroscopic dielectric constant is often proportional to the molecular polarizability. For the rodlike molecules, such as the nematic liquid crystal molecules, the longitudinal polarizability (parallel to molecular axis) is often larger than the transverse polarizability (perpendicular to axis). Most of the rodlike molecules have induced dipole in the applied electric field. Because the induced dipole is parallel to the director, the dielectric anisotropy is positive, $\Delta\varepsilon > 0$, and $\varepsilon_{//} > \varepsilon_{\perp}$. *4`-n*-pentyl-*4*-cyanobiphenyl (5CB) is one of the most common positive nematic liquid crystals in literatures.[2] Some

polar liquid crystal compounds have the permanent dipole moment. Depending on the angle between the permanent dipole moment and the molecular axis, the additional contributions increase or decrease the dielectric constant. The increase or decrease of the dielectric anisotropy $\Delta \varepsilon$ results in the negative value of the dielectric anisotropy, called the negative liquid crystals (e.g., *p*-Methoxybenzylidene-*p*`-*n*-butylaniline, MBBA).[1] The dielectric anisotropy also depends on the temperature. $\varepsilon_{//}$ and $\varepsilon_{\perp}$ approaches to each other near the clearing point T_c. Beyond the clearing point, the dielectric constant becomes the mean dielectric constant

$$\bar{\varepsilon} = \frac{\varepsilon_{//} + 2\varepsilon_{\perp}}{3}.$$

(1-2)

Figure 1-2 shows the characteristic of the dielectric constants for 5CB.[3] Here, $\bar{\varepsilon}$ is calculated from the measured values of $\varepsilon_{//}$, $\varepsilon_{\perp}$ and Equation (1-2). The dashed line denotes the extrapolated value of the dielectric anisotropy in isotropic state, ε_{iso}.[4]

On the other hand, the nematic liquid crystals also show the anisotropic properties in optical region, called the optical anisotropy. Without proper boundaries or the applied field (magnetic field or electric field), the directors and the refractive index of liquid crystal molecules are random, and the incident light is scattered. Because of the discontinuity of the refractive indices at the domain boundaries, the nematic liquid crystals usually appear as a milky fluid. A nematic liquid crystal cell with the proper treated alignment layers exhibits the optical properties as an uniaxial crystal with two principal refractive indices n_o and n_e. The ordinary refractive index n_o is for light with the polarization of the electric field perpendicular to the director. The extraordinary refractive index n_e is for light with the polarization of the electric field parallel to the director. The optical anisotropy, also called the birefringence, is defined as

$$\Delta n = n_e - n_o .$$

(1-3)

If $\Delta n > 0 \Rightarrow n_e > n_o$, the liquid crystal has positive birefringence, whereas if $\Delta n < 0 \Rightarrow n_e < n_o$, the liquid crystal has negative birefringence. For most liquid crystals, the ordinary refractive index n_o is around 1.5, and the birefringence is from 0.05 to 0.45. This optical anisotropy plays an essential role in changing the polarization state of light in liquid crystals. Figure 1-3 shows the characteristic of n_e, n_o and Δn of 5CB.[5] It clearly shows the similar behavior as the dielectric constants. It is because that the refractive index is also related to the molecular polarizability at optical frequencies and the anisotropic molecular structure.

1.2 Liquid crystal display applications

In liquid crystal display applications, the liquid crystal molecules are usually sandwiched between two substrates coating with the alignment layers. Depending on different alignment layers, the liquid crystal molecules orient homogenously or homeotropically. Figure 1-4 shows the typical orientations of liquid crystal molecules in different liquid crystal displays. The liquid crystal molecules align parallel to the substrates in the homogenous cell and perpendicular to the substrates in the homeotropic cell. For the twist nematic cell, the directors of the liquid crystal molecules near two substrates are different, one with 90° respect to another. In the hybrid cell, the liquid crystal molecules on one substrate have homogenous alignment and those on the other substrate have homeotropic alignment. The homogenous alignment can be obtained by rubbing polyimide films, photoalignment method and using the microgrooved substrates. The homeotropic alignment can be obtained by coating the substrate with hydrophobic films such as silane compounds or the ferromagnetic film. The SiO oblique evaporation method can give any of the homogenous, homeotropic and tilted alignments by controlling the evaporation angle. All of these alignment methods

will be introduced in the following sections.

1.3 Rubbing alignment method

In the 70s, the early stages of liquid crystal displays production, only the rubbing method has been adopted for alignment technologies. The rubbing alignment method is a simple, convenient, and low-cost method. A typical rubbing machine includes a rolling cylinder covered by the rubbing cloth and a substrate holding stage. The cylinder rotates 100-800 rpm, and can be controlled to move up and down relative to the substrate stage. The glass substrates with alignment layers are fixed to the stage by using air suction. By rotating the angle of the substrate on the stage, the rubbing direction on the alignment layer can be controlled. The rotating cylinder moves down to the substrate and applies pressure to the substrate. Then, the substrate stage moves forward with a constant velocity. After the entire area is rubbed, the cylinder moves away and the substrate stage returns to the initial position.[6]

However, when the production of the thin film transistors liquid crystal displays (TFT-LCDs) started in the 80s, defects of the rubbing method were highlighted. In the rubbing method, the surface of polyimide layers is rubbed with a cloth. Several problems were pointed out: (a) the TFTs are destroyed by the static electricity caused by the friction between the surfaces of the cloth and the polyimide layers, (b) the direct contact between the surfaces and the cloth causes defects and stains on the surface of alignment layer, and (c) the clean room is polluted by fiber from the cloth.

1.4 Photoalignment method

The photoalignment method is a non-contact method for liquid crystal alignment. The non-contact method can prevent a lot of problems which are produced from the rubbing process, such as the static electricity and dust. The

most common photoalignment method is the alignment method by generating the anisotropic distribution of the molecules of the alignment materials using the polarized light irradiated on the alignment layer. In 1991, W. M. Gibbons et al. presented the photoalignment method that the liquid crystal molecules were aligned by using the polarized laser light in visible range.[7] The photochemical reactions of the photoalignment method can be categorized as photoisomerization, photodimerization, photodecomposition, photocrosslinking and a combination of photodecomposition and photolinking. By using the conformational change between cisoid-type and transoid-type azobenzene functional units, the photoisomerization reaction can control the liquid crystal alignment.[8] It is a reversible change between homeotropic and homogenous alignment by controlling the wavelength or the polarization of the irradiated light.[9]

Polyvinyl cinnamate (PVCi) is a well-known material that aligns liquid crystal molecules by photodimerization process.[10][11] PVCi absorb the energy of the irradiated linear polarization light which polarization axis is parallel to the double bonds of PVCi. The double bonds are scissored and then two of the scissored bonds are reconnected and dimerized. The alignment direction of the liquid crystal molecules is perpendicular to the polarization of the light for PVCi.

The photodecomposition reaction has been applied to a various photosensitive materials compared with the other two methods, photoisomerization and photodimerization. Polyimide has been used as a photodecomposition material. The anisotropic photodecomposition of polyimide by irradiating the polarized UV light changes the anisotropic molecular length distribution. The distribution can control the alignment of liquid crystal molecules.

By irradiating the UV light, the crosslinking process connects one molecule to another molecule and generates a new structure. This new structure can be used to align the liquid crystal molecules. Some of photodecomposition material not only break bonds and create new structures, but also connect these structures and

become a new anisotropic alignment structure. This process is called the Hybird method (photocomposition and photocrosslinking). However, the photoalignment mechanisms in some material are not clearly understood because the photochemical reactions are different in each photoalignment material.

1.5 Ion beam bombardment method

The ion beam bombardment method is another novel non-contact alignment method. It is developed only in the past decade. In 1998, an IBM research group invented that the liquid crystal molecules can be aligned on the polyimide or diamond-like carbon (DLC) alignment layer which is bombarded by a low energy and neutral argon ion beam.[12][13] Recently, Stöhr et al. discovered that the ion beam bombardment changes the carbon double or triple bonds. This anisotropic change introduces the surface orientational anisotropy.[14] Any amorphous layer with directional sp^2 and sp bonds, such as SiN_x, SiC, SiO_2, SnO_2, $ZnTiO_2$ and $InTiO_2$, can align the liquid crystal.

During the past few years, the most remarkable research about the ion beam bombardment is that the homeotropic alignments can be obtained by using fluorinated DLC thin films as the alignment layer. The pretilt angle can also be controlled by the different parameters of the ion beam and the concentration of fluorine doped in DLC thin films.[15] On the other hand, by using the ion beam with different energies, both homeotropic and homogenous alignment can be applied on the same organic alignment layer.[16][17]

Recently, our group has developed a novel alignment method by using ion beam bombardment on different alignment materials. We have demonstrated that both homeotropic and homogenous alignments can be obtained with the same ion beam apparatus and polyimide by varying the ion beam energy or the bombarding time.[18] Another alignment method is by using a one-step, ion beam bombardment of the glass substrates without polyimide layer. The homeotropic

alignment is achieved due to orientation of the diamagnetic nematogenic molecules by the magnetic field from the γ-Fe_2O_3 ferrimagnetic thin films created on the substrates by ion beam bombardment. This is a simple, noncontact, and reliable alignment method for liquid crystal devices.[19][20]

1.6 Chemical treatment method

After chemically treating the substrates, the substrates can provide the homeotropic or homogenous alignment. The surface active agents, such as silicone compounds, are used to obtain homeotropic alignment. The silicon compounds react with the substrate surface and polymerize to form polysiloxane structures near the surface. *N*, *N*-dimethyl-*N*-octadecyl-3-amino-propyl -trimeth oxysilyl chloride (DMOAP) is usually used to homeotropic alignment. The surface treatments with DMOAP are carried out by dipping the substrate into a 1% aqueous solution of the silane compounds, DMOAP. There are other methods to treat the surface of substrate. By exposing the substrate to the vapor of pure silane compounds or spreading silane compounds on the surface, the surface can be treated and become the homeotropic alignment surface. In 1973, F. J. Kahn investigated the alignment properties of N-methyl-3-amino-propyl -trimethoxy-silane (MAP) and DMOAP.[32] Figure 1-5 shows the names and the chemical formulas of DMOAP and MAP. The schemes also represent the orientations of their components propyl $(CH_2)_3$ and octadecyl $(C_{18}H_{37})$. For DMAOP with long alkyl chains, the propyl chain attaches on the substrate surface and the octadecyl chain orients out of plane. The liquid crystal molecules can align along the octadecyl chain. It is the most used vertical alignment method.

1.7 Other alignment method

Besides the rubbing method, the photoalignment method and the ion beam bombardment method, there are some other alignment method, such as the

oblique evaporation method and the microgroove surface method. SiO is the most common material used in the oblique evaporation method. After the oblique evaporation process, the micro SiO columnar structure is formed on the substrate surface. The columnar angle is dependent on the evaporation angle and changes in the nematic alignment direction and the pretilt angle.[21]

For the microgroove surface method, our group has demonstrated that the liquid crystal molecules can be aligned on the U-shaped grooves surface formed on the substrate with variable depths and spacing by using the reactive ion etching (RIE) method. [22] The periods of grooves were varied from 2 μm to 9 μm with three different depths by changing the etching time in the RIE process. The anchoring strengths are within the range of $1 \times 10^{-8} \sim 2 \times 10^{-6}$ J/m^2. It can be increased by more than an order of magnitude by varying the groove depth and period.

1.8 Mechanism of liquid crystal alignment

As what we have discussed, the alignment layer is necessary for the liquid crystal displays application to align the liquid crystal molecules without any applied field. The major mechanisms for the alignment of liquid crystals on the alignment layer, such as the rubbed polymer film, are the micro-morphology of the alignment surface and the interaction force between the liquid crystal molecules and the alignment molecules. The mechanism of the micro-morphology was suggested by D. W. Berreman.[23] He mentioned that the liquid crystal molecules prefer to align parallel to the induced grooves to reduce the total surface free energy. Here we review his calculations as following. The groove surface can be approximately described by a sinusoidal wave $z \approx A\sin(qx)$ where A is the depth of the groove on the surface and $\lambda = 2\pi/q$ is the frequency of the groove. The anchoring energy can be calculated by using the elastic energy based on the Oseen-Frank elastic continuum theory.[24][25] The

azimuthal anchoring energy W_ϕ calculated as $W_\phi = \frac{1}{4} K_{11}(Aq)^2 q$. Here, K_{11} is a splay elastic constant of the liquid crystal.

On the other hand, J. M. Geary et al. suggested that liquid crystal molecules are anchored to buffed polymer chains of the polymer surfaces. The alignment of the liquid crystal molecules follows in an epitaxial manner.[26] The reorientation of polymers which gives the anisotropic characteristics caused by rubbing have been confirmed by optical retardation, IR absorption spectra and second harmonic generation. In view of problems mentioned above, studies on both the mechanism of the rubbing process and the development of other methods for liquid crystalline alignment have been carried out. Thus, novel alignment technologies are required that not only achieve increase in production yields, but also offer additional advantages, such as the convenience of multi-domain alignment.

1.9 Overview of this work

In this work, we develop two novel alignment methods based on the micro-morphology mechanism. The first alignment method is a novel vertical alignment method which is by using the porous anodic aluminum oxide (AAO) thin film as the alignment layer. The porous AAO thin film is formatted by anodizing the aluminum thin film in the acidic electrolyte. The detailed manufacture process is described in Appendix A. The morphology of porous AAO thin film surface is a nanopores array. It offers the liquid crystal molecules an excellent vertical alignment layer. The second alignment method is a homogenous alignment method on the grooving surface by using the nanoimprinting method.

In Chapter 2 and Chapter 3, we demonstrate the strong vertical alignment of liquid crystal on porous AAO thin film and also discuss the polar anchoring strength of the AAO thin film with different pores sizes and different aspect ratio, respectively. In detail, the measuring method of the polar anchoring strength by

using the magnetic field method is described in Appendix B.

In the past few years, our group has studied the optical constants of the liquid crystals in terahertz region[27][28] and developed several terahertz devices, such as the electrically controlled quarter and full wave plate[29][30] and the magnetically controlled phase shifter[31], based on the liquid crystal devices. In order to apply the AAO thin film as an alignment layer in terahertz region, we investigate the optical properties of the AAO thin film by using the terahertz time-domain spectroscopy in Chapter 3.

In Chapter 5, we demonstrate the preliminary work about the homogenous alignment on the flexible polydimethylsiloxane (PDMS) substrate. Here we use the glass substrates with the U-shaped groove as the imprinting mode. By using the nanoimprinting technology, the U-shaped groove can be imprinted on PDMS substrate. After O_2 plasma treatment, the nematic liquid crystal can be aligned homogenously on the PDMS surface and parallel to the groove direction.

In order to investigate the homogenous alignment ability in the previous chapter, the azimuthal anchoring strength is a physical parameter to indicating the ability of the alignment layer. In Chapter 6, we develop a novel method to measure the pitch of the chiral nematic liquid crystal. By using this modified pitch to calculate the azimuthal anchoring strength, the error of the azimuthal anchoring strength can be reduced and become less than 1%.

Finally, in Chapter 7, we summarize all remarkable conclusions about each novel alignment method discussed in this thesis. Furthermore, we provide some interesting research topics for future work.

References

[1] P. G. de Gennes, and J. Prost, "*The Physics of Liquid Crystals*," Oxford University Press, ISBN 0-19-852024-7 (1994).

[2] L. M. Blinov, and V. G. Chigrinov, "*Electrooptic Effects in Liquid Crystal Materials*," Springer-Verlag New York, ISBN 0-387-94030-8 (1994).

[3] S. Chandrasekhar, "*Liquid Crystals*," 2nd Ed., Cambridge University Press, ISBN 0-521-42741-X (1992).

[4] B. R. Ratina, and R. Shashidhar, "Dielectric properties of *4`-n*-alkyl-*4*-cyanobiphenyls in their nematic phases," *Pramana* **6**, 278 (1976).

[5] R. G. Horn, "Refractive indices and order parameters of two liquid crystals," *J. Phys. France* **39**, 105 (1978).

[6] T. Uchida, M. Hirano, and H. Sakai, "Director orientation of a ferroelectric liquid crystal on substrates with rubbing treatment: The effect of surface anchoring strength," *Liquid Crystals* **5**, 1127 (1989).

[7] W. M. Gibbons, P. J. Shannon, S. T. Sun, and B. J. Swetlin, "Surface-mediated alignment of nematic liquid crystals with polarized laser light," *Nature* **351**, 49 (1991).

[8] Y. Kawanishi, T. Tamaki, M. Sakyragi, T. Seki, Y. Suzuki, and K. Ichimura, "Photochemical induction and modulation of nematic homogenous alignment by the polarization photochromism of surface azobenzenes," *Langmuir* **8**, 2601 (1992).

[9] K. Ichimura, Y. Suzuki, T. Seki, A. Hosoki, and K. Aoki, "Reversible change in alignment mode of nematic liquid crystals regulated photochemically by command surfaces modified with an azobenzene monolayer," *Langmuir* **4**, 1214 (1988).

[10] M. Schadt, K. Schmitt, V. Kozinkov, and V. Chigrinov, "Surface-induced

parallel alignment of liquid crystals by linearly polymerized photopolymers," *Jpn. J. Appl. Phys.* **31**, 2155 (1992).

[11] Y. Iimura, T. Saitoh, S. Kobayashi, and T. Hashimoto, "Liquid crystal alignment on photopolymer surfaces exposed by linearly polarized UV light," *J. Photopolymer Sci. and Tech.* **8**, 257 (1995).

[12] P. Chaudhari, J. Lacey, S. C. Alan Lien, and J. L. Speidell, "Atomic beam alignment of liquid crystals," *Jpn. J. Appl. Phys.* **37**, L55 (1998).

[13] P. Chaudhari, J. Lacey et al., "Atomic-beam alignment of inorganic materials for liquid-crystal displays," *Nature* **411**, 56 (2001).

[14] J. Stöhr, M. G. Samant, J. Lüning, A. C. Callegari, P. Chaudhari, J. P. Doyle, J. A. Lacey, S. A. Lien, S. Purushothaman, and J. L. Speidell, "Liquid crystal alignment on carbonaceous surfaces with orientational order," *Science* **292**, 2299 (2001).

[15] H. J. Ahn, S. J. Rho, K. C. Kim, J. B. Kim, B. H. Hwang, C. J. Park, and H. K. Baik, "Ion-beam induced liquid crystal alignment on diamond-like carbon and fluorinated diamond-like carbon thin films," *Jpn. J. Appl. Phys.* **44**, 4092 (2005).

[16] J. S. Gwag, K. H. Park, J. L. Lee, J. C. Kim, and T. H. Yoon, "Two-domain hybrid-aligned nematic cell fabricated by ion beam treatment of vertical alignment layer," *Jpn. J. Appl. Phys.* **44**, 1875 (2005).

[17] S. H. Lee, K. H. Park, J. S. Gwag, T. H. Yoon, and J. C. Kim, "A multimode-type transflective liquid crystal display using the hybrid-aligned nematic and parallel-rubbed vertically aligned modes," *Jpn. J. Appl. Phys.* **42**, 5127 (2003).

[18] H. Y. Wu, T. T. Tang, C. C.Wang, R. P. Pan, S. J. Chang, and J. C. Hwang, "Controllable alignment modes of nematic liquid crystals on argon ion beam bombarded polyimide films," *Mol. Cryst. Liq. Cryst.* **475**, 45 (2007).

[19] H. Y. Wu, and R. P. Pan, "Liquid crystal surface alignments by using ion beam sputtered magnetic thin films," *Appl. Phys. Lett.* **91**, 074102 (2007).

[20] R. P. Pan, H. Y. Wu, and C. F. Hsieh, "Liquid crystal surface alignment by using films composed of magnetic nanoparticles," *Proc. SPIE* **6911**, 691104 (2008).

[21] J. L. Janning, "Thin film surface orientation for liquid crystals," *Appl. Phys. Lett.* **21**, 173 (1972).

[22] Y. F. Lin, M. C. Tsou, and R. P. Pan, "Alignment of liquid crystals by ion etched grooved glass surfaces," *Chinese J. Phys.* **43**, 1066 (2005).

[23] D. W. Berreman, "Solid surface shape and the alignment of an adjacent nematic liquid crystal," *Phys. Rev. Lett.* **28**, 1683 (1972).

[24] C. W. Oseen, "The theory of liquid crystals," *Trans. Faraday Soc.* **29**, 883 (1933).

[25] F. C. Frank, "I. Liquid crystals. On the theory of liquid crystals," *Discuss. Faraday Soc.* **25**, 19 (1958).

[26] J. M. Geary, J. W. Goodby, A. R. Kmetz, and J. S. Patel, "The mechanism of polymer alignment of liquid-crystal materials," *J. Appl. Phys.* **62**, 4100 (1987).

[27] T. R. Tsai, C. Y. Chen, C. L. Pan, R. P. Pan, and X. C. Zhang, "Terahertz Time-Domain Spectroscopy Studies of the Optical Constants of the Nematic Liquid Crystal 5CB," *Appl. Opt.* **42**, 2372 (2003).

[28] R. P. Pan, T. R. Tsai, C. Y. Chen, and C. L. Pan, "Optical constants of two typical liquid crystals 5CB and PCH5 in the THz frequency range", *J. Bio. Phys.* **29**, 335 (2003).

[29] C. F. Hsieh, R. P. Pan, T. T. Tang, H. L. Chen, and C. L. Pan, "Voltage-controlled liquid-crystal terahertz phase shifter and quarter-wave plate," *Opt. Lett.* **31**, 1112 (2006).

[30] H. Y. Wu, C. F. Hsieh, T. T. Tang, R. P. Pan, and C. L. Pan, "Electrically tunable room-temperature 2π liquid crystal terahertz phase shifter", *IEEE Phtonics Tech. Lett.* **18**, 1488 (2006).

[31] C. Y. Chen, T. R. Tsai, C. L. Pan, and R. P. Pan, "Room temperature

terahertz phase shifter based on magnetically controlled birefringence in liquid crystals," *Appl. Phys. Lett.* **83**, 4497 (2003).

[32] F. J. Kahn, "Orientation of liquid crystals by surface coupling agents," *Appl. Phys. Lett.* **22**, 386 (1973).

Figures

| Nematic | Smectic | Cholesteric |
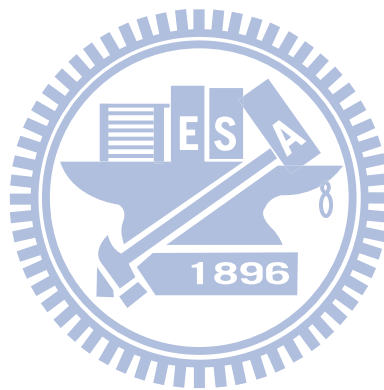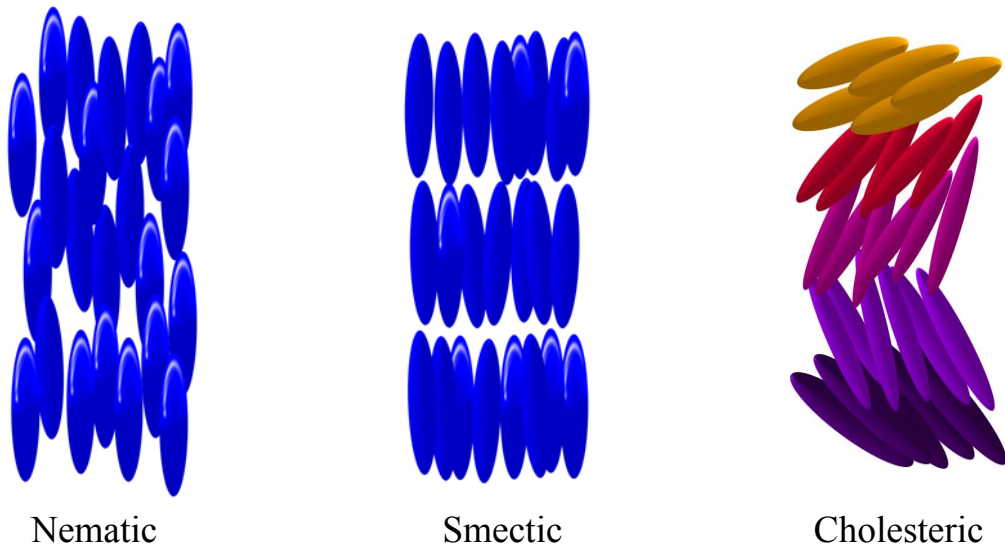
Figure 1-1 Scheme of different type of liquid crystal.
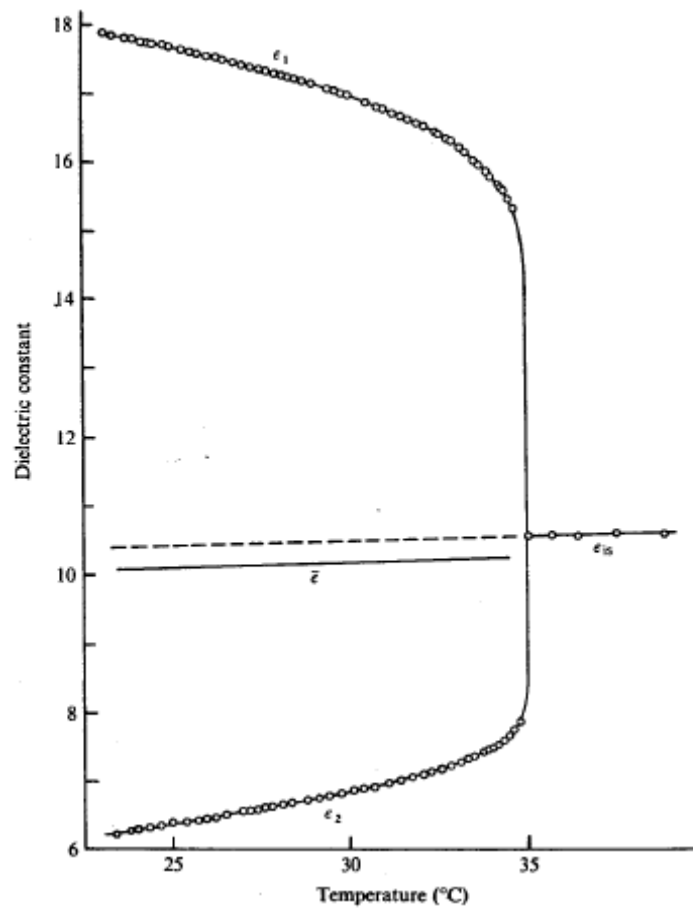
Figure 1-2 Characteristic of the dielectric constant of 5CB. [3]
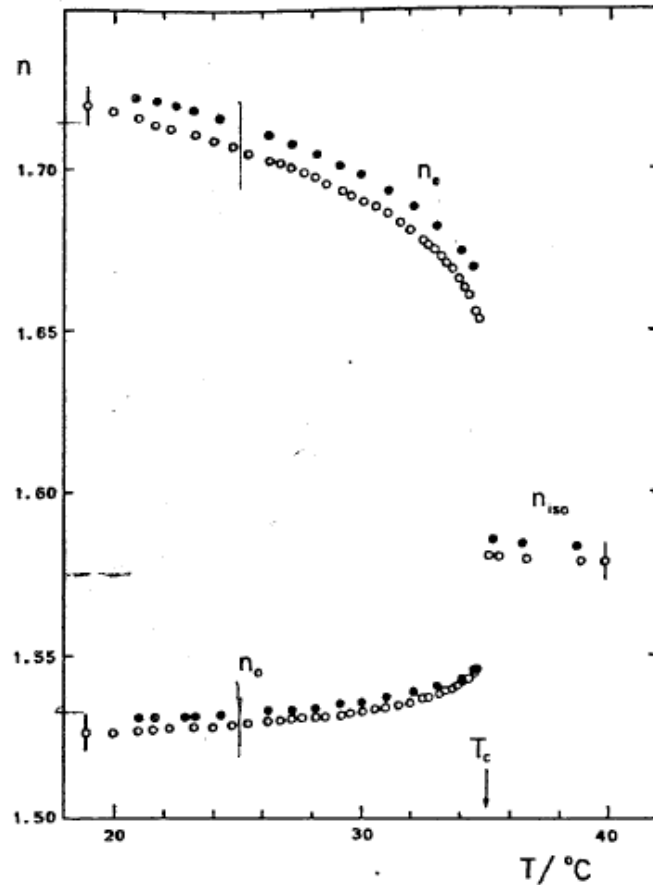
Figure 1-3 Characteristic of the ordinary refractive index, the extraordinary refractive index and the birefringence of 5CB. ● is for 589 nm, and ○ is for 632.8 nm. Tc is the cleaning temperature.[5]
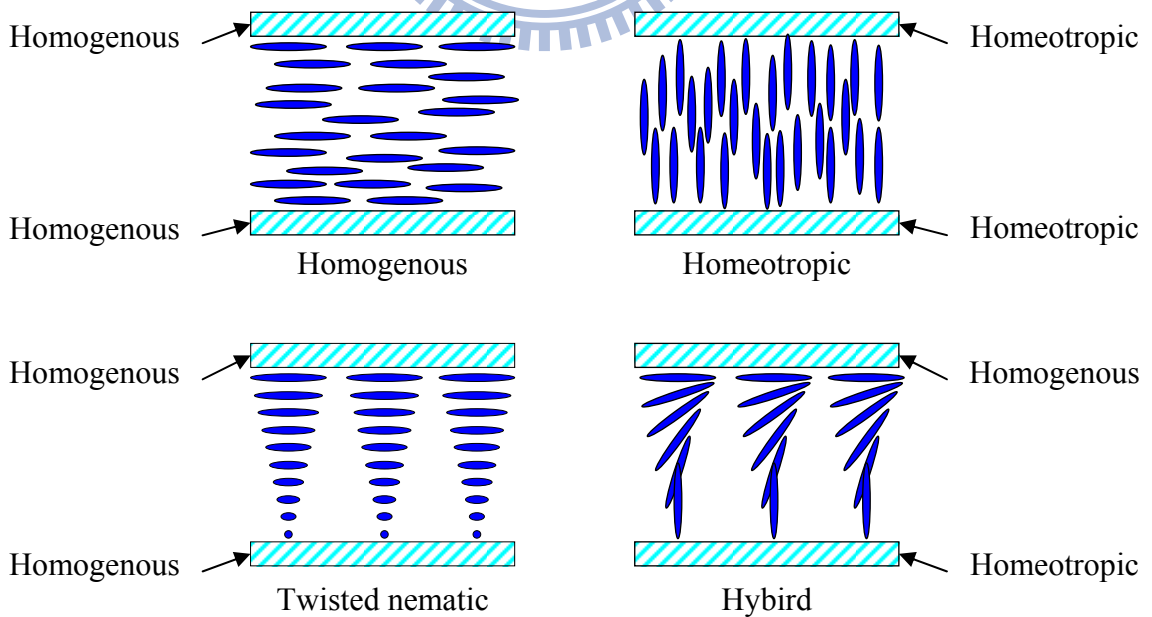
Figure 1-4 Typical orientations of liquid crystal molecules in different liquid crystal displays.

(a) N,N-dimethyl-N-octadecyl-3-aminopropyltrimethoxysilyl chloride (DMOAP)

$$Cl^- \ + N - (CH_2)_3 \ Si(OCH_3)_3$$

with $C_{18}H_{37}$ attached to N, and CH_3, CH_3 branches

$C_{18}H_{37}$
$(CH_2)_3$
SUBSTRATE

(b) N-methyl-3-aminopropyltrimethoxysilane (MAP)

$$H_3C - N - (CH_2)_3 \ Si(OCH_3)_3$$

with H attached to N

$(CH_2)_3$
SUBSTRATE
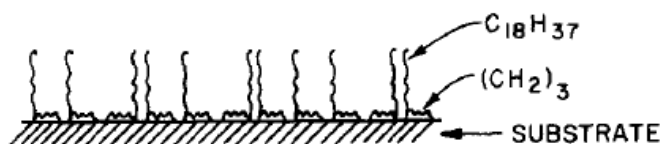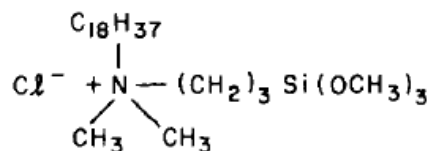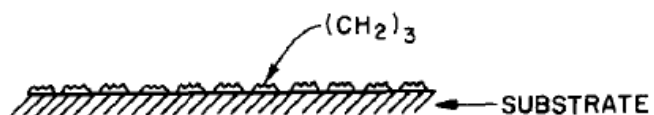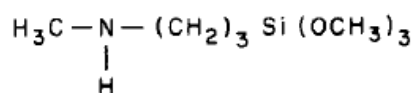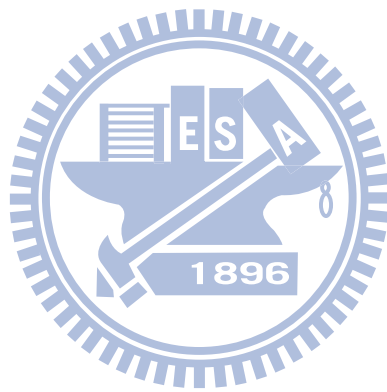
Figure 1-5 Chemical formulas of DMOAP and MAP and the surfaces which result from their application to a substrate.[32]

Chapter 2
Strong vertical alignment of liquid crystal on anodic aluminum oxide film with different pore size

2.1 Overview

Anodic Alumina Oxide (AAO) is an inorganic and porous material. It is almost transparent and colorless in visible region. Because of these properties, AAO film is a good candidate as the alignment layer of liquid crystal displays. **Appendix A.2** shows how to manufacture the porous AAO thin film. The mechanism of AAO formation is also discussed in **Appendix A.4**. Recently, T. Maeda and K. Hiroshima had demonstrated the vertical alignment of liquid crystal molecules on AAO films. [1][2] In their work, the depth and the diameter of the nanopores in the AAO film are 100-150nm and 5-20nm, respectively. The measured pretilt angle and the observed conoscopic pattern of the liquid crystal cells indicate that the liquid crystal molecules are aligned vertically on AAO films. They also showed that the pretilt angle can be changed by anodizing the pre-rubbing aluminum film. In this work, we use both one-step and two-step process to produce non-uniform and uniform porous AAO thin film, respectively. By using different anodizing voltages, we can control the pore sizes of the AAO films. We examined the relationship between the polar anchoring strength and the anodizing voltage. All these different AAO films are good vertical alignment layers. It is shown, however, that the anchoring strength depends on anodizing condition. This is due to the voltage-dependent pore sizes of the AAO films.

2.2 Experimental procedures

The porous AAO is formed by anodizing aluminum thin film or aluminum

foil in acid electrolytes. By using one-step process or two-step process, it is easy to form crack-like or hexagonal porous AAO structure. The pore sizes are controllable by varying the anodizing voltage. For the two-step process, the thickness of AAO thin film can be controlled by changing the anodizing time of the first step. The remaining curved aluminum thin film can form the uniform porous AAO thin film. The more detail manufacture description is shown in **Appendix A.2.**

By using the field emission scanning electron microscope (FESEM: HITACHI S-4700i), we can observe the morphology and the nanostructure of the porous AAO thin film. All AAO thin films are evaporated thin platinum or gold layer to reduce charging effects. The thickness of AAO thin film can be measured by examining the cross-view of the AAO FESEM image. By using the image processing program, ImageJ, we can analysis the FESEM image to determine the average pore size, the average AAO wall area, and the density of pores. The software introduction and the analysis algorithm of ImageJ are shown in Appendix C.

In order to use the AAO thin film as the alignment layer, the transmittance of AAO thin films in visible region are very important. The transmittance of AAO thin films are taken by using a UV-Visible spectrometer (Oceanoptics, model ISS-UV-VIS and USB2000) with air as the reference.

Finally, we need to investigate the alignment characterization of the AAO thin film. The investigative cell is made by putting together a pair of glass substrates with the AAO film face to face. The nematic liquid crystal, 5CB (Merck) was filled into the cell in the isotropic phase (above 36°C). The thickness of liquid crystal layers is 23 μm. The liquid crystal alignment in the cell is examined with a polarizing microscope. The cell is put between a pair of crossed polarizers. By using the polarizing microscope, we can examine the transmitted image and the conoscopic image. The conoscopy is a useful optical method to analyze the alignment of the uniaxial crystals by observing the interference

image.[3]

By applying the magnetic field on the vertical alignment cell, the polar anchoring strength can be determined from the transmittance, which is a function of applied magnetic field above the threshold magnetic field. The polar anchoring strength characterizes the surface energy ability out of the substrate plane. The theory and analysis method of the polar anchoring strength are discussed in Appendix B.

2.3 Results and discussions

2.3.1 Anodizing current characterization

By using the function of the power supply (Keithley Instruments Inc. Model 2410 General-Purpose SourceMeter), we can record the anodizing current during the anodizing process. For the anodizing current characterization analysis, the thickness of the aluminum thin film is 500 nm. The anodizing current characterization is shown in Figure 2-1 and Figure 2-2 for one-step and two-step process, respectively. For both one-step and two-step process, the anodizing process with lower anodizing voltage has lower anodizing current and longer anodizing time. According to the manual of 2410 SourceMeter, the maximum power is 22W. The range of operation is 21V at 1.05A or 1100V at 21mA.[4] Because the range of operation is 21V for 20V, the capability of anodizing current can be 1.05A. When the anodizing voltage is larger than 20V, the range of operation is 1100V, the capability of anodizing current can only be 21mA. In Figure 2-1 and Figure 2-2, it is obviously that the anodizing current is saturated at 21mA for V≥50V. In Figure 2-2, the dash and solid line are the anodizing current characterization of the first and second step process of two-step process, respectively.

For more investigations, we can integrate the anodizing current by the anodizing time. The integrated result is the total charge of the anodizing process.

Table 2-1 shows the total charge of the one-step anodizing process for different anodizing voltage. It clearly shows the total charge is around 6 Coulomb regardless the anodizing voltage. According to the mechanism, the total charge is proportional to the thickness and the anodized area of the aluminum thin film. Table 2-2 shows the charge of first step and second step in the two-step process for different anodizing voltage. The total charges are also around 6 Coulomb for different anodizing voltage, even the first step or the second step is different anodizing duration.

2.3.2 Morphology of the anodic aluminum oxide surface

Figure 2-3 shows the FESEM image of the AAO film formed by using the one-step process. There were only fine crack-like structures connecting irregular small pores on the surface of the AAO film. When the anodized voltage was varied from 20 to 70V, the widths of the pores remained almost the same, about 5-15nm. By using the two-step process, the surface of the AAO film had regular pores as shown in Figure 2-4. These pores were self-assembled into hexagons. According to cross-sectional observation by the FESEM, the actual thicknesses of AAO films prepared by the one-step process were 415±15 nm, while those by the two-step process were 210±30nm. In Figure 2-5, we show the relationship between the diameter of pores and the anodizing voltage. The pore size is determined by measuring some pores in the SEM image directly. The data dots in Figure 2-5 are the average size of these pores and the error bars are the standard deviation of these pores.

The diameters of pores for the two-step process increased linearly from 15 to 50nm as the anodizing voltage was increased from 20V to 50V. For V > 50V, the diameter of pore was saturated at a value around 65nm. The saturated values for pore diameters were observed for both cases, nonetheless. According to the anodizing current characterizations, we note that the anodizing current was saturated at 21mA, the current limit of the power supply, when V > 50V. If the

anodizing current is saturated at the current limitation, the power supply will operate in constant current mode, and the anodizing voltage will be limited by the maximum current, 21mA for Model 2410, when V > 50V. In contrast, the diameters of pores for AAO prepared by the one-step process were small and did not exhibit apparent trend when the anodizing voltage was varied in this range.

2.3.3 Transmittance of the anodic aluminum oxide layer

Figure 2-6 shows the transmittance of the AAO films on the ITO glass substrate as a function of wavelength from 300 to 800 nm. The cut off wavelength at 350nm is due to absorption of the ITO glass substrate. For the AAO films anodized at a bias voltage from 20V to 40V, the transmittance is about 65% over this spectral range. In comparison, the transmittance of the substrates with the ITO thin film on the back side is around 80%. For AAO films anodized at a bias voltage from 50V to 70V, the transmittance reduces to about 55%. Ripples in the spectral transmittance for the AAO films, for which the thickness varies from 300 to 500 nm, are attributed to the interference effects of the films. The spectral transmittance of the substrate is relatively smooth, because the ITO-film is very thin, 50-100 nm in thickness. Our data showed that the AAO film is highly transparent in the visible region and is a very good candidate of alignment layer in LCD applications.

2.3.4 Alignment characterization

In this section, the alignment characterizations are investigated by using the liquid crystal cell. By putting together a pair of glass substrates with the AAO alignment layer face to face, the cell with cell gap of 23μm was made. The nematic liquid crystal, 5CB (Merck) was filled into the cell in the isotropic phase (above 36°C). The liquid crystal alignment in the cell was examined with a polarizing microscope in microscopic mode and conoscopic mode.

In Figure 2-7, we show the polarizing microscopic images of the liquid crystal cells with the AAO alignment thin film manufactured by using one-step process. The liquid crystal cells are observed in a pair of crossed polarizers. The micrographs are taken in two orientations of the cell, 45° with respect to each other. Regardless of the anodizing voltages, all of the liquid crystal cells show the dark state in both 0° and 45°. The dark state observed for both cases indicates that vertical alignment of liquid crystal was achieved. Figure 2-8 shows the polarizing microscopic images of the liquid crystal cells with the AAO alignment thin film manufactured by using two-step process. No matter what the anodizing voltage is, all of these images in Figure 2-8 are the dark state. That is mean all of the AAO thin film with two-step process are good vertical alignment.

Figure 2-9 shows the conoscopic image of the same liquid crystal cells with both one-step and two-step AAO alignment layers. It obviously shows that all conoscopic images are the cross texture. The cross texture also shows that the liquid crystal cell was vertically aligned.[3] Further, in order to confirm the vertical alignment, the pretilt angles of the liquid crystal cells were measured by using the crystal rotation method [5]. Figure 2-10 shows the pretilt angle of the liquid crystal cell with the AAO alignment layer. For all of these cells with anodizing voltage between 20 and 70V, the pretilt angles were between 89.5° and 90.0°. There is no significant difference between the samples prepared with one-step or two-step processes.

2.3.5 Polar anchoring strength analysis

According to the previous section, we already knew that the AAO thin film can vertically align nematic liquid crystal. In order to know the alignment ability of the AAO thin film and compare to the other traditional vertical alignment layer, N, N-dimethyl-N-octadecyl-3-amino-propyl-trimeth oxysilyl chloride (DMOAP) , we made a few liquid crystal cells with the same AAO alignment layer, and

measured the polar anchoring strength of these samples by using the magnetic field method [6]. The polar anchoring strengths of the liquid crystal cells are plotted versus the anodizing voltages from 20V to 60V as shown in Figure 2-10. The data dots in Figure 2-11 are the average anchoring strength, and the error is the standard deviation. For AAO films anodized at different voltages, the uniformities of the films are different. The error bars in anchoring strengths of AAO films with non-uniform pore sizes are larger than those of uniform ones.

As a reference, we have determined the polar anchoring strength of N,N-dimethyl-N-octadecyl-3-amino-propyl-trimeth oxysilyl chloride (DMOAP) to be $38\pm6\times10$-6 J/m2. Notably, AAO films prepared by these two methods show similar polar anchoring strengths, comparable but still somewhat smaller than that of the traditional vertical alignment film (DMOAP). Figure 2-11 also indicates clearly that the uniformity of the pore array is not a key parameter in effective alignment. In this sense, the one-step process for preparing AAO films is advantageous over the two-step process.

By the way, it is possible to reduce the anodizing voltage to 5 or 10 Volts. We expect such AAO films will have higher anchoring strength. Unfortunately, this will increase the anodizing time appreciably. According to our experimental data, the anodizing time for 20V is around 30 minutes. If we use lower anodizing voltage (5 or 10 V), it maybe take more than 1 hour.

According to Figure 2-5 and Figure 2-11, it is easy to show the relationship between the polar anchoring strength and pore diameter in Figure 2-12. Regardless of whether the AAO films were prepared by the one-step or two-step processes (the solid circles and squares, respectively), the polar anchoring strengths of AAO film with smaller pore diameters are stronger. The maximum polar anchoring strength for 5CB on the uniformly porous AAO film is 15×10^{-6} J/m^2. Because 5CB is a rod-like nematic liquid crystal, the long axis of 5CB will tend to align parallel to the long axis of AAO cylindrical pore. In AAO films with small–pores, most of liquid crystal molecules would be confined by the pore wall.

In large–pore AOO films, the liquid crystal molecules near the pore wall would still be well-confined, but the liquid crystal molecules in the central part of the pores would just tend to align parallel to the adjacent liquid crystal and not strongly affected by the walls. As a result, large-core AOO films exhibit less anchoring strength. On the other hand, AAO films with smaller pore diameters would have more surface area for effective alignment.

2.3.6 Possible alignment mechanism

According to the relationship between the polar anchoring strength and the pore sizes, the possible mechanism of liquid crystal alignment on porous AAO thin film is discussed as follows. The alignment of liquid crystal molecules depend on the surface morphology and the surface tension energy. Depending on the surface tension energy of the AAO material, the liquid crystal molecules tend to align parallel to the AAO surface. Figure 2-13 shows the scheme of the possible alignment mechanism. Considering the same thickness of the AAO thin films, those with smaller pore sizes have higher anisotropy out of plane. Therefore, more liquid crystal molecules are aligned by the AAO surface perpendicular to the substrate surface, the AAO thin films have stronger alignment abilities and higher polar anchoring strength. On the other hand, the AAO thin films with larger pore sizes have lower polar anchoring strength.

2.4 Summaries

We investigated the alignment properties of AAO films prepared by two types of anodizing processes. In contrast to those anodized by the one-step process, the AAO films prepared by the two-step process exhibit regular hexagonal pore arrays. The diameter of pores of AAO films can be controlled easily by adjusting the anodizing voltage. For the two-step process, the diameter of pore is controlled from 17nm to 65nm. Using the nanoporous AAO film as the

alignment layer, excellent vertical alignment for the LC cell can be achieved. The pretilt angle of the LC cell by using AAO film as an alignment layer is very close to 90°. The polar anchoring strength for this LC cell is about 15×10-6 J/m2 which is just a little weaker than DMOAP, commonly used vertical alignment layer. The AAO films, on the other hand, can be used without rubbing and easily scalable for industrial applications. Our studies further indicates that AAO films prepared by the one-step process, even though do not exhibit uniform array of pore, are as effective in alignment as those prepared by the two-step process. We also demonstrated that AAO films with smaller pore diameters exhibit higher anchoring strengths.

References

[1] T. Maeda and K. Hiroshima, "Vertically aligned nematic liquid crystal on anodic porous alumina," *Jpn. J. Appl. Phys.* **43**, L1004 (2004).

[2] T. Maeda and K. Hiroshima, "Tilted liquid crystal alignment on asymmertrically grooved porous alumina film," *Jpn. J. Appl. Phys.* **44**, L845 (2005).

[3] B. L. Van Horn, and H. H. Winter, "Analysis of the conoscopic measurement for uniaxial liquid-crystal tilt angles," *Applied Optics* **40**, 2089 (2001).

[4] Keithley Model 2400 Series SourceMeter$^{®}$ User's Manual, Chapter 3 Basic Souce-Measure Operation, 3-3.

[5] T. J. Scheffer, and J. Nehring," Accurate determination of liquid-crystal tilt bias angles," *J. Appl. Phys.* **48**, 1783 (1977).

[6] K. H. Yang, and C. Rosenblatt, "Determination of the anisotropic potential at the nematic liquid crystal-to-wall interface," *Appl. Phys. Lett.* **43**, 62 (1983).

Tables

Anodizing voltage	Total charge
20 V	5.75 C
30 V	6.22 C
40 V	5.96 C
50 V	5.82 C
60 V	5.94 C
70 V	5.85 C

Table 2-1 The total charge of the one-step anodizing process for different anodizing voltage.
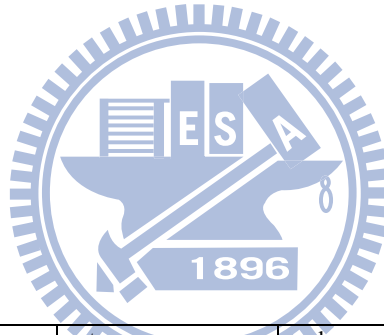
Anodizing voltage	1st step charge	2nd step charge	Total charge
20 V	3.84 C	2.55 C	6.39 C
30 V	4.00 C	1.92 C	5.92 C
40 V	3.92 C	1.85 C	5.77 C
50 V	3.76 C	2.26 C	6.02 C
60 V	3.08 C	2.93 C	6.01 C
70 V	3.14 C	2.89 C	6.03 C

Table 2-2 The total charge of the two-step anodizing process for different anodizing voltage.

Figures
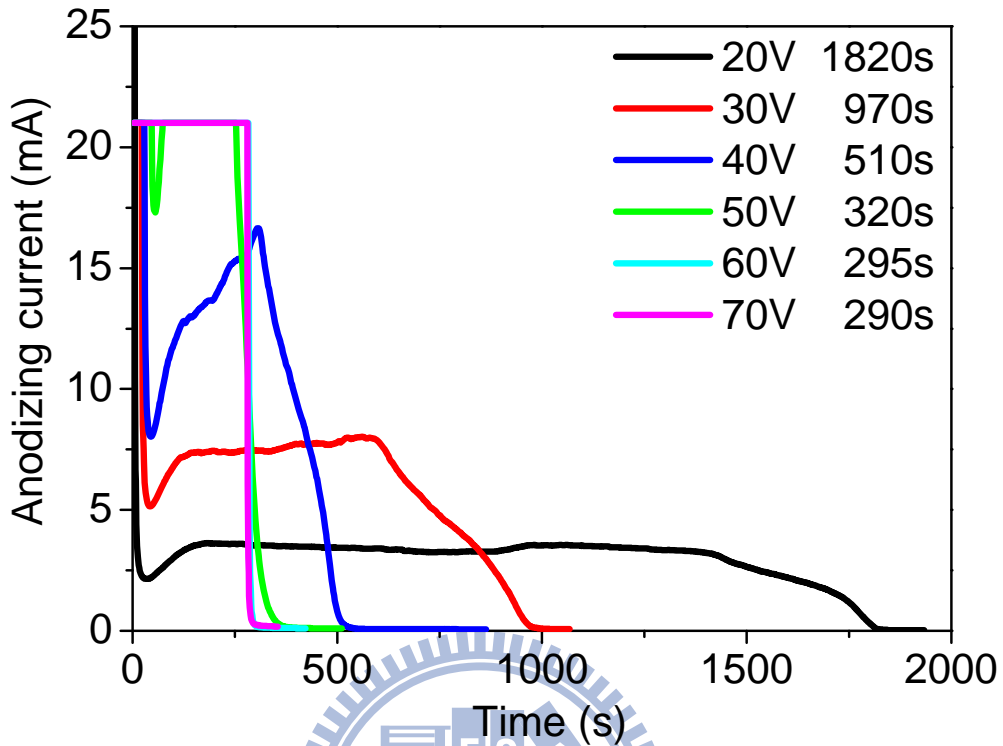
Figure 2-1 The anodizing current characterization of the one-step process in different anodizing voltages.
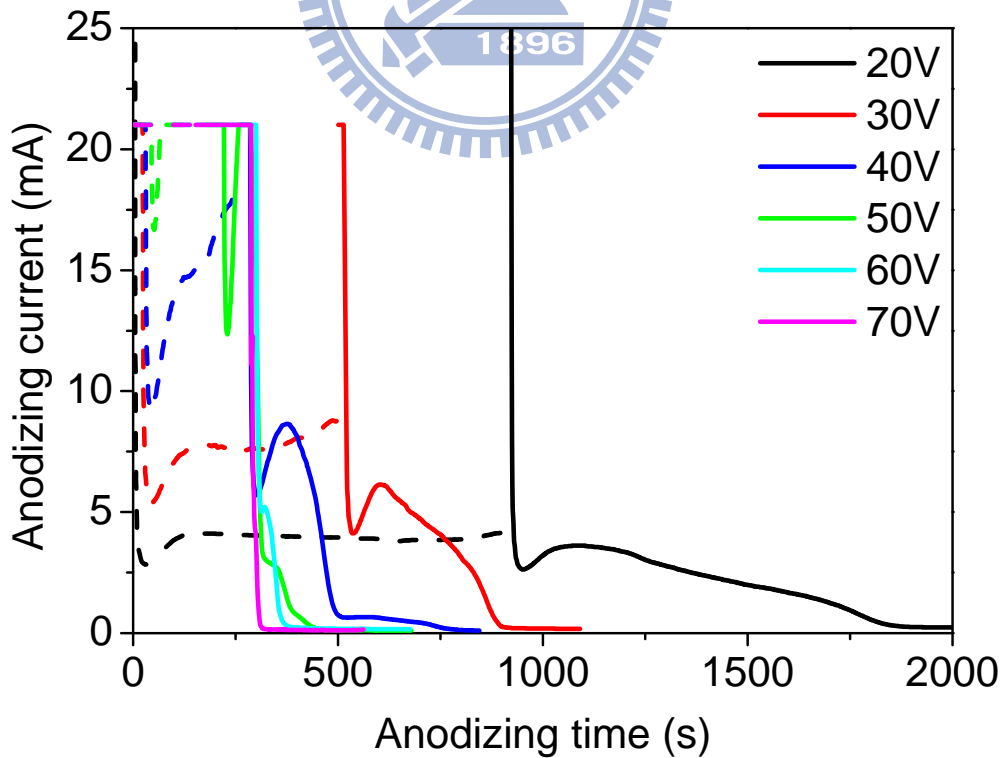
Figure 2-2 The anodizing current characterization of the two-step process in different anodizing voltages. The dash and solid line are anodizing current characterization of the first and second step process, respectively.
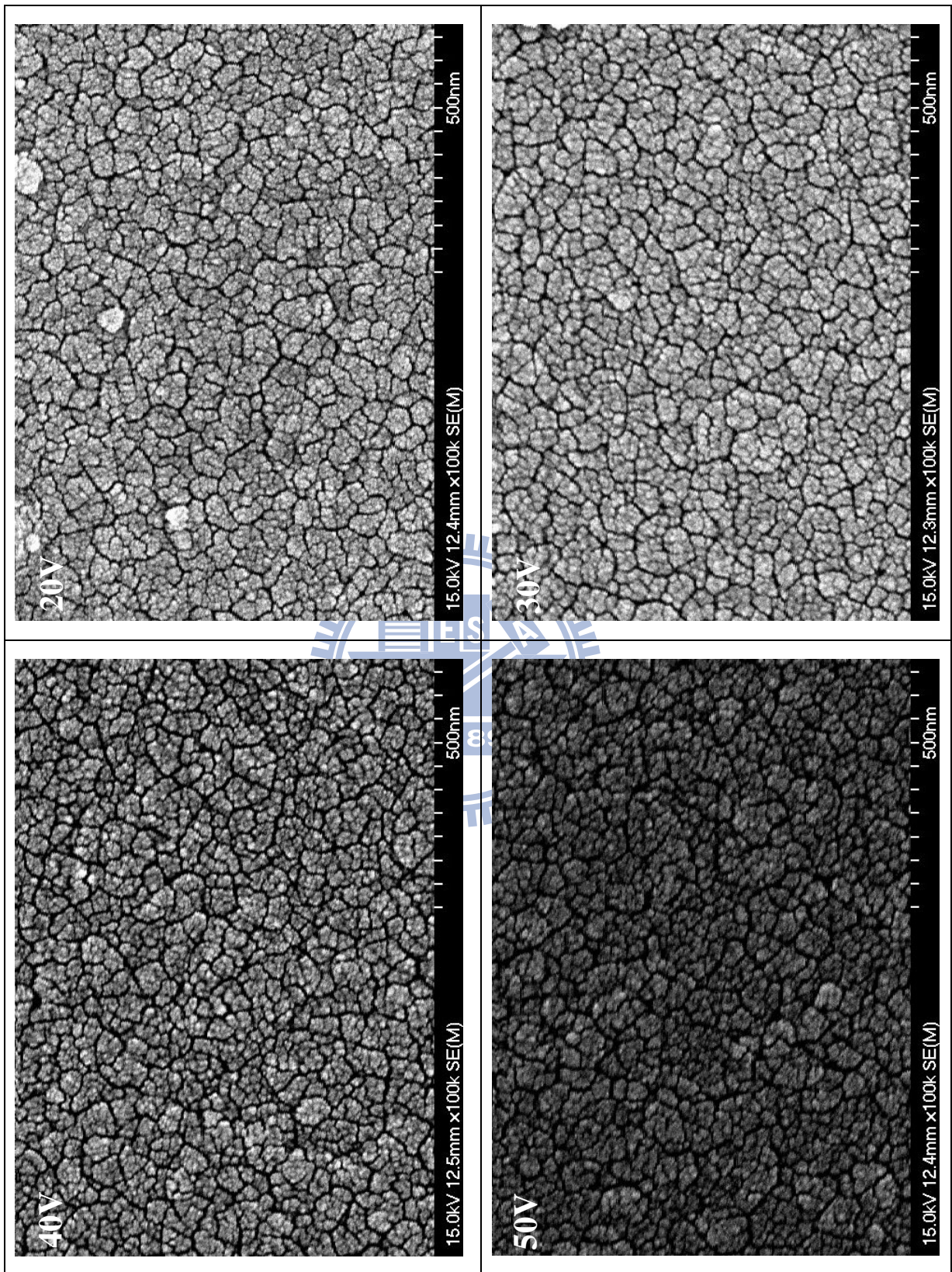
Figure 2-3 FESEM images of AAO thin film by one-step process. The anodizing voltage is 20-70V.
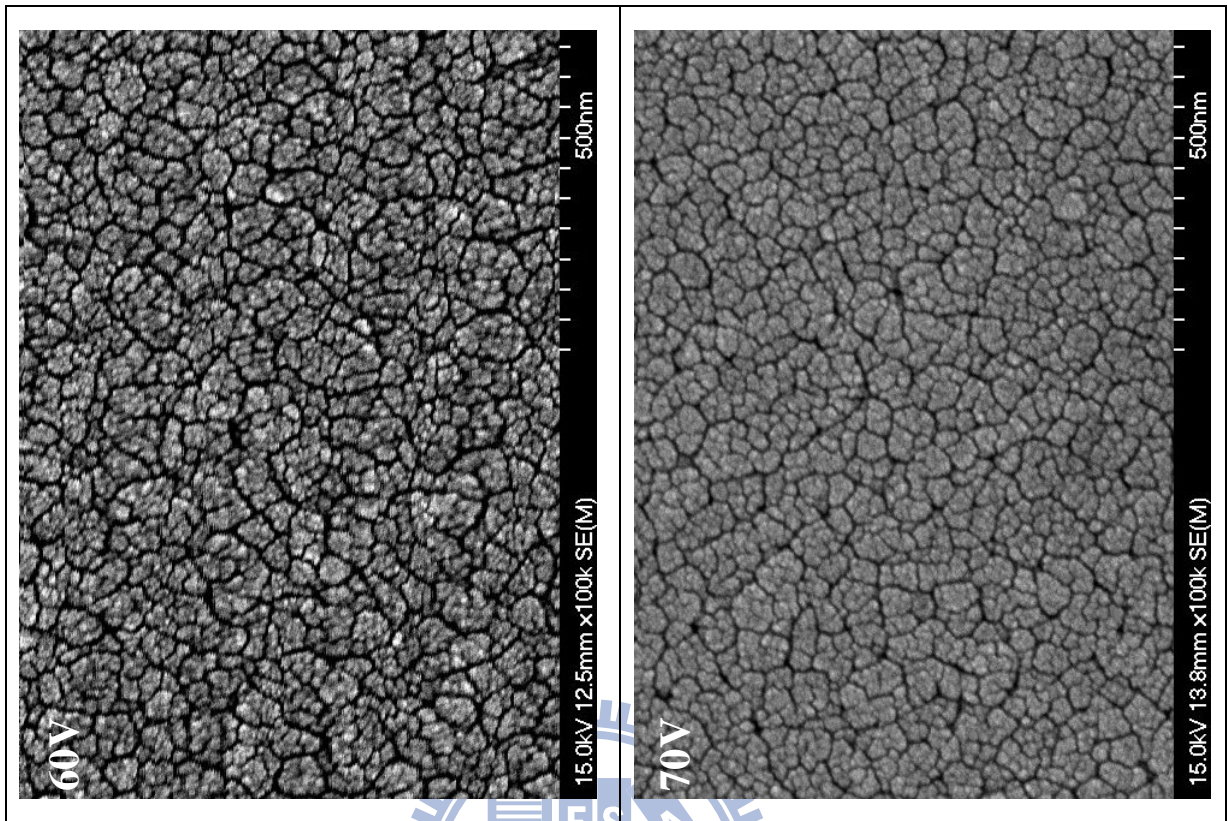
Figure 2-3 (cont'd) FESEM images of AAO thin film by one-step process. The anodizing voltage is 20-70V.
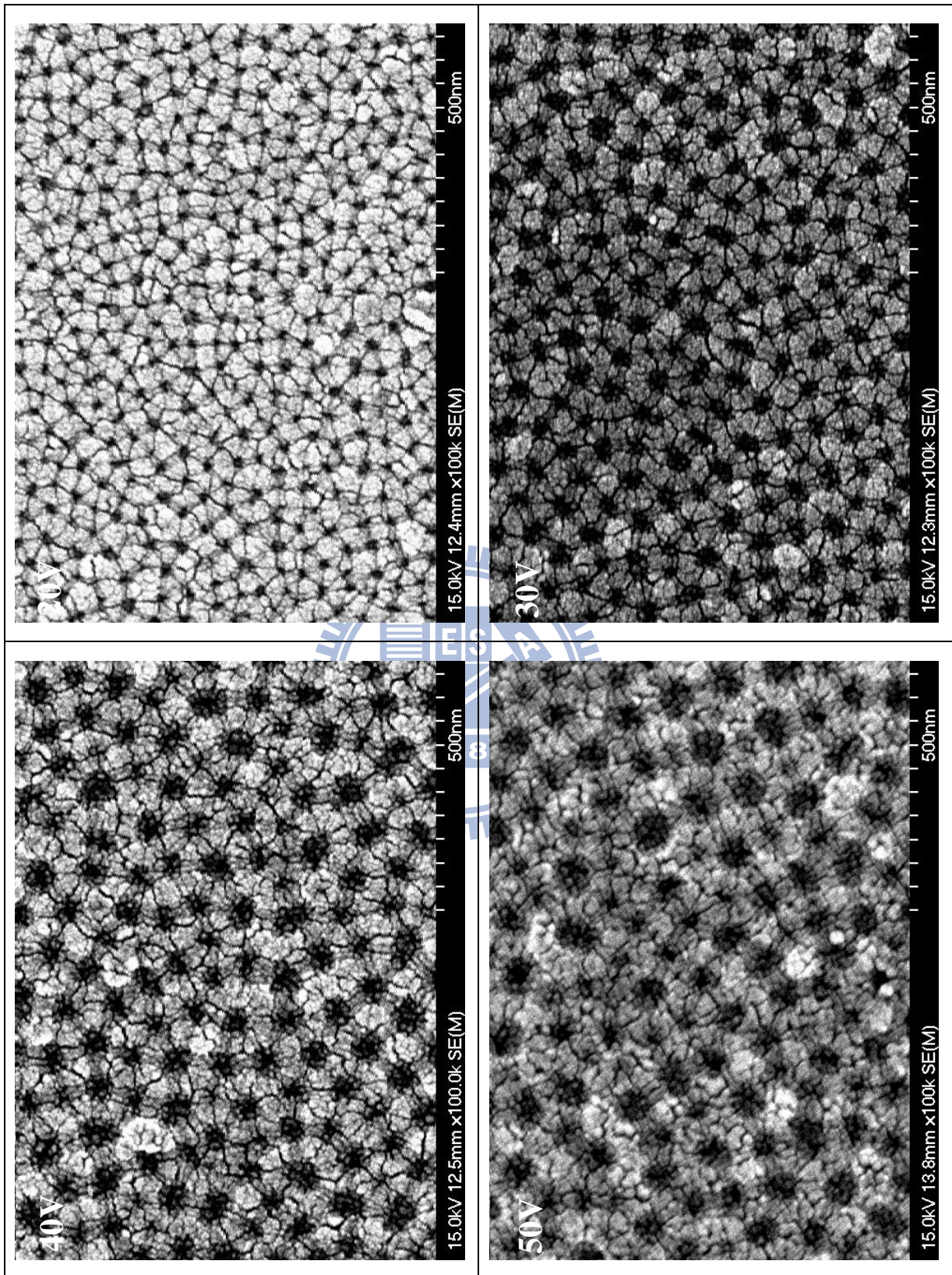
Figure 2-4 FESEM images of AAO thin film by two-step process. The anodizing voltage is 20-70V.
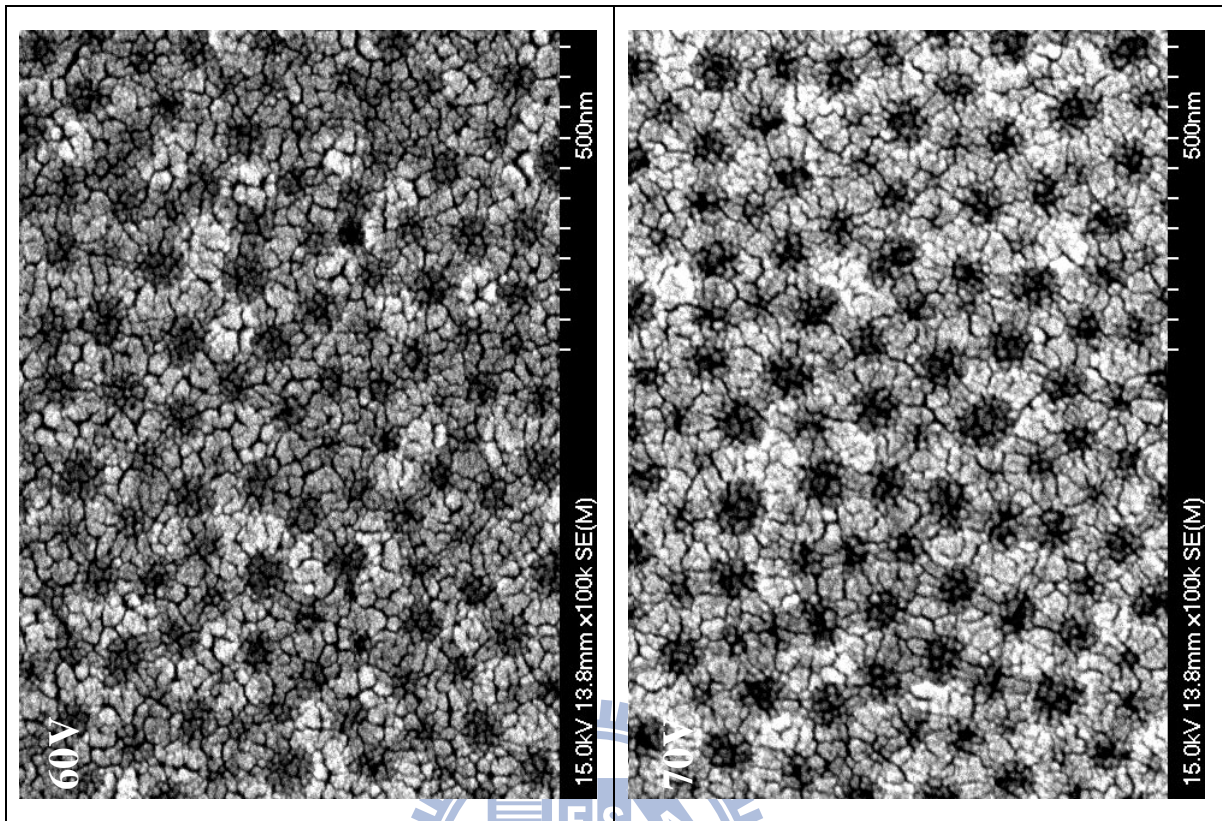
Figure 2-4 (cont'd) FESEM images of AAO thin film by two-step process. The anodizing voltage is 20-70V.
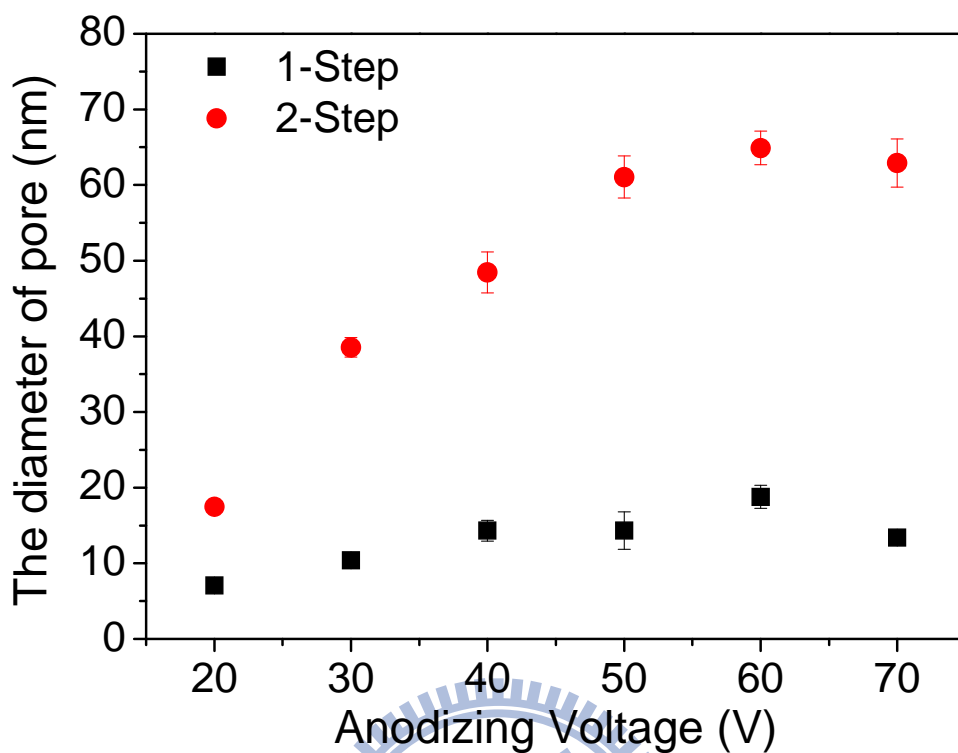
Figure 2-5 The relationship between the pore diameter and the anodizing voltage.
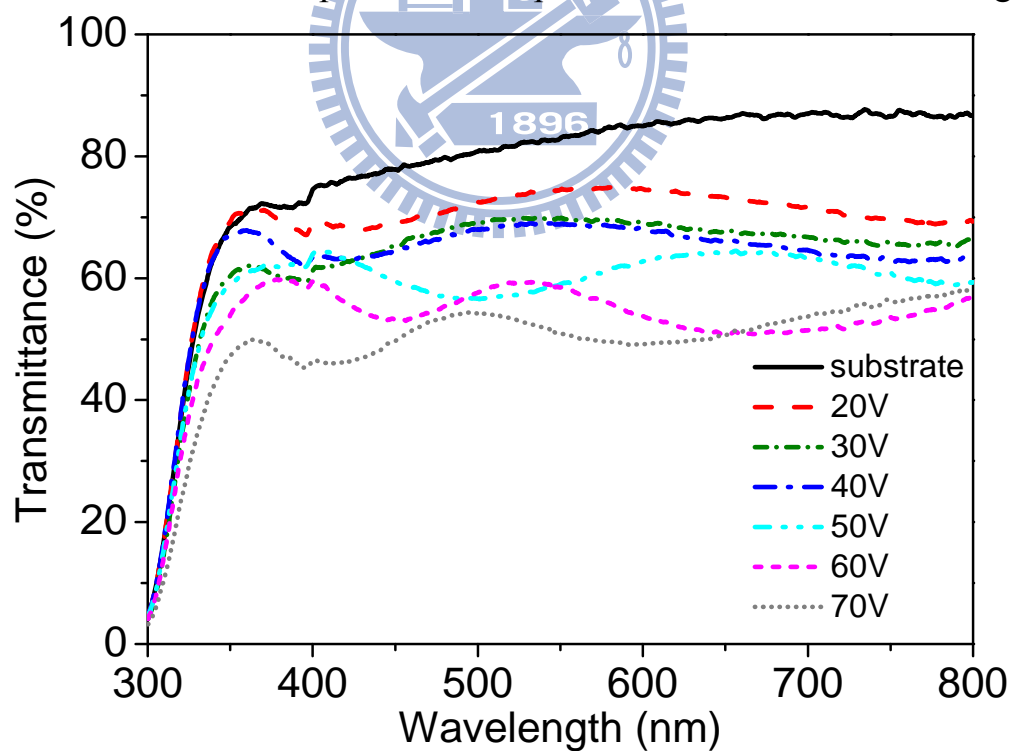
Figure 2-6 Transmittance of and the substrates with AAO films with anodized at different voltages.
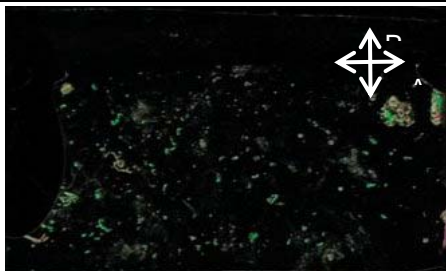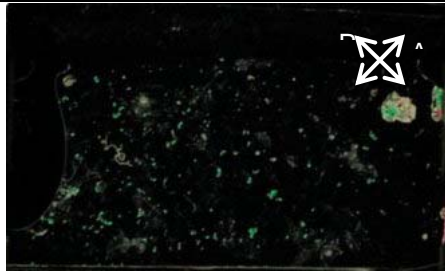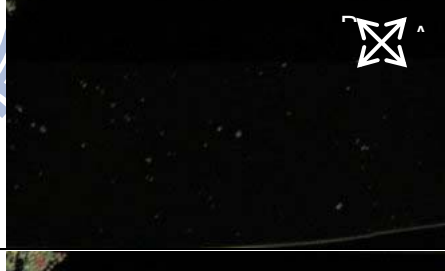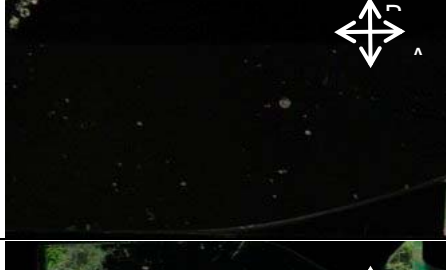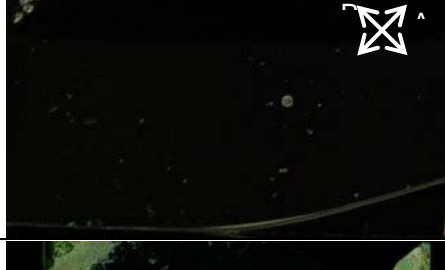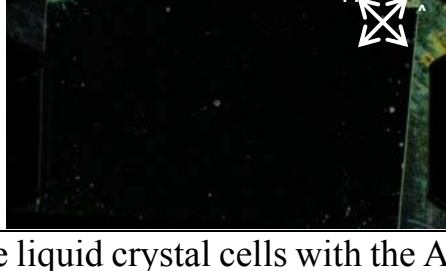
Anodizing voltage	0°	45°
1 step 20 V		
1 step 30 V		
1 step 40 V		
1 step 50 V		
1 step 60 V		
1 step 70 V		

Figure 2-7 Polarizing microscopic images of the liquid crystal cells with the AAO thin film manufactured by using one-step process.

Anodizing voltage	0°	45°
2 step 20 V		
2 step 30 V		
2 step 40 V		
2 step 50 V		
2 step 60 V		
2 step 70 V		

Figure 2-8 Polarizing microscopic images of the liquid crystal cells with the AAO thin film manufactured by using two-step process.

Anodizing voltage	One-step	Two-step
20 V		
30 V		
40 V		
50 V		
60 V		
70 V		

Figure 2-9 Conoscopic images of the liquid crystal cell with the AAO thin film manufactured by using one-step and two-step process.
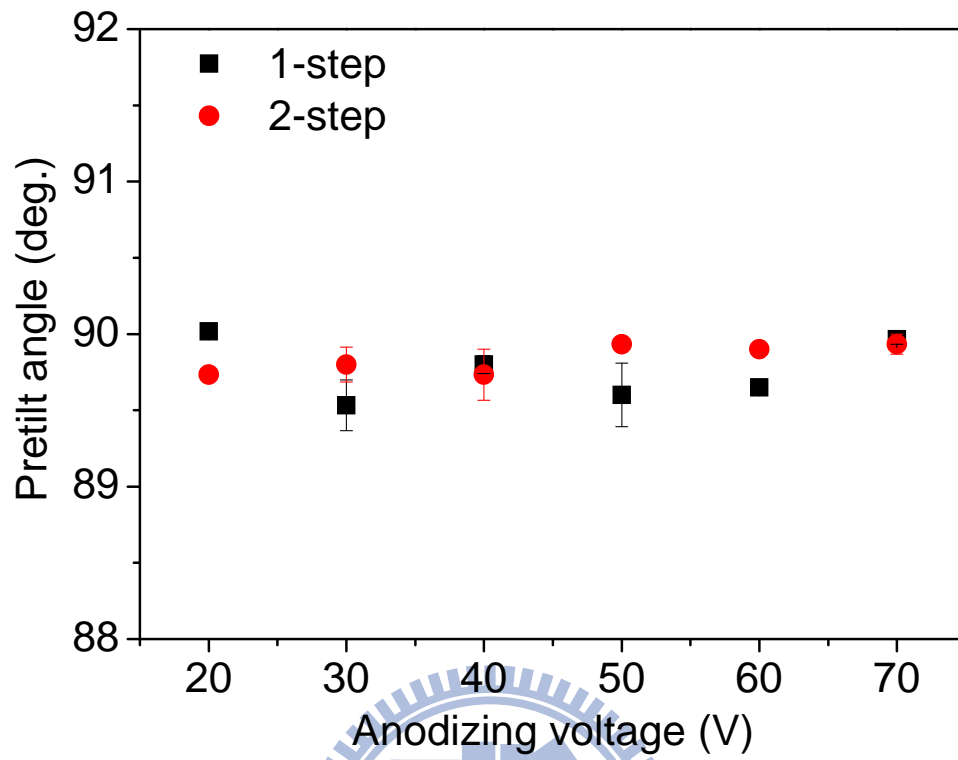
Figure 2-10 Pretilt angles of the liquid crystal cell with the AAO thin film manufactured by using one-step and two-step process with different anodizing voltage.
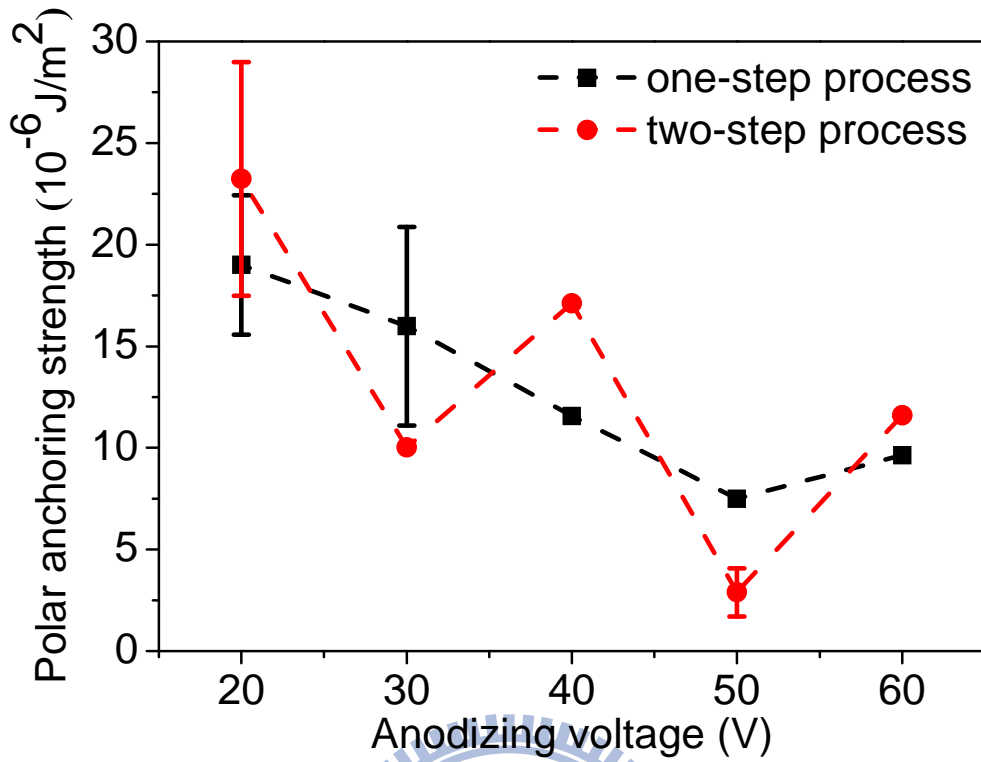
Figure 2-11 The relationship between the polar anchoring strength and the anodizing voltage.
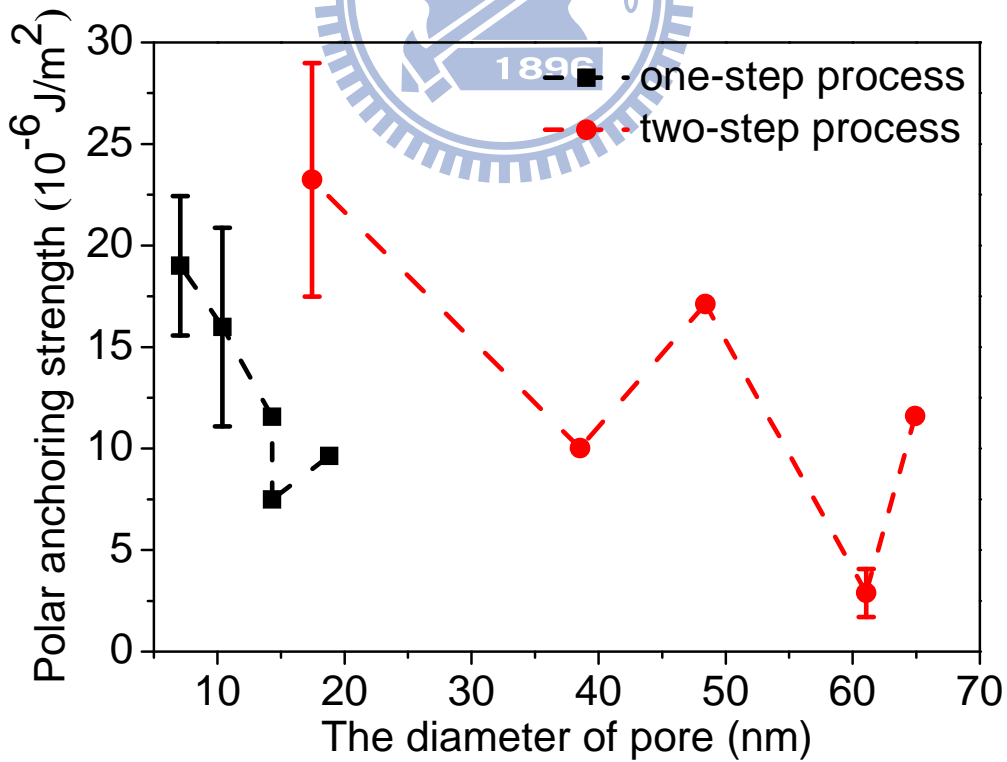
Figure 2-12 The relationship between the polar anchoring strength and the diameter of pore.

Liquid crystal
molecules

Porous AAO
thin film

Smaller pore sizes

larger pore sizes
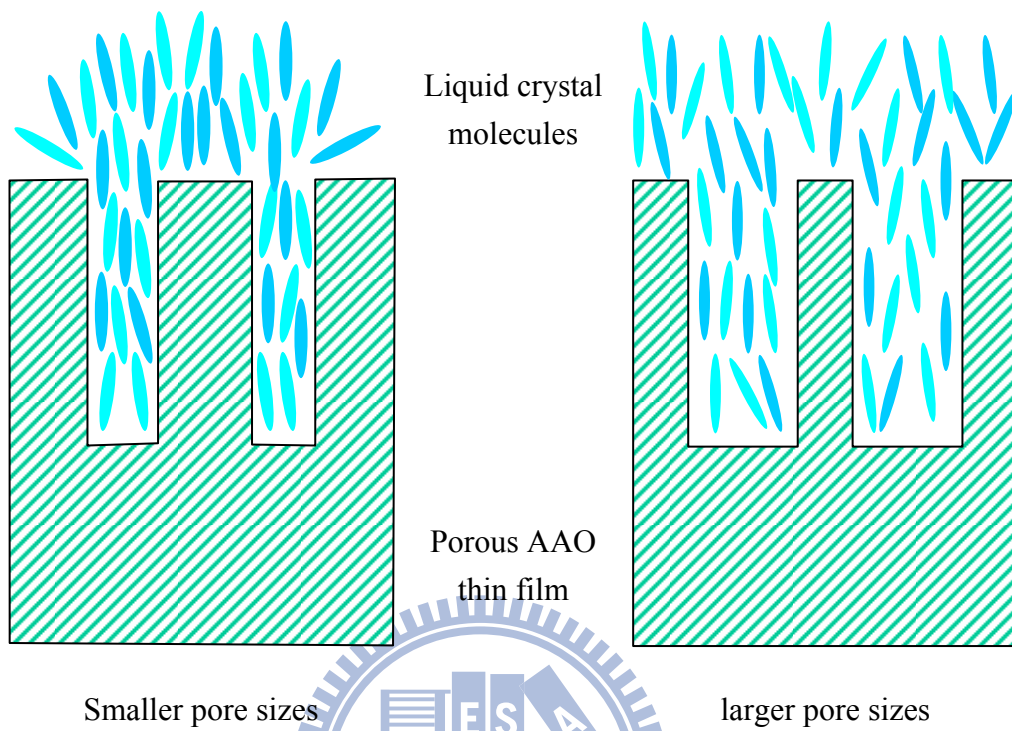
Figure 2-13 Scheme of the possible alignment mechanism.
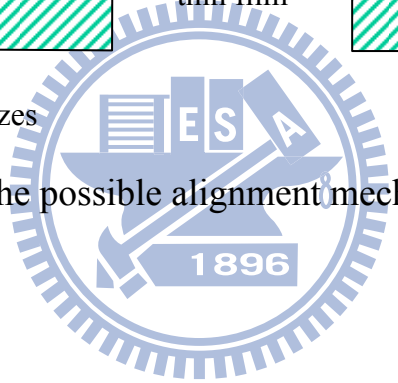
Chapter 3
The alignment properties of liquid crystal on anodic aluminum oxide film with different aspect ratio

3.1 Overview

In Chapter 2, we have demonstrated the strong vertical alignment of liquid crystal on Anodic Alumina Oxide (AAO) thin film with different pores size. By using the porous AAO film as the alignment layer, excellent vertical alignment for the LC cell can be achieved. In order to investigate the alignment mechanism, there are more variables discussed in the following chapter.

3.2 Experimental procedures

In this chapter, we only use the one-step porous AAO thin film. The detail manufacture description is also shown in Appendix A.2. Figure 3-1 shows the scheme of the experimental procedure for the etched AAO thin film with different etching time. Here we only consider 40V one-step process case, and fix the anodizing voltage. After the one-step process finished, the substrate with the one-step AAO thin film was immersed in a mixture of chromic acid (1.5 wt% H_2CrO_4) and phosphoric acid (6 wt% H_3PO_4) at 60°C. It is the same etching solution used in the two-step process. Here, we control the etching time, between 1.5 minutes and 6.0 minutes. The etching process not only removes the formed AAO from top to bottom, but also etches the wall of the AAO cylinder. By this process, we can reduce the thickness of the AAO thin film and expand the diameter of the pores of AAO thin film.

To investigate the alignment properties of liquid crystal, the morphology and the nanostructure of the porous AAO thin film, the transmittance of AAO thin

films in visible region, the alignment characterization of the AAO thin film, and the polar anchoring strength are measured for the AAO thin film with different aspect ratio. All of these measurements are taken by the same equipments and the same method as those described in Section 2.2.

3.3 Results and discussions

3.3.1 Morphology of the anodic aluminum oxide surface

Figure 3-2 shows the FESEM image of the etched AAO thin film with different etching time. The top view images are shown in left column, and the side view images are shown in right column. When the etching time is 0 minute, the process is just a one-step process, and the FESEM image also shows the fine crack-like structures connecting irregular small pores. After immersing the one-step AAO thin film in the etching solution, the nanoporous structure is appeared in FESEM image. Figure 3-3 shows the relationship between the diameters of the pores and the etching time. The pore sizes of the first and second manufacture AAO thin films are consistent. If the etching time is less than 3.0 minute, the pore sizes are almost proportional to etching time. When the AAO thin films immerse in the acid solution longer, the pore sizes become larger. That is because the AAO wall between two nanopores can be etched by the acid mixture. If the etching time is longer than 3.0 minute, the diameters of pores slightly decrease from 92nm to 81nm. At 3.0 minute, the FESEM image shows a different image. There are some clusters of nanorods with some hexagonal curve on the bottom of these clusters. The walls of AAO are etched too much and collapse because of the thinner walls. According to the side view image, it is easy to measure the thickness of the etched AAO thin film. Figure 3-4 shows the thickness of the etched AAO thin film with different etching time. Between 1.5 and 3.0 minute, the thickness remains around 450 nm. The thickness has a sudden drop at 3.5 minute. When the etching time is longer than 3.5 minute, the thickness

becomes less than 50 nm. According to the FESEM image for longer than 3.5 minute, most of the porous AAO arrays collapse and just remain the hexagonal curve surface. These rough surfaces contain thousand of nanotips, instead of the hexagonal pores array.

3.3.2 Transmittance of the anodic aluminum oxide layer

Figure 3-5 shows the transmittance of the AAO films on the ITO glass substrate as a function of wavelength from 300 to 1000 nm. The cut off wavelength at 350nm is due to absorption of the ITO glass substrate. For all etched AAO films with different etching time, the transmittance is about 65% over this spectral range. In comparison, the transmittance of the substrates with ITO thin film on the back side is around 80%. The ripples in the spectral transmittance for the AAO films with the etching time between 0.0 and 3.0 minute, for which the thickness are around 450 nm, are attributed to the interference effects of the films. Here the transmittance of the etched AAO thin film shows the same behavior. It is highly transparent in the visible region.

3.3.3 Alignment characterization

The alignment characterizations can be investigated by using the liquid crystal cell. The manufacture process and the structure of the test liquid crystal cell are the same as those in section 2.3.4. The test liquid crystal cell is a sandwiched cell with the etched AAO thin film as the alignment layer. The cell is filled into the nematic liquid crystal, 5CB (from Merck co.), in the isotropic phase (above 36°C). The liquid crystal alignment in the cell was examined with a polarizing microscope in microscopic mode and conoscopic mode in the nematic phase (room temperature, around 25°C).

In Figure 3-6, we show the polarizing microscopic images of the liquid crystal cells with the etched AAO alignment thin film. The liquid crystal cells are

observed in a pair of crossed polarizers. The micrographs are taken in two orientations of the cell, 45° with respect to each other. According to the discussion of the alignment characteristic in section 2.3.4, the AAO thin film can provide the vertical alignment for the nematic liquid crystal. The liquid crystal cells show the dark state in both 0° and 45°. The dark state observed for both cases indicates that vertical alignment of liquid crystal was achieved. Figure 3-6 shows only three cells, 2.0 min., 2.5 min. and 3.0 min., have the dark state in both 0° and 45°. It means only the AAO thin films manufacturing by these three conditions can perform as the vertical alignment layers. If the etching time is 0 min., 3.5 min., 4.0 min., 5.0 min., and 6.0 min., the polarizing microscopic images show the random textures that mean the alignment of liquid crystal molecules is random.

When the etching time is 1.5 min., the polarizing images show a dark state in 0° and a white state in 45°. It shows the homogenous alignment characteristic. It is different from the other cells. According to the FESEM image of this condition, it still has the hexagonal pore array. This performance is unusual. In order to investigate this unusual behavior, the conoscopic image is taken. Figure 3-7 shows the conoscopic image of the same liquid crystal cells with the etched AAO alignment layers. It shows that the conoscopic images of the 2.5 min., 3.0 min., and 3.5 min., are the cross texture. The cross or parabolic textures show that the liquid crystal cell was vertically or homogenously aligned, respectively. The other images do not show any regular pattern. For 1.5 min., it is neither the cross texture nor the parabolic texture. Therefore, the alignment mechanism for 1.5 min. is not clear, yet.

3.3.4 Polar anchoring strength analysis

According to the previous section, we already knew that the etched AAO thin film with the etching time from 2.0 min. to 3.0 min. can vertically align nematic liquid crystal. By measuring the polar anchoring strength, the alignment ability of the etched AAO thin film can be characterized. The polar anchoring

strength is measured by using the magnetic field method.[2] Figure 3-8 show the polar anchoring strengths of the liquid crystal cell cells are plotted versus the etching time from 2.0 min. to 3.0 min.. The data dots in Figure 3-8 are the average anchoring strength, and the error is the standard deviation. The different data dots with the same etching time are the polar anchoring strength in different liquid crystal cell with the AAO alignment layer with the same etching time. It clearly shows the etched AAO thin films with shorter etching time have stronger polar anchoring strength. Table 3-1 summarizes the diameter of pores, the thickness of the etched AAO thin film, and the aspect ratio with different etching time. The aspect ratio is the thickness of the etched AAO thin film divided by the diameter of pores. According to the relationship between the etching time and the aspect ratio, shown in Table 3-1, it is easy to show the relationship between the polar anchoring strength and the aspect ratio in Figure 3-9. This relationship is almost linear. The etched AAO thin film with higher aspect ratio has higher polar anchoring strength.

3.3.5 Possible alignment mechanism

In Section 2.3.6, the possible alignment mechanism of AAO thin film has been discussed. For further investigation in this chapter, both homogenous and homeotropic alignment are observed in the liquid crystal cell with AAO alignment layers. The alignment ability does not only depend on the pore sizes but also on the aspect ratio. The AAO thin films with higher aspect ratio have stronger polar anchoring strength. Here, the modified possible mechanism of liquid crystal alignment is discussed as follows. Figure 3-10 shows the scheme of the modified possible alignment mechanism. The AAO thin films with smaller pore sizes and higher aspect ratio have stronger polar anchoring strength. The aspect ratio R is defined as thickness/diameter, $l/2r$. Considering a perfect cylinder, the total area of the wall is $2\pi rl$, where r and l are the

radius and depth of the cylinder, respectively. The total area can be rewritten as $4\pi r^2 R$. Assuming the pore sizes are constant, the porous AAO thin films with higher aspect ratio have larger surface area at out-of-plane direction. The liquid crystal molecules are affected by the AAO surface at not only in-plane but also out-of-plane direction. Therefore, the alignments of liquid crystal molecules depend on the ratio of the in-plane area to out-of-plane area of the porous AAO surface. The surface property of the AAO material is dominated the alignment property, homogenous alignment. The porous structures modify the alignment ability. For porous AAO thin films which contain high aspect ratio pores array, the area at out-of-plane direction is much larger than that at in-plane direction. The liquid crystal molecules are aligned homeotropically by the out-of plane surfaces. Resulting in the AAO thin films are as the vertical alignment layer. It is the most possible alignment mechanism of liquid crystal on the porous AAO thin film.

3.4 Summaries

We investigated the alignment properties of the etched AAO films prepared by etching the one-step AAO thin film with different etching time. Because the etching process is perpendicular to the AAO surface, both the thickness and the pores diameter of the etched AAO thin film can be modified, and the aspect ratio is controllable. Both homeotropic and homogenous alignment properties are observed on the etched AAO thin films. When the etched walls of the AAO pores are too thin, the wall will collapse, and the hexagonal pores array will be removed. The hexagonal curve surface can not perform as the alignment layer. According to our experiments, the AAO thin film with higher aspect ratio has higher polar anchoring strength. The further research about the mechanism of the alignment on the etched AAO thin film is under processed. We need more evidences to understand the alignment properties and the alignment mechanism
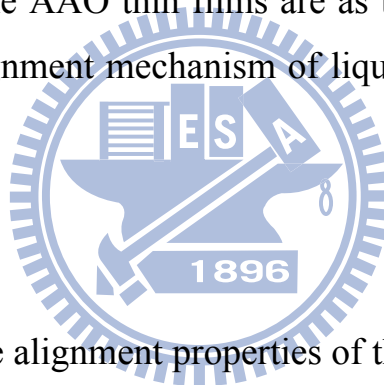
of the AAO thin film.

References

[1] T. Maeda and K. Hiroshima, "Vertically aligned nematic liquid crystal on anodic porous alumina," *Jpn. J. Appl. Phys.* **43**, L1004 (2004).

[2] K. H. Yang, and C. Rosenblatt, "Determination of the anisotropic potential at the nematic liquid crystal-to-wall interface," *Appl. Phys. Lett.* **43**, 62 (1983).

Tables

Etching time (min.)	diameter (nm)	thickness (nm)	aspect ratio
0.0	13	657	50.54
1.5	60	403	6.72
2.0	65	456	7.02
2.5	84	415	4.94
3.0	92	435	4.73
3.5	88	48	0.55
4.0	80	42	0.53
5.0	83	37	0.45
6.0	85	48	0.56

Table 3-1 The diameter of pores, the thickness of the etched AAO thin film, and the aspect ratio with different etching time.
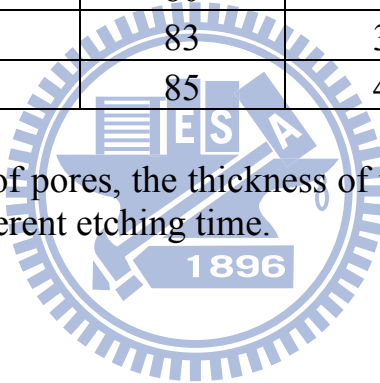
Figures
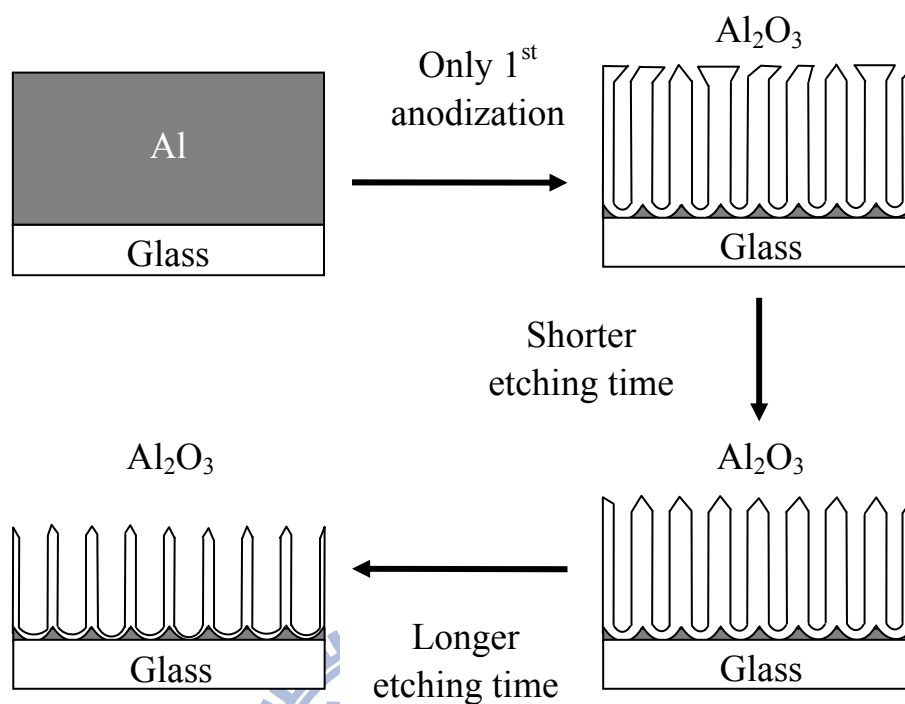
Figure 3-1 Scheme of the experimental procedures for the etched AAO thin films with different etching time.
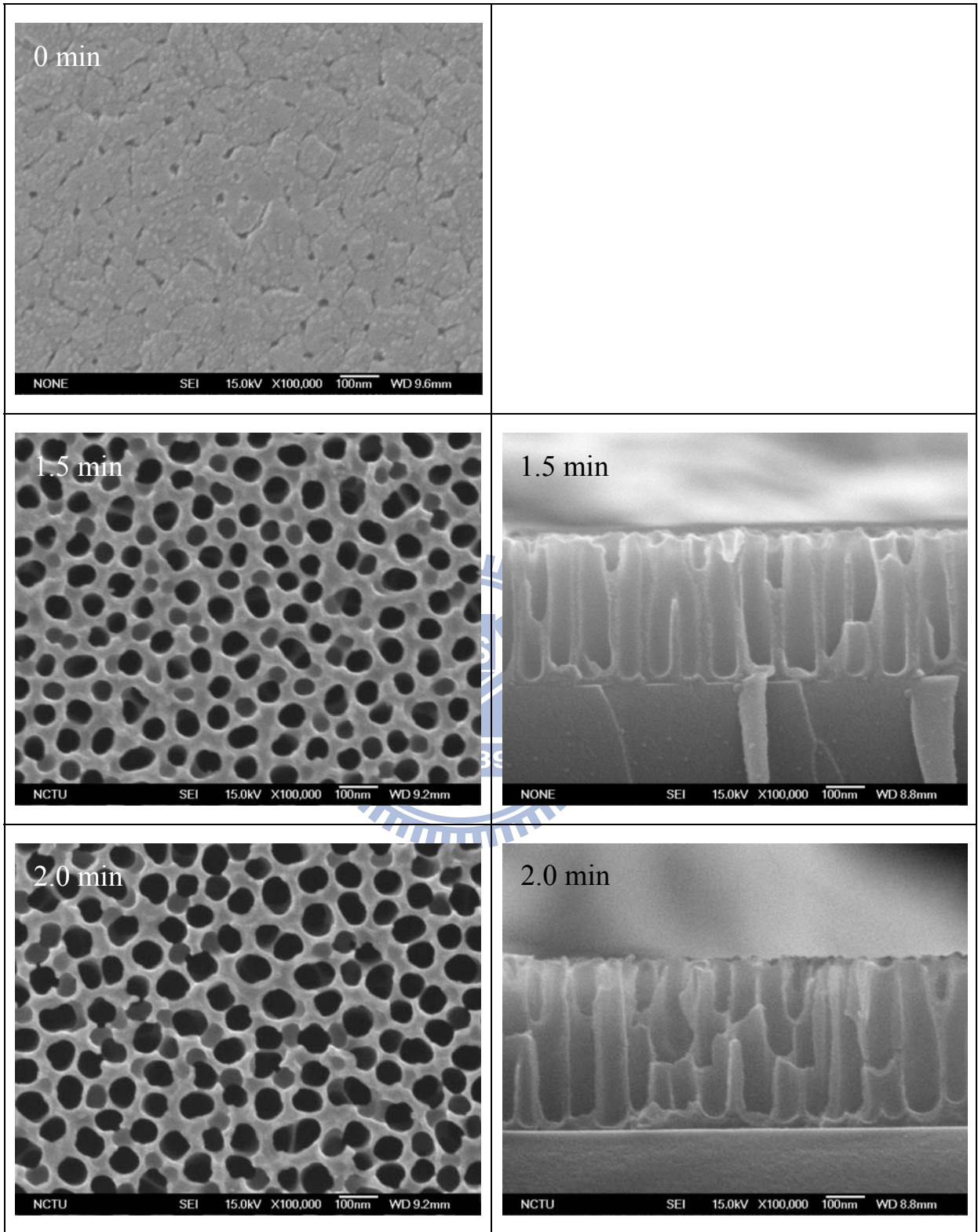
Figure 3-2 FESEM images of the one-step AAO thin film with different etching time. The images in left column are the top view of these thin films. The images in the right column are the side view of these thin films.

Figure 3-2 (cont'd) FESEM images of the one-step AAO thin film with different etching time. The images in left column are the top view of these thin films. The images in the right column are the side view of these thin films.

Figure 3-2 (cont'd) FESEM images of the one-step AAO thin film with different etching time. The images in left column are the top view of these thin films. The images in the right column are the side view of these thin films.
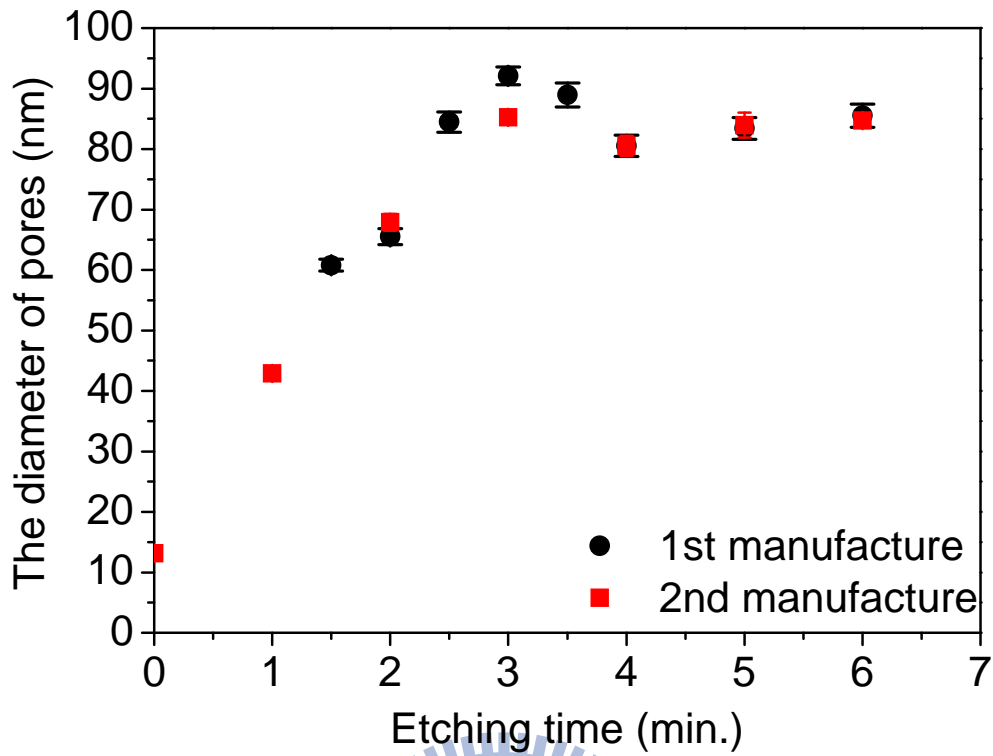
Figure 3-3 The relationship between the diameter of pores and the etching time.
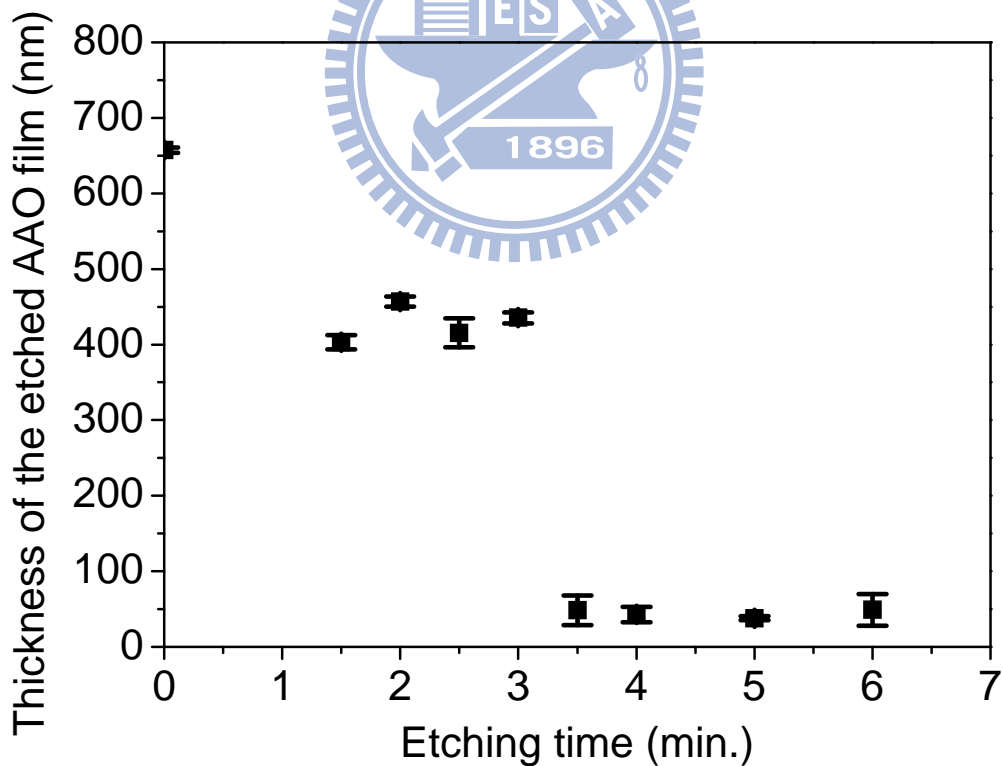
Figure 3-4 Thickness of the etched AAO thin films with different etching time.
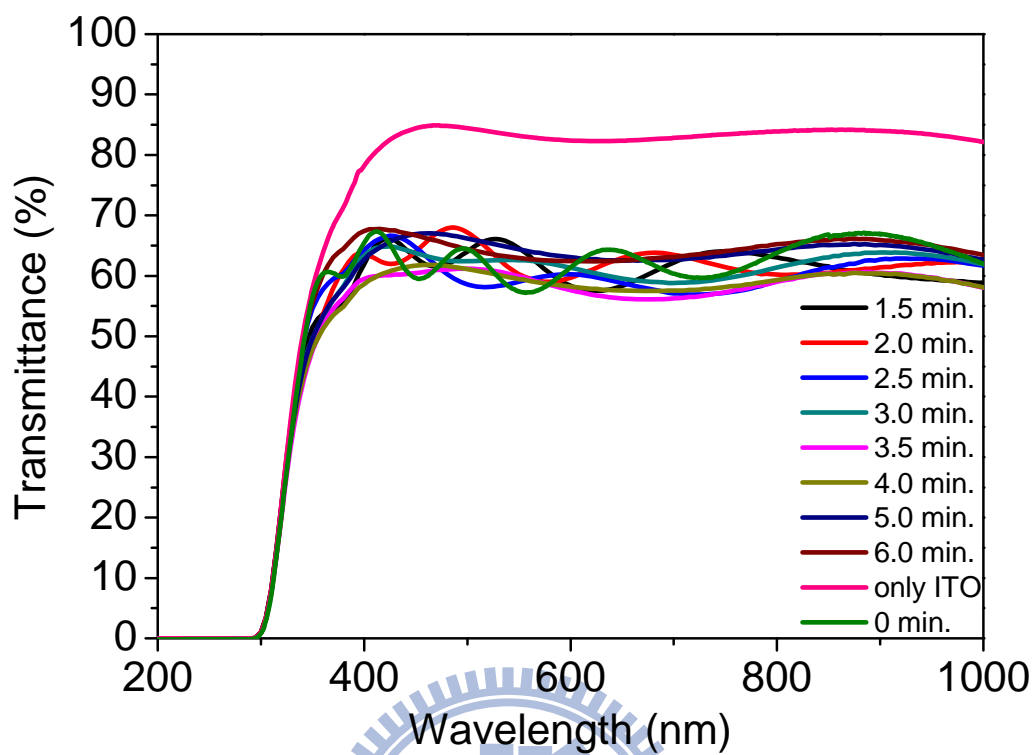
Figure 3-5 Transmittance of the ITO substrates with the etched AAO films with different etching time.

Etching time	0°	45°
0 min		
1.5 min		
2.0 min		
2.5 min		
3.0min		
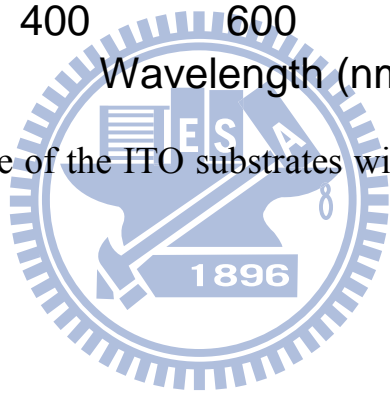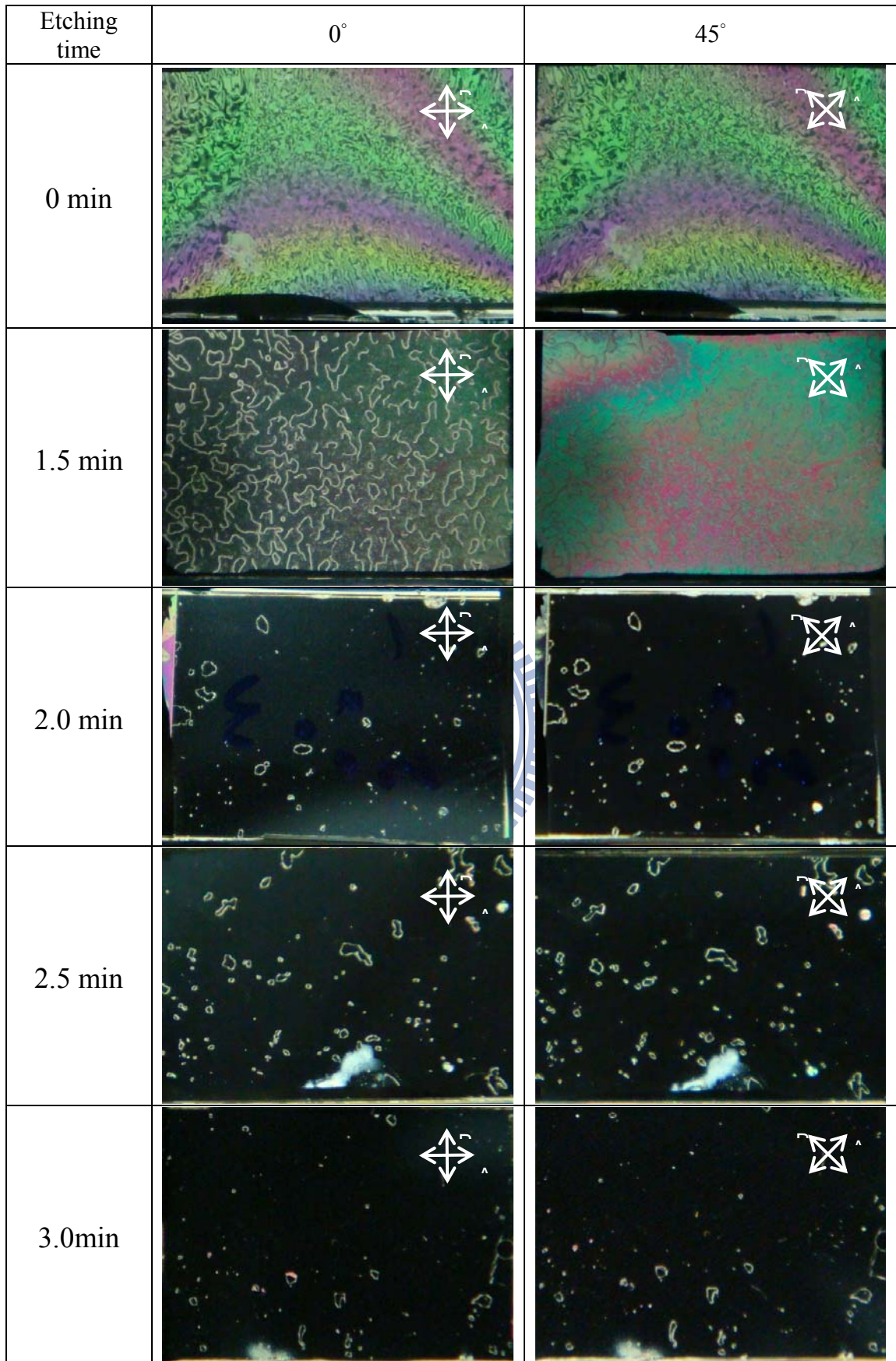
Figure 3-6 Polarizing microscopic images of the liquid crystal cells with the etched AAO thin film as the alignment layer.

Etching time	0°	45°
3.5 min		
4.0 min		
5.0 min		
6.0 min		
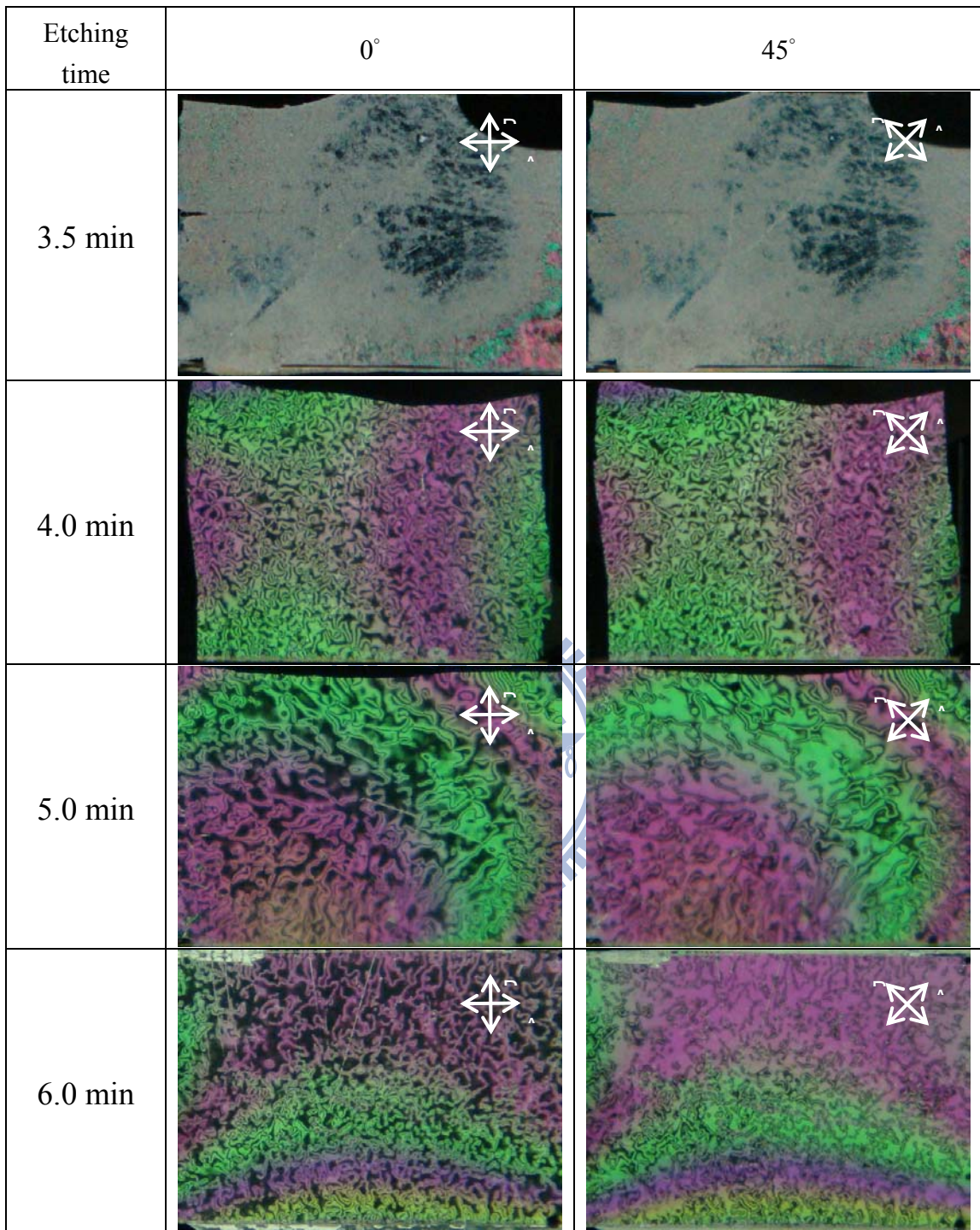
Figure 3-6 (cont'd) The polarizing microscopic images of the liquid crystal cells with the etched AAO thin film as the alignment layer.
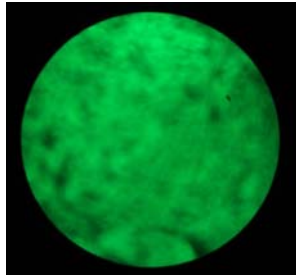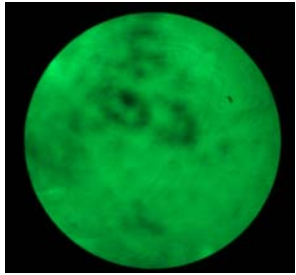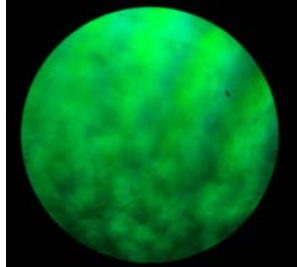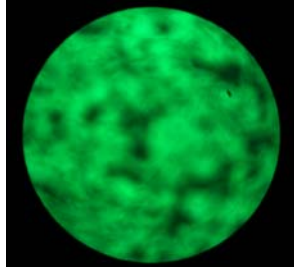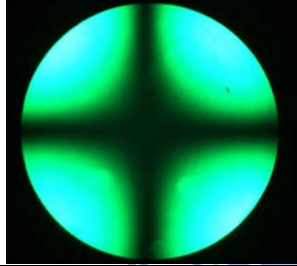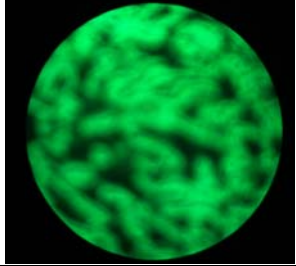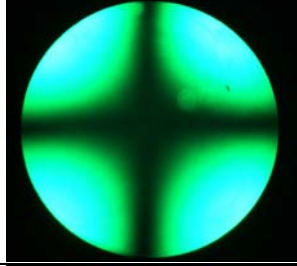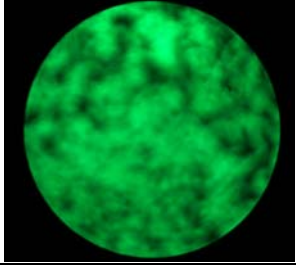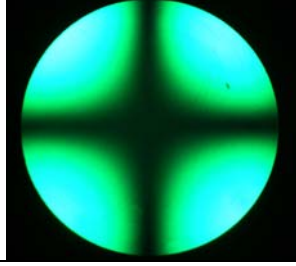
Etching time		Etching time	
0.0 min		3.5 min	
1.5 min		4.0 min	
2.0 min		5.0 min	
2.5 min		6.0 min	
3.0 min			

Figure 3-7 The conoscopic images of the liquid crystal cell with the etched AAO thin film with different etching time.
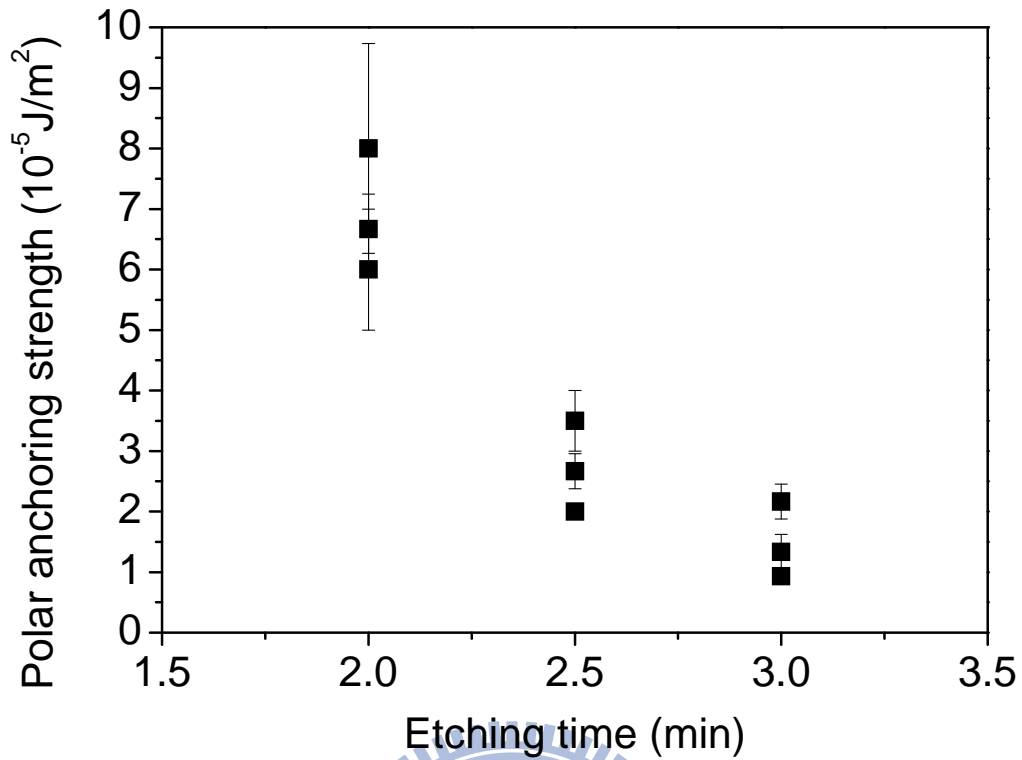
Figure 3-8 The relationship between the polar anchoring strength and the etching time.
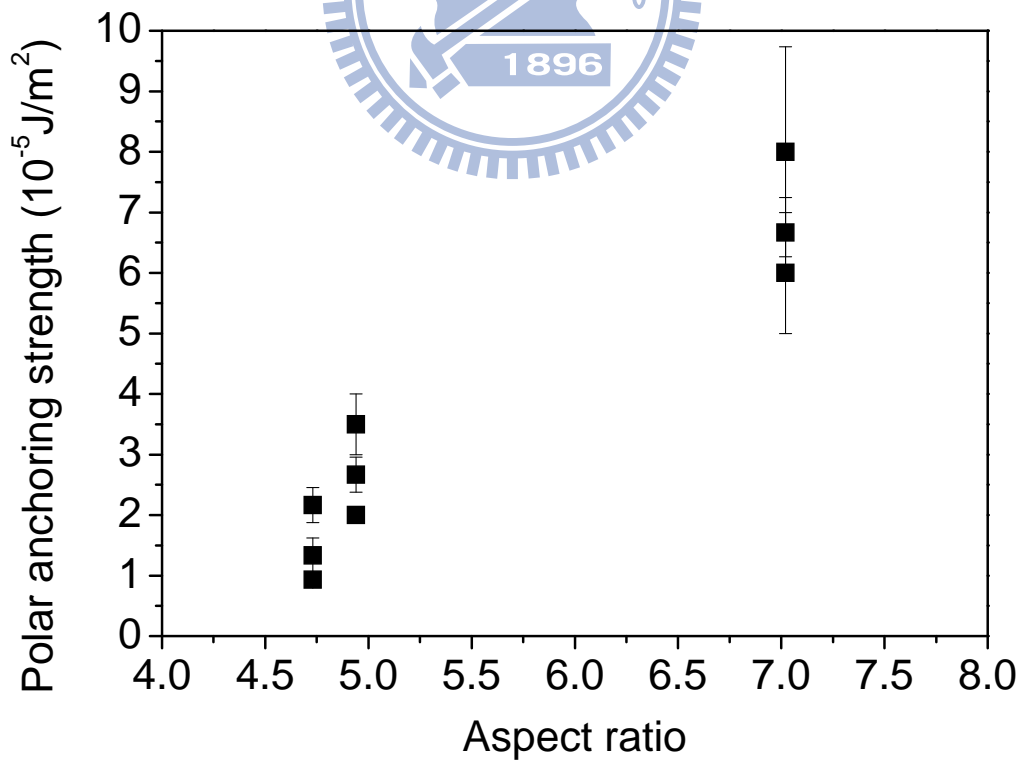
Figure 3-9 The relationship between the polar anchoring strength and the aspect ratio.

Liquid crystal molecules

Porous AAO thin film

l

$2r$

Smaller pore sizes

larger pore sizes
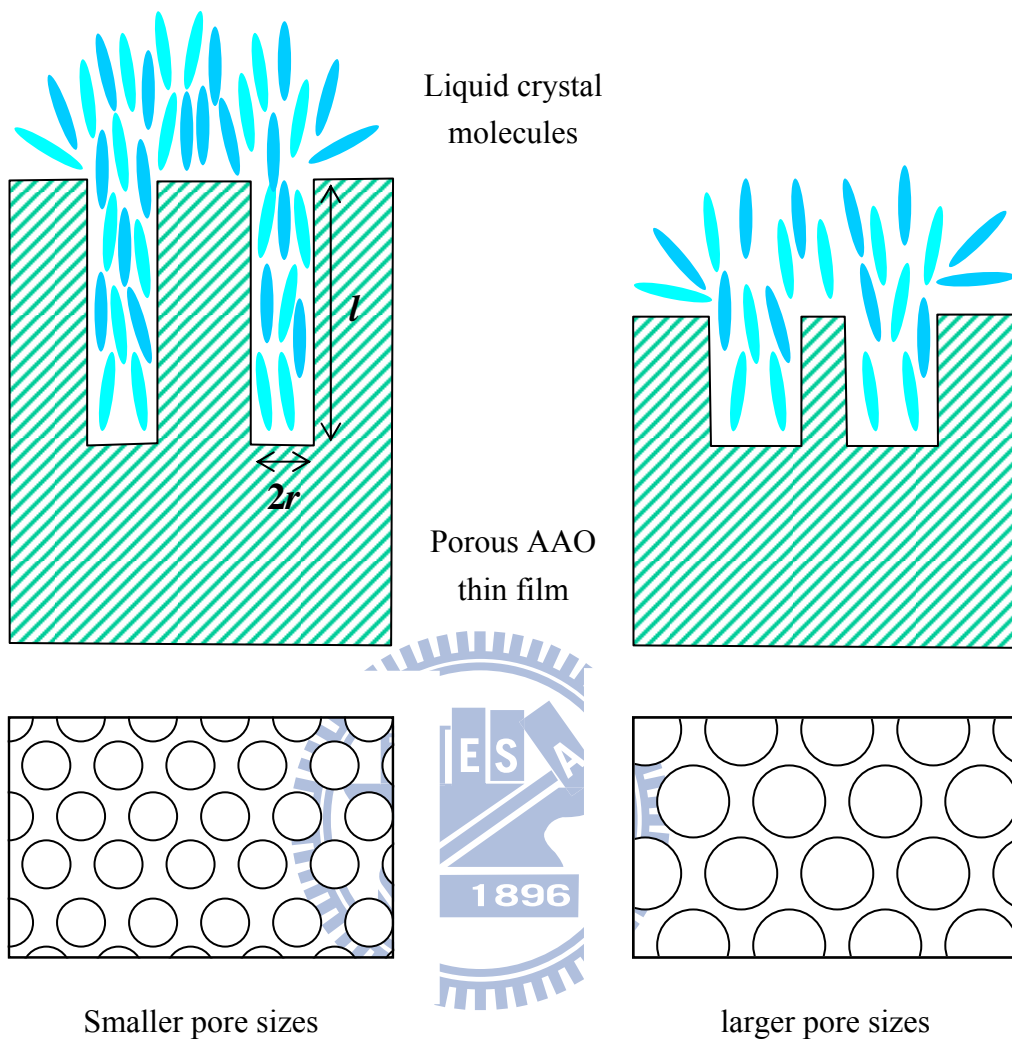
Figure 3-10 Scheme of the possible alignment mechanism.

Chapter 4
The optical constants and birefringence
of the anodic aluminum oxide
in terahertz frequency range

4.1 Overview

Terahertz (THz) waves are the electromagnetic waves sent at frequencies in the terahertz range. It is normally used for the region of the electromagnetic spectrum between 0.1 THz (10^{11} Hz) and 10 THz (10^{13} Hz), corresponding to the sub-millimeter wavelength range between 3 mm and 30 μm. 1 THz is corresponding to 300 μm. Figure 4-1 shows the spectrum of electromagnetic wave.[1] It shows that the THz waves are between the microwave and infrared optical bands. Because of the development of the efficient emitters and detectors, there are a lot of industrial applications in each of the spectral regimes. Before mid-1980s, the efficient THz generators and detectors are short. Most THz sources are low brightness emitters and with narrow band. In order to detect the THz waves, the incoherent detectors such as pyroelectric detectors and bolometers have been used in the past three decade. These conventional incoherent detectors suffer from cryogenic requirement and the noise from the thermal background radiation. Therefore, there was less application in THz regime, called "THz gap".

Since 1990, a breakthrough of the THz technology came with the development of ultrafast lasers delivering femtosecond pulses in the visible and near infrared spectral range. By converting the ultrafast laser pulses in a nonlinear crystal or a photoconductive antenna, it can generate picosecond broadband pulses of terahertz radiation. There are two main mechanisms for the generation of THz radiation: optical rectification[2] and photoconduction[3]. Following, we introduce how to generate and detect the THz wave, the terahertz time-domain

spectroscopy (THz-TDS) system, and how to analyze the optical properties of anodic aluminum oxide in THz regime.

4.2 Terahertz technology

4.2.1 Generation of terahertz wave by using photoconductive antennas

In 1988, Grischkowsky et al. demonstrated the first coherent detection of THz radiation by using the ultrashort pulse and the photoconductive antenna.[4], [5] In order to construct the photoconductive antenna, the photoconductive substrate must have some excellent properties such as short carrier lifetime, high mobility and high breakdown voltage. Table 4-1 shows the characteristics of some photoconductive substrates.[6] In our THz-TDS system, LT-GaAs have been used as the substrate of photoconductive antenna. The structure of the antenna is a Hertzian dipole antenna with a small central gap (d=5 μm) made of AuGe/Ni/Au metal layer.[7] The structure of the photoconductive dipole antenna is shown in Figure 4-2. When the ultrashort pulse or the femtosecond optical pulse with the energy larger than the bandgap of the photoconductive material (E_g=1.43eV for LT-GaAs at room temperature) is incident to photoconductive antenna, the free electrons and holes are excited in the conduction and valence band, respectively. The carriers (electron-hole pairs) are accelerated by the bias electric field, and then decayed with a time constant depended on the carrier lifetime. It results in a pulsed photocurrent in the photoconductive antenna. Because the modulated current is in sub-picosecond regime, it emits a sub-picosecond electromagnetic wave, as THz pulse.

By using the classical Drude model [8], the dynamic behaviors of the free carriers generated by the ultrashort pulses can be described. According to this model, the average velocity of the free carriers is

$$\frac{dv_c(t)}{dt} = -\frac{v_c(t)}{\delta\tau} + \frac{q}{m_c}E(t),$$ (4-1)

where $v_c(t)$ is the average velocity of the carrier, $\delta\tau$ is the carrier collision time, q is the charge of the carrier (an electron or a hole), m_c is the effective mass of the carrier, and $E(t)$ is the biasing electric field.[9] The photocurrent density in the emitter corresponds to the convolution of the temporal shapes of the exciting ultrashort pulses and the impulse current response of the photoconductive antenna. It can be presented as

$$j_c(t) = P_{opt}(t) \otimes [n_c(t)qv_c(t)],$$ (4-2)

where $j_c(t)$ is the photocurrent density, $P_{opt}(t)$ is the optical power of the ultrashort pulses, $\otimes$ denotes the convolution product, and $n_c(t)$ is the density of the photocarriers. The current density $[n_c(t)qv_c(t)]$ represents the impulse response of the photoconductive antenna, i.e., its response to a delta Dirac optical excitation. Here, let us consider the classical dipole emitting antenna [10], which behaves as a Hertizian dipole. Assuming the THz detector is in the far-field range and neglecting the dispersion of the quasi-optical system that focuses the THz beam, the THz field at a distance r $(r \gg \lambda)$ and time t can be presented as

$$E_{THz}(t) = \frac{l_e}{4\pi\varepsilon_0 c^2 r}\frac{dj_c(t)}{dt}\sin\theta \propto \frac{dj_c(t)}{dt}.$$ (4-3)

where l_e is the effective length of the dipole antenna, and θ is the angle from the direction of the dipole antenna. ε_0 and c are the dielectric constant and the velocity of light in vacuum, respectively. Obviously, the THz field is directly proportional to the temporal derivative of the photocurrent density. Figure 4-3 shows the calculated photocurrent in the emitting photoconductive antenna and the amplitude of the THz field versus time. The temporal pulse shape of the ultrashort pulse is shown as a dotted line. [9] It provides that Equation 4-3 is well described. The THz waves generated by this method have average power levels

on the order of nanowatt. The bandwidth of the generated THz wave is primarily limited by how quickly the carriers can accelerate in LT-GaAs substrate, rather than the pulse duration of the ultrashort laser pulse.

4.2.2 Detection of terahertz wave by using photoconductive antennas

After discussing about generating the THz wave by using photoconductive antenna, let us consider the detection of the THz wave in the detecting photoconductive antenna. The physical process in the detecting antenna is very similar to the one in the emitting antenna. The photogenerated free carriers are accelerated by the electric field of the THz wave in the detecting photoconductive antenna. The average velocity of the accelerated carriers obeys to the differential equation

$$\frac{dv_d(t;\Delta t)}{dt} = -\frac{v_d(t;\Delta t)}{\delta\tau_d} + \frac{q}{m_d}E_{THz}(t+\Delta t),\qquad(4\text{-}4)$$

where Δt is the time delay between the optical pulse and the THz wave onto the detector, $v_d(t;\Delta t)$ is the average velocity of the accelerated carriers. $\delta\tau_d$ and m_d are the carriers collision time and the effective mass of the accelerated carriers in the detecting antenna, respectively. $E_{THz}(t+\Delta t)$ is the electric field of the THz wave.

The actual photocurrent density in the detecting antenna is given by the convolution product of the temporal shapes of the ultrashort pulse that triggers the detector and of the impulse response of the photoswitch to a Dirac-like optical excitation. Consequently, the instantaneous photocurrent density in the detector is presented as

$$j_d(t;\Delta t) = P_d(t) \otimes [n_d(t)qv_d(t;\Delta t)].\qquad(4\text{-}5)$$

Furthermore, the measured THz signal corresponds to the average current flowing through the gap of the detecting antenna. Therefore, the measured

photocurrent is given by

$$J_d(\Delta t) \propto \int_{-\infty}^{+\infty} j_d(t;\Delta t)dt$$

$$\propto \int_{-\infty}^{+\infty} dt \int_{-\infty}^{+\infty} P_d(t^{'}) \times [n_d(t-t^{'})qv_d(t-t^{'};\Delta t+t^{'})]dt^{'} \quad .$$

(4-6)

Briefly, the measured photocurrent density $J_d(\Delta t)$ is relative to the THz electric field $E_{THz}(t+\Delta t)$ and the response function of the detector. The transient response of the THz signal is affected by the carrier life time, the transmission characteristics of LT-GaAs, the resonance characteristics of antenna, the pulse shape and the power of the probe beam, and the diffractive effect of the THz beam. The THz electric field generates the current across the gap of photoconductive antenna amplified using a low-bandwidth amplifier, such as Lock-in amplifier. This amplified current corresponds to the THz field strength. Because the carriers in the LT-GaAs substrate have an extremely short lifetime, the THz electric field is only sampled by using an extremely narrow slice, such as the femtosecond pulse. By using this method, it is easy to map the entire THz electric field waveform.

4.2.3 Terahertz time-domain spectroscopy (THz-TDS)

Terahertz time-domain spectroscopy (THz-TDS) is a spectroscopic technique based on generating and detecting electromagnetic transients to probe material properties with the terahertz radiation. This method is sensitive to the sample material's effect on both the amplitude and the phase of the THz radiation. THz-TDS can provide more information than conventional Fourier-transform spectroscopy that is only sensitive to the amplitude.

Figure 4-4 shows a schematic of the experimental setup of the terahertz time-domain spectroscopy system. This system consists of a femtosecond laser (Ti:Sappire laser), two gated photoconductive dipole antennas (an emitter and a detector), a pair of off-axis parabolic mirrors, a optical scanning delay line. The

wavelength and pulse width of the femtosecond laser pulse are 800 nm and 50 fs, respectively. The pulse duration is 80MHz. The emitting photoconductive dipole antenna is biased with a 1kHz-modulation square wave. The bias voltage is 5 Vp-p. A hyper-hemispherical silicon lens is attached to the photoconductive dipole antenna, both of the emitter and the detector. The pair of off-axis parabolic mirrors is for collimating and focusing the terahertz beam. The transient current was induced in the gap of the detecting antenna with the focused THz electric field, which accelerated the photocurrents exited by the probing ultrashort pulse. A digital lock-in amplifier with a current-voltage preamplifier module (Model SR830, Stanford Research System) is connected to the electrodes of the detecting antenna, to synchronously detect the detecting photoconductive current. The THz electric field provides the driving field to the carriers on the detecting photoconductive antenna. Because the detecting electronics are much slower than the THz signals, it is difficult to measure the whole THz transients directly. By scanning the optical delay of the probing arm with respect to the pump arm, the THz signal can be acquired sequentially. The data acquisition and the control of the stepping stage for the delay line are conducted with a LabVIEW program using the GPIB interface. The time dependent electric transient through the gap of the antenna depends on both the magnitude and the direction of THz wave.

Figure 4-5 is the experimental data of the time domain THz signal passing through the atmosphere. The black or red line is the atmosphere signal with or without N2 purged, respectively. After the main signal (~15 ps), the signal fluctuation is shown in the atmosphere signal without N2 purged (red line). This fluctuation is because of the water vapor absorption from the moist atmosphere. On the other hand, the signal in the atmosphere with N2 purged (black line) is much smoother because of the dry air condition (the relative humidity ~ 3 %). By applying Fast Fourier Transform (FFT) to both of the THz time domain signal, the power spectrum in frequency domain is obtained as shown in Figure 4-6. It shows several water vapor absorption peaks below 1.5 THz.[11] The

reliable THz signal is from 0.3 to 3.0THz. The signal and noise ratio is around 107:1.

4.3 Derivation of optical constants in terahertz frequency range

4.3.1 Optical constants of the thin film with substrate

We assume that the THz signal is a plane wave passing through the cell at normal incidence. Figure 4-7 (a) is shown the schematic of the THz wave pathway near the thin film with substrate. The electric field of the THz wave transmitted through a substrate and a thin film can be written as

$$E_{thin\ film}(t) = \int_{-\infty}^{+\infty} E_0(f) \tilde{t}_{AW} e^{i2\pi f(\frac{\tilde{n}_W d_W}{c})} \tilde{t}_{WS} FP_S(f,d_s) e^{i2\pi f(\frac{\tilde{n}_S d_S}{c})} \tilde{t}_{SA} e^{-i2\pi ft} df , \qquad (4-7)$$

where $E_0(f)$ is the electric field of the incident THz wave. d_W and d_S are the thickness of the sample substrate and the thin film, respectively. In Equation 4-7, $\tilde{n}_A = n_A + i\kappa_A$, $\tilde{n}_W = n_W + i\kappa_W$ and $\tilde{n}_S = n_S + i\kappa_S$, are the complex refractive index of air, window and thin film, respectively. The real part of the complex refractive index $\tilde{n}$ is often called simply the refractive index n . The imaginary part κ is called the extinction coefficient. $\tilde{t}_{AW}$, $\tilde{t}_{WS}$ and $\tilde{t}_{SA}$ are the Fresnel transmission coefficient at the air-window, window-thin film and thin film-air interfaces, respectively. These three complex transmission coefficient are presented as

$$\tilde{t}_{AW} = \frac{2 \times \tilde{n}_A}{\tilde{n}_A + \tilde{n}_W} , \quad \tilde{t}_{WS} = \frac{2 \times \tilde{n}_W}{\tilde{n}_W + \tilde{n}_S} \quad \text{and} \quad \tilde{t}_{SA} = \frac{2 \times \tilde{n}_S}{\tilde{n}_S + \tilde{n}_A} . \qquad (4-8)$$

The Fabry-Perot coefficient in the thin film with a thickness of d_S is $FP_S(f,d_S)$, presented as

$$\sum_{m=0}^{N}\left[\widetilde{r}_{SW}^{m}\widetilde{r}_{SA}^{m}e^{i2\pi f(\frac{\widetilde{n}_S d_S}{c}\times 2m)}\right],$$
(4-9)

where $\widetilde{r}_{SW}$ and $\widetilde{r}_{SA}$ are the Fresnel reflection coefficient of the window-sample and sample-air interface, respectively. These two complex reflective coefficients are presented as

$$\widetilde{r}_{SW}=\frac{\widetilde{n}_S-\widetilde{n}_W}{\widetilde{n}_S+\widetilde{n}_W}\quad\text{and}\quad\widetilde{r}_{SA}=\frac{\widetilde{n}_S-\widetilde{n}_A}{\widetilde{n}_S+\widetilde{n}_A}.$$
(4-10)

According to Figure 4-7 (b), the electric field of the THz wave transmitted through only substrate at a frequency f can be obtained as

$$E_{ref}(t)=\int_{-\infty}^{+\infty}E_0(f)\widetilde{t}_{AW}e^{i2\pi f(\frac{\widetilde{n}_W d_W'}{c})}\widetilde{t}_{WA}e^{i2\pi f(\frac{\widetilde{n}_A(d_S+\Delta d)}{c})}e^{-i2\pi ft}df,$$
(4-11)

where d_W' is the thickness of the reference substrate. The complex transmission coefficients $\widetilde{t}_{AW}$ and $\widetilde{t}_{WA}$, which indicate the complex amplitude transmittance at the air-window and window-air interfaces, respectively, are presented as

$$\widetilde{t}_{AW}=\frac{2\times\widetilde{n}_A}{\widetilde{n}_A+\widetilde{n}_W},\text{ and }\widetilde{t}_{WA}=\frac{2\times\widetilde{n}_W}{\widetilde{n}_W+\widetilde{n}_A}.$$
(4-12)

In order to compare two THz signal with each other, the total optical path of these two cases need to be equal.

$$d_W+d_S=d_W'+d_S+\Delta d$$
$$\Delta d=d_W-d_W'$$
(4-13)

Here, Δd is the differential thickness between sample substrate and reference substrate.

The complex transmittance of the sample is presented using Equation (4-7) and (4-11) as,

$$\sqrt{T_{thin\,film}}e^{i(\phi_{thin\,film})}=\frac{E_{thin\,film}(t)}{E_{ref}(t)}$$
$$=\frac{\widetilde{t}_{WS}\widetilde{t}_{SA}}{\widetilde{t}_{WA}}FP_S(f,d_S)e^{i\frac{2\pi f}{c}(\widetilde{n}_W\Delta d+\widetilde{n}_S d_S-\widetilde{n}_A d_S-\widetilde{n}_A\Delta d)}$$
(4-14)

$$= \left[\frac{\widetilde{t}_{WS}\widetilde{t}_{SA}}{\widetilde{t}_{WA}} FP_S(f,d_S) e^{\frac{-2\pi f}{c}[(\kappa_S-\kappa_A)d_S+(\kappa_W-\kappa_A)\Delta d]} \right]$$

$$\times e^{i\frac{2\pi f}{c}[(n_S-n_A)d_S+(n_W-n_A)\Delta d]} \tag{4-14}$$

where $\sqrt{T_{thin\ film}}$ and $\phi_{thin\ film}$ indicate the power transmittance and the phase shift, respectively. According to complex number calculation, we can convert the right part of Equation (4-14) into a point in the complex plane. The radius and angle of this point are presented as the power transmittance and phase shift, respectively.

$$e^{i(\phi_{thin\ film})} = e^{i\arg\left(\frac{\widetilde{t}_{WS}\widetilde{t}_{SA}}{\widetilde{t}_{WA}} \sum_{m=0}^{N}\left[\widetilde{r}_{SW}^m \widetilde{r}_{SA}^m e^{i2\pi f(\frac{\widetilde{n}_S d_S}{c}\times 2m)} \right] \right)} e^{i\frac{2\pi f}{c}[(n_S-n_A)d_S+(n_W-n_A)\Delta d]}$$

$$\sqrt{T_{thin\ film}} = \left| \frac{\widetilde{t}_{WS}\widetilde{t}_{SA}}{\widetilde{t}_{WA}} \sum_{m=0}^{N}\left[\widetilde{r}_{SW}^m \widetilde{r}_{SA}^m e^{i2\pi f(\frac{\widetilde{n}_S d_S}{c}\times 2m)} \right] \right| \times e^{\frac{-2\pi f}{c}[(\kappa_S-\kappa_A)d_S+(\kappa_W-\kappa_A)\Delta d]} \tag{4-15}$$

From Equation (4-15) the complex refractive index $\widetilde{n}_S = n_S + i\kappa_S$ is derived as follows,

$$n_S = \frac{1}{2\pi f \frac{d_S}{c}}\left[(\phi_{thin\ film}) - \arg\left(\frac{\widetilde{t}_{WS}\widetilde{t}_{SA}}{\widetilde{t}_{WA}} \sum_{m=0}^{N}\left[\widetilde{r}_{SW} \widetilde{r}_{SA} e^{i4\pi f(\frac{\widetilde{n}_S d_S}{c})} \right]^m \right) \right] + n_A - \frac{(n_W-n_A)\Delta d}{d_S}$$

$$\kappa_S = \frac{1}{-2\pi f \frac{d_S}{c}}\ln\left[\frac{\sqrt{T_{thin\ film}}}{\frac{\widetilde{t}_{WS}\widetilde{t}_{SA}}{\widetilde{t}_{WA}} \sum_{m=0}^{N}\left[\widetilde{r}_{SW} \widetilde{r}_{SA} e^{i4\pi f(\frac{\widetilde{n}_S d_S}{c})} \right]^m} \right] + \kappa_A + \frac{(\kappa_W-\kappa_A)\Delta d}{d_S} \tag{4-16}$$

Most of the THz-TDS system is operated in the atmosphere at room temperature. The complex refractive index of air $\widetilde{n}_A = 1$ is assumed. Because of the N$_2$ purged, the absorption coefficient $\widetilde{\kappa}_A = 0$ is also assumed. In this work, the windows are fused silica, and the complex refractive index $\widetilde{n}_W$ is given by $n_W = 1.95$ and $\kappa_W = 0.003$.

For optically thick film ($n_S d_S >2.25$ mm), the echoes of THz waves from the multiple reflections of the film are temporally well separated from the main signal. The temporal difference between the main signal and the first reflective signal is larger than 15 ps. These can be easily removed without affecting accuracies of the

measurements. Thus we can set the Fabry-Perot term, $FP_S(f, d_S)$, equal to 1 in Equeation. (4-14).

4.3.2 Optical constants of the liquid crystal cell with two substrates

For the liquid crystal cell, the THz wave pathway is similar. Figure 4-8 (a) is shown the schematic of the THz wave pathway through the liquid crystal cell with two substrates. The electric field of the THz wave can be presented as

$$E_{LC}(t) = \int_{-\infty}^{+\infty} E_0(f)\tilde{t}_{AW} e^{i2\pi f(\frac{\tilde{n}_W d_{W1}}{c})}\tilde{t}_{WS} FP_{LC}(f, d_S) e^{i2\pi f(\frac{\tilde{n}_S d_S}{c})}\tilde{t}_{SW} e^{i2\pi f(\frac{\tilde{n}_W d_{W2}}{c})}\tilde{t}_{WA} e^{-i2\pi ft} df \tag{4-17}$$

where $E_0(f)$ is the electric field of the incident THz wave. d_{W1} and d_{W2} are the thickness of the first and second sample substrate, respectively. d_S is the thickness of the liquid crystal layer. In Equation 4-16, $\tilde{n}_A = n_A + i\kappa_A$, $\tilde{n}_W = n_W + i\kappa_W$ and $\tilde{n}_S = n_S + i\kappa_S$, are the complex refractive index of air, window and thin film, respectively. $\tilde{t}_{AW}$, $\tilde{t}_{WS}$, $\tilde{t}_{SW}$ and $\tilde{t}_{WA}$ are the Fresnel transmission coefficient at the air-window, window-liquid crystal, liquid crystal-window and window-air interfaces, respectively. These four complex transmission coefficient are presented as

$$\tilde{t}_{AW} = \frac{2 \times \tilde{n}_A}{\tilde{n}_A + \tilde{n}_W}, \quad \tilde{t}_{WS} = \frac{2 \times \tilde{n}_W}{\tilde{n}_W + \tilde{n}_S}, \quad \tilde{t}_{SW} = \frac{2 \times \tilde{n}_S}{\tilde{n}_S + \tilde{n}_W} \quad \text{and} \quad \tilde{t}_{WA} = \frac{2 \times \tilde{n}_W}{\tilde{n}_W + \tilde{n}_A}. \tag{4-18}$$

$\tilde{r}_{SW}$ is the Fresnel reflection coefficient of the liquid crystal-window interface. This complex reflective coefficient is presented as

$$\tilde{r}_{SW} = \frac{\tilde{n}_S - \tilde{n}_W}{\tilde{n}_S + \tilde{n}_W}. \tag{4-19}$$

The Fabry-Perot coefficient in the liquid crystal layser with a thickness of d_S is $FP_{LC}(f, d_S)$, presented as

$$\sum_{m=0}^{N} \left[\tilde{r}_{SW}^{2m} e^{i2\pi f \left(\frac{\tilde{n}_S d_S}{c} \times 2m \right)} \right]. \tag{4-19}$$

According to Figure 4-8 (b), the electric field of the THz wave transmitted through only substrate at a frequency f can be obtained as

$$E_{ref}(t) = \int_{-\infty}^{+\infty} E_0(f) \tilde{t}_{AW} e^{i2\pi f \left(\frac{\tilde{n}_W d_{W3}}{c} \right)} e^{i2\pi f \left(\frac{\tilde{n}_W d_{W4}}{c} \right)} \tilde{t}_{WA} e^{i2\pi f \left(\frac{\tilde{n}_A (d_S + \Delta d)}{c} \right)} e^{-i2\pi ft} df, \tag{4-20}$$

where d_{W3} and d_{W4} are the thickness of the two reference substrate. The complex transmission coefficients $\tilde{t}_{AW}$ and $\tilde{t}_{WA}$, which indicate the complex amplitude transmittance at the air-window and window-air interfaces, respectively, are presented as

$$\tilde{t}_{AW} = \frac{2 \times \tilde{n}_A}{\tilde{n}_A + \tilde{n}_W}, \text{ and } \tilde{t}_{WA} = \frac{2 \times \tilde{n}_W}{\tilde{n}_W + \tilde{n}_A}. \tag{4-21}$$

Let $d_W = d_{W1} + d_{W2}$ and $d_W' = d_{W3} + d_{W4}$. In order to compare two THz signal with each other, the total optical path of these two cases need to be equal.

$$\begin{aligned} d_W + d_S &= d_W' + d_S + \Delta d \\ \Delta d &= d_W - d_W' \end{aligned} \tag{4-22}$$

Here, Δd is the total differential thickness between sample substrate and reference substrate.

The complex transmittance of the sample is presented using Equation (4-17) and (4-20) as,

$$\begin{aligned} \sqrt{T_{LC}} e^{i(\phi_{LC})} &= \frac{E_{LC}(t)}{E_{ref}(t)} \\ &= \tilde{t}_{WS} \tilde{t}_{SW} FP_{LC}(f, d_S) e^{i\frac{2\pi f}{c} \left(\tilde{n}_W (d_{W1} + d_{W2}) + \tilde{n}_S d_S - \tilde{n}_W (d_{W3} + d_{W4}) - \tilde{n}_A (d_S + \Delta d) \right)} \\ &= \tilde{t}_{WS} \tilde{t}_{SW} FP_{LC}(f, d_S) e^{i\frac{2\pi f}{c} \left(\tilde{n}_W d_W + \tilde{n}_S d_S - \tilde{n}_W d_W' - \tilde{n}_A (d_S + \Delta d) \right)} \\ &= \tilde{t}_{WS} \tilde{t}_{SW} FP_{LC}(f, d_S) e^{i\frac{2\pi f}{c} \left(\tilde{n}_W \Delta d + \tilde{n}_S d_S - \tilde{n}_A d_S - \tilde{n}_A \Delta d \right)} \end{aligned} \tag{4-23}$$

$$= \left[\tilde{t}_{WS}\tilde{t}_{SW} FP_{LC}(f,d_S)e^{\frac{-2\pi f}{c}[(\kappa_S-\kappa_A)d_S+(\kappa_W-\kappa_A)\Delta d]} \right]$$

$$\times e^{i\frac{2\pi f}{c}[(n_S-n_A)d_S+(n_W-n_A)\Delta d]} \tag{4-23}$$

where $\sqrt{T_{LC}}$ and ϕ_{LC} indicate the power transmittance and the phase shift, respectively. According to complex number calculation, we can convert the right part of Equation (4-23) into a point in the complex plane. The radius and angle of this point are presented as the power transmittance and phase shift, respectively.

$$e^{i(\phi_{LC})} = e^{i\arg\left(\tilde{t}_{WS}\tilde{t}_{SW} \sum\limits_{m=0}^{N}\left[\tilde{r}_{SW}^{2m}e^{i2\pi f(\frac{\tilde{n}_S d_S}{c}\times 2m)} \right] \right)} e^{i\frac{2\pi f}{c}[(n_S-n_A)d_S+(n_W-n_A)\Delta d]}$$

$$\sqrt{T_{LC}} = \left| \tilde{t}_{WS}\tilde{t}_{SW} \sum\limits_{m=0}^{N}\left[\tilde{r}_{SW}^{2m}e^{i2\pi f(\frac{\tilde{n}_S d_S}{c}\times 2m)} \right] \right| \times e^{\frac{-2\pi f}{c}[(\kappa_S-\kappa_A)d_S+(\kappa_W-\kappa_A)\Delta d]} \tag{4-24}$$

From Equation (4-24) the complex refractive index $\tilde{n}_S = n_S + i\kappa_S$ is derived as follows,

$$n_S = \frac{1}{2\pi f \dfrac{d_S}{c}}\left[(\phi_{LC}) - \arg\left(\tilde{t}_{WS}\tilde{t}_{SW}\sum\limits_{m=0}^{N}\left[\tilde{r}_{SW}e^{i2\pi f(\frac{\tilde{n}_S d_S}{c})} \right]^{2m} \right) \right] + n_A - \frac{(n_W-n_A)\Delta d}{d_S}$$

$$\kappa_S = \frac{1}{-2\pi f \dfrac{d_S}{c}}\ln\left[\frac{\sqrt{T_{LC}}}{\tilde{t}_{WS}\tilde{t}_{SW}\sum\limits_{m=0}^{N}\left[\tilde{r}_{SW}e^{i2\pi f(\frac{\tilde{n}_S d_S}{c})} \right]^{2m}} \right] + \kappa_A + \frac{(\kappa_W-\kappa_A)\Delta d}{d_S} \tag{4-25}$$

Most of the THz-TDS system is operated in the atmosphere at room temperature. The complex refractive index of air $\tilde{n}_A = 1$ is assumed. Because of the N_2 purged, the absorption coefficient $\tilde{\kappa}_A = 0$ is also assumed. In this work, the windows are fused silica, and the complex refractive index $\tilde{n}_W$ is given by $n_W = 1.95$ and $\kappa_W = 0.003$.

4.3.3 Attenuation coefficient

The attenuation coefficient is a basic physical quantity used in calculations of the penetration or the absorbance of materials by electromagnetic wave or other

energy beams. It is also called the absorption coefficient. According to the Beer-Lambert law, the transmittance T can be written as

$$T = \frac{I}{I_0} = 10^{-\alpha L} = e^{-\alpha' L},$$ (4-26)

where I and I_0 are the intensity of the transmitting electromagnetic wave and the incident electromagnetic wave, respectively. L is the distance that the electromagnetic wave pass through the material. α and α' are both absorption coefficient of the material, and

$$\alpha = \frac{\alpha'}{\ln 10} = \frac{\alpha'}{2.30}.$$ (4-27)

The interrelationship between the absorption coefficient α' and the extinction coefficient κ is

$$\alpha' = \frac{4\pi\kappa}{\lambda} = \frac{4\pi\kappa}{c/f} = \frac{4\pi f}{c}\kappa.$$ (4-28)

In this work, the absorption coefficient is defined with the logarithmic base 10 instead of Napier number e. Therefore, the absorption coefficient α can be presented as

$$\alpha = \frac{4\pi f}{c\ln 10}\kappa.$$ (4-29)

4.4 Results and discussions

4.4.1 Water vapor absorption in THz range

In order to check the quality of the THz-TDS system, the water vapor absorption is measured before using this THz-TDS system. Figure 4-9 shows the spectrum of the water vapor absorption peak in THz region. The upper graph is the power spectrum of moist air (r.h.~65%) and N_2 purged air (r.h.~3%). The water vapor absorption peak is clearly shown in power spectrum. By using the N_2 purged air as a reference, the transmittance and the phase difference are shown in the middle and lower graphs, respectively. The black line in the middle graph is the absorbance spectrum of water vapor in Ref. [12]. Here, we read out the entire

water vapor absorption peak from Figure 4-9, and compare with the data shown in Ref. [11] and Ref. [12]. Table 4-2 shows the water vapor absorption lines in THz region. Most of the water vapor absorption lines are the same in Ref. [11], Ref. [12], and our spectrum. For the water vapor absorption line at 1.113 THz, it is shown in both Ref. [11] and Ref. [12], not shown in our spectrum. The absorption line at 1.113 THz is smaller than the line at 1.097 THz. In our spectrum, it is including in the absorption line at 1.105 THz. By using our THz-TDS system, the additional water vapor absorption lines between 1.5 THz and 2.0 THz are shown in Table 4-2. It is clearly shown the realizable spectrum is between 0.1 THz and 2.0 THz.

4.4.2 Optical constants of the fused silica substrate

In this work, most of the substrates used in THz region are fused silica. In order to understand the property of fused silica, the optical constants of the fused silica are taken by using THz-TDS system. Figure 4-10 shows the optical constants of 1 mm fused silica substrate (d = 1.034 mm) in THz region. Considering the multiple reflections, the Fabry-Perot effect, the optical constants are shown by the black line. The red lines are the optical constants without considering the Fabry-Perot effect. After considering the Fabry-Perot effect in calculating the optical constants, the fluctuations from the multiple reflections are reduced a lot. Even if the Fabry-Perot effect is considered in calculating the optical constants, the small fluctuation is shown in the spectrum, regardless of the refractive index, the extinction index, or the absorption coefficient. That is because the thickness difference between the real and the measured thickness of the fused silica substrate. The accuracy of the screw-micrometer used to measure the thickness of the substrate is 1 μm.

In order to cancel the Fabry-Perot effect, the optical constants are measured by using the thicker substrate. Figure 4-11 shows the optical constants of 3 mm fused silica substrate (d = 3.174 mm). The refractive index n is 1.955 between

0.2 THz and 2.0 THz, shown in the upper graph of Figure 4-11. In the middle graph of Figure 4-11, the extinction index κ is around 0.005. According to the relationship between the extinction index κ and the absorption coefficient α, Equation (4-29), the absorption coefficient is proportional to the frequency, and slowly increases from 0 cm^{-1} to 6 cm^{-1} between 0.2 THz and 2.0 THz.. According to the spectrum of fused silica substrate, there is no any obvious absorption peak and the refractive index is constant between 0.2 THz and 2.0 THz. It shows fused silica is a good candidate for substrate in the THz experiment.

4.4.3 Optical constants of the anodic aluminum oxide

The thickness of the AAO thin film is around 500 nm which is much shorter than the wavelength of the terahertz wave. It is difficult to measure the optical constants by using the ultrathin AAO layer as the sample. In order to determine the optical constants of the AAO material in THz region, the commercial AAO substrate from Whatman International Ltd is used. The Anopore™ inorganic membrane (Anodisc™) is designed for a wide range of laboratory filtration applications. The precise pore structure and narrow pore size distribution of the Anopore membrane ensure a high level of particle removal efficiency. Microorganisms and particulate material are captured on the surface of the membrane for subsequent analysis by traditional optical or electron microscopy. When the Anopore membrane is wet, the membrane is virtually transparent and the retained particles do not need to be transferred to another surface before microscopic examination. Here, we choose two different pore sizes, 20 nm and 100 nm, to exam the optical constants in THz region. The thickness of the Anopore membrane is around 60 μm for both substrates.

Figure 4-12 shows the optical constants of the Anopore membrane. The black and red lines are the optical spectrums of the Anopore membrane with 100 nm and 20 nm pores, respectively. For 100 nm, the refractive index is around 1.8. For 20 nm, the refractive index is around 2.1. According to the attenuation

coefficient, there is no obvious absorption peak for both 100 nm and 20 nm. The difference of the refractive index between 100 nm and 20 nm is because of the different pore sizes. The substrate with smaller pore size has higher density and the refractive index is larger for the higher density AAO substrate. The upper graph in Figure 4-12 shows the refractive index of 20-nm AAO substrate is larger than the refractive index of 100-nm AAO substrate. Therefore, the AAO thin films are transparent at THz region and can be used as the alignment layers. The crystalline Al_2O_3, Sapphire, has birefringence. The refractive indices of Sapphire for ordinary ray n_o and for extraordinary ray n_e are 3.07 and 3.41 at 1 THz, respectively.[15] Here, the AAO is not crystalline Al_2O_3 and a macroscopically isotropic material. The dielectric constant of the bulk polycrystalline Al_2O_3 is 9.31 for 0.5-2.0 THz.[16] A published refractive index value of the bulk Al_2O_3 is 3.17 at THz region.[17] The refractive index of the porous AAO thin film is between 1.8 and 2.1 depending on the porosity, which means pore sizes and pore density.

The most commonly used model for the porous materials is the Maxwell-Garnett model. There are two theoretical cases need to be considered. One, denoted as M-G max case, is the air included in the porous AAO substrate, which leads to a relatively larger refractive index n_{max}. The other, denoted as M-G min case, is considered as the AAO spheres in air, which is with a relatively smaller refractive index n_{min}. The effective medium model, which means a mixture of the compounds at the molecular size, derived from the Clausius-Mossoti equation. Here, the smaller refractive index n_{min} is the same as the effective refractive index calculated by using the effective medium model. The relationship between the refractive index n and the dielectric constant ε can be written as

$$n = \sqrt{\varepsilon} . \qquad (4\text{-}30)$$

According to the Maxwell-Garnett theory, the dielectric constant of the

porous AAO substrate can be written as

$$\varepsilon_{min} = 1 + \frac{3(1-p)(\varepsilon_{bulk}-1)}{3+p\varepsilon_{bulk}-p}$$

$$\varepsilon_{max} = \varepsilon_{bulk}\left(1 + \frac{3p(1-\varepsilon_{bulk})}{1+2\varepsilon_{bulk}-p(1-\varepsilon_{bulk})}\right)$$

(4-31)

where ε_{min} and ε_{max} are the effective dielectric constant (permittivity) of the porous AAO substrate in M-G min and M-G max case, respectively. ε_{bulk} is the dielectric constant of the bulk AAO substrate, and p is the porosity. Figure 4-13 shows the relationship between the refractive index and the porosity. The blue solid line is the refractive index n_{max} in the M-G max case. The blue dot line is the refractive index n_{min} in the M-G min case. The effective refractive index should be between n_{max} and n_{min}. According to the Figure 4-12, the refractive indies of the porous AAO substrate, from 1.8 to 2.1, have been drawn as the black and red dash line in Figure 4-13, respectively. It clearly shows that the porosity is between 29% and 52% for the porous AAO substrate with 20-nm pore sizes. For the 100-nm porous AAO substrate, the porosity is between 42% and 66%. It is consistent that the AAO substrates with smaller pore sizes have higher porosity. Further researches, such as the FESEM image and the pore density, need to be investigated to know the practical porosity.

4.4.4 Optical constants of the ferroelectric liquid crystal

The optical constants analysis can also be used in determining the optical constants of ferroelectric liquid crystal (FLC) in THz region. The FLC cell was prepared by sandwiching the commercial available FLC, ZLI-4654-000 (from Merck co.) between two fused silica windows. This FLC has a SmC* phase between -10 and 65°C and a SmA* phase between 65 and 69°C. Homogenous alignment of the FLC was achieved by rubbing the substrates that was coated with polyimide (SE-130B, Nissan). Precision-machined copper pieces, 289±4

μm in thickness, were used both as spacers and electrodes for biasing the FLC cell up to 1500 Volts. The cell was mounted in a copper block for which the temperature can be varied and maintained within ± 0.1 °C. The configuration of the cell and its geometry with respect to the incident terahertz wave are shown in Figure 4-14.

In Figure 4-15, the THz-band real extraordinary and ordinary indices of refraction of the FLC in both the SmA* phase (67.9 °C) and the SmC* phase (58.1°C) are shown. In the 0.3 to 3.0 THz range, we determine that n_e varies between 1.54 and 1.59, while n_o varies from 1.44 to 1.52 for the SmA* phase. For the SmC* phase, n_e = 1.56 ~1.64, and n_o = 1.44 ~ 1.51. The birefringence of ZLI-4654-000, $\Delta n = n_e - n_o$, is thus between 0.03 and 0.16, depending on the phase and frequency. In comparison, the birefringence for the FLC in the visible region is reported to be 0.13 at 589 nm, according to the Merck data sheet.

In Figure 4-16, we illustrate the imaginary indices of refraction of the FLC in the SmA* phase, κ_e and κ_o, the absorption coefficients, α_e and α_o, together with the real indices. Corresponding data for the SmC* phase are shown in Figure 4-17. The imaginary indices are in general less than 0.06, while the corresponding absorption coefficients of the FLC are found to be less than 5 cm-1 below 1 THz. Several broad absorption features can be discerned. The dashed lines in Figure 4-16 indicate the absorption peaks at 1.4 THz for e-waves and 1.75 THz for o-waves, which coincide with anomalous dispersion region of the FLC in the SmA* phase, as expected. The same absorption peak for o-wave is also observed in the SmC* phase as indicated by the dashed line in Figure 4-17. Further work is in progress for the identification of these absorption features. We note that the data reported beyond 2.5 THz are less accurate due to the signal-to-noise limitation of the THz time-domain spectrometer.

4.5 Summaries

We have successfully developed an optical constants analysis program to Fast Fourier Transfer the time-domain signal of THz field and calculate the complex refractive index and the attenuation coefficient. In this work, the water vapor absorption peaks and the optical constants of the fused silica substrate are investigated and compare with the other group's data. It shows the optical constants analysis program is suitable to analyze the THz-TDS signal. On the other hand, the optical constants of the AAO substrate are measured and it shows that the AAO material is a good candidate for the inorganic alignment layer in THz region. By using this technology, the optical constants of the ferroelectric liquid crystal are investigated. Several broad absorption features can be discerned, for example, the ones near 1.4 and 1.75 THz in the SmA* phase. The present study indicates that ferroelectric liquid crystals are also potentially useful for device applications in the THz frequency range. Faster response than that of devices based on nematic liquid crystals is expected.
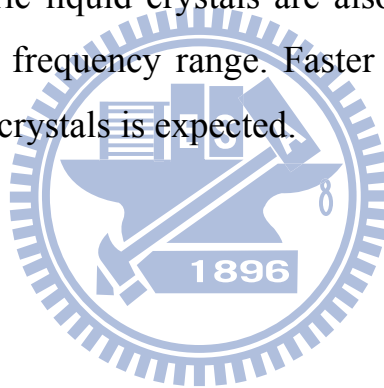
References

[1] B. Ferguson, and X.-C. Zhang, "Materials for terahertz science and technology," *Nat. Mater.* **1**, 26 (2002).

[2] B. Greene, P. Sateta, D. Dykaar, S. Schmitt-Rink, and S. L. Chuang, "Far-infrared light generation at semiconductor surface and its spectroscopic applications," *IEEE J. Quantum Electron* **28**, 2302 (1992).

[3] X.-C. Zhang, "Generation and detection of terahertz electromagnetic pulses from semiconductors with femtosecond optics," *J. Luminescence* **66/67**, 488 (1996).

[4] Ch. Fattinger, D. Grischkowsky, "Point source terahertz optics," *Appl. Phys. Lett.* **53**, 1480 (1988).

[5] M. van Exter, D. Grischkowsky, "Characterization of an optoelectronic terahertz beam system," *IEEE Trans. Microwave Theory Tech.* **38**, 1684 (1990).

[6] K. Sakai (Ed.), "*Terahertz Optoelectronics*," Chapter 1 Introduction to Terahertz Pulses, Springer, (2004).

[7] D. H. Auston, K. P. Chueng, and P. R. Smith, "Picosecond photoconducting Hertzian dipoles," *Appl. Phys. Lett.* **45**, 284 (1984).

[8] D. Grischkowsky, S. Keiding, M. van Exter, and Ch. Fattinger, "Far-infrared time-domain spectroscopy with terahertz beams of dielectrics and semiconductors," *J. Opt. Soc. Am. B* **7**, 2006 (1990).

[9] L. Duvillaret, F. Garet, J.-F Roux, and J.-L Coutaz, "Analytical modeling and optimization of terahertz time-domain spectroscopy experiments, using photoswitches as antennas," *IEEE Journal on Selected Topics in Quantum Electronics* **7**, 615 (2001).

[10] M. van Exter, Ch. Fattinger, and D. Grischkowsky, "High brightness terahertz beams characterized with an ultrafast detector," *Appl. Phys. Lett.*

55, 337 (1989).

[11] M. van Exter, Ch. Fattinger, and D. Grischkowsky, " Terahertz time-domain spectroscopy of water vapor," *Optics Letters* **14**, 1128 (1989).

[12] V. B. Podobedov, D. F. Plusquellic, and G.T. Fraser, "Investigation of the water-vapor continuum in the THz region using a multipass cell," *Journal of Quantitative Spectroscopy and Radiative Transfer* **91**, 287 (2005).

[13] C. M. Randall, and R. D. Rawcliffe, "Refractive indices of Germanium, Silicon, and Fused Quartz in the far infrared," *Appl. Opt.* **6**, 1889 (1967).

[14] D. Grischkowsky, S. Keiding, M. van Exter, and Ch. Fattinger, "Far-infrared time-domain spectroscopy with terahertz beams of dielectrics and semiconductors," *J. Opt. Soc. Am. B* **7**, 2006 (1990).

[15] E. E. Russell and E. E. Bell, "Optical Constants of Sapphire in the Far Infrared," *J. Opt. Soc. Am.* **57**, 543 (1967).

[16] P. H. Bolivar, M. Brucherseifer, J. G. Rivas, R. Gonzalo, A. L. Reynolds, M. Holker, and P. de Maagt, "Measurement of the dielectric constant and loss tangent of high dielectric-constant materials at terahertz frequencies," *IEEE Transactions on Microwave Theory and Techniques* **51**, 1062 (2003).

[17] F. Rutz, M. Koch, L. Micele, and G. De Portu, "Ceramic dielectric mirrors for terahertz range," *Appl. Opt.* **45**, 8070 (2006).

[18] S. Labbé-Lavigne, S. Barret, F. Garet, L. Duvillaret, and J.-L Coutaz, "Far-infrared dielectric constant of porous silicon layers measured by terahertz time-domain spectroscopy," *J. Appl. Phys.* **83**, 6007 (1998).

Tables

Photoconductive materials	Carrier lifetime (ps)	Mobility $(cm^2/(V \cdot s))$	Resistivity $(\Omega \cdot cm)$ (Breakdown field, V/cm)	Band gap (eV at R.T.)
Cr:doped SI-GaAs	50–100.0	$\approx 1\,000$	10^7	1.43
LT-GaAs	0.3	150– 200	10^6 (5×10^5)	1.43
SI-InP	50–100.0	$\approx 1\,000$	4×10^7	1.34
Ion-Implanted InP	2– 4.0	200	$> 10^6$	1.34
RD-SOS	0.6	30		1.10
Amorphous Si	0.8– 20.0	1	10^7	1.10
MOCVD CdTe	0.5	180		1.49
LT-In$_{0.52}$Al$_{0.48}$As	0.4	5		1.45
Ion-implanted Ge	0.6	100		0.66

Table 4-1 Characteristics of photoconductive substrates.[6]

Line shown in Ref. [11] (THz)	Line shown in Ref. [12] (THz)	Line measured in this thesis (THz)
0.557	0.553	0.560
0.752	0.747	0.749
0.988	0.980	0.991
1.097	1.090	1.105
1.113	1.109	
1.163	1.158	1.158
1.208	1.200	1.211
1.229	1.223	1.234
1.410	1.406	1.415
	1.596	1.604
		1.673
		1.718
		1.763
		1.801
		1.869
		1.922

Table 4-2 Water vapor absorption lines in THz region. The data shown in the left column are from Reference [11]. The data shown in the middle column are from Reference [12]. The data shown in the right column are read out from Figure 4-9.

Figures
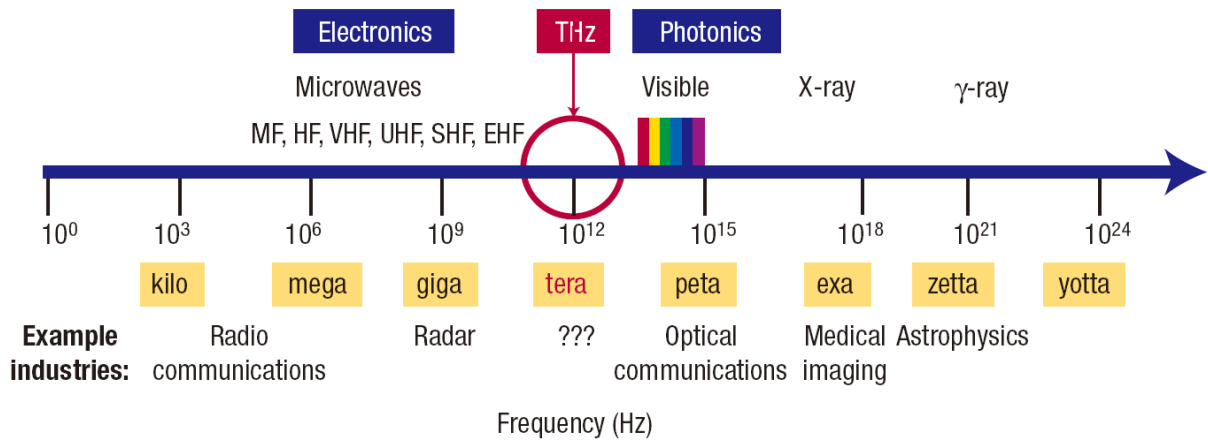
Figure 4-1 Spectrum of electromagnetic wave.
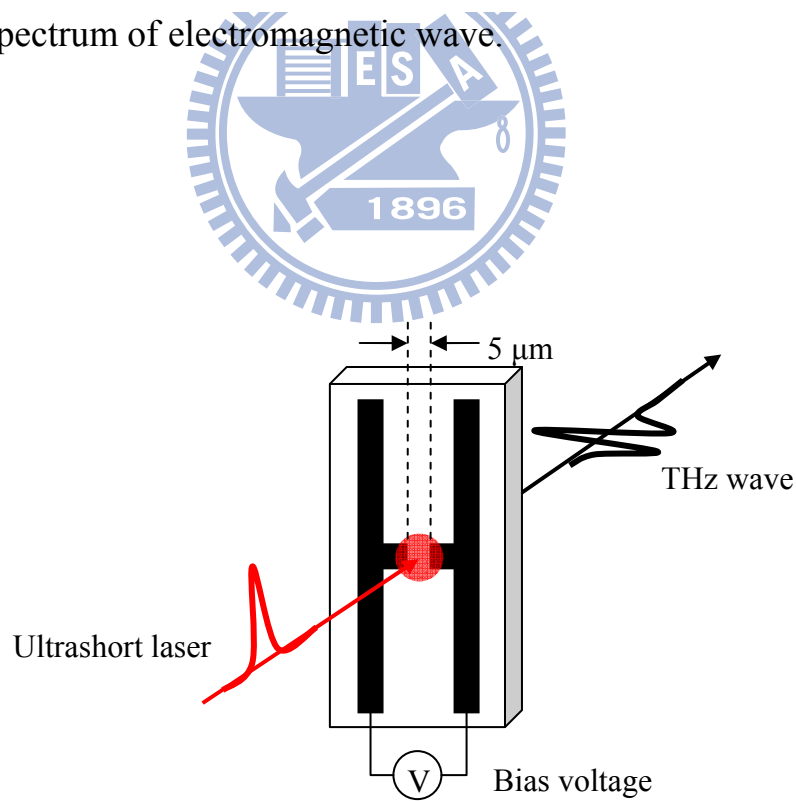
Figure 4-2 Structure of the photoconductive dipole antenna.
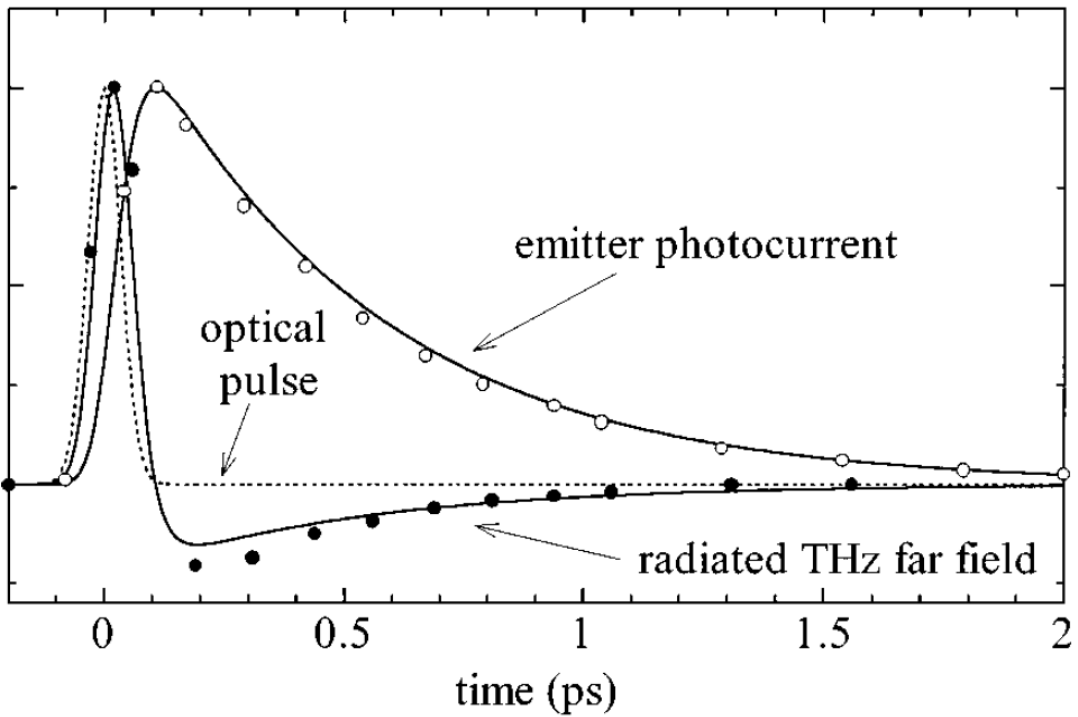
Figure 4-3 The calculated photocurrent in the emitting photoconductive antenna and the amplitude of the THz field versus time. The temporal pulse shape of the ultrashort pulse is shown as a dotted line.[9]
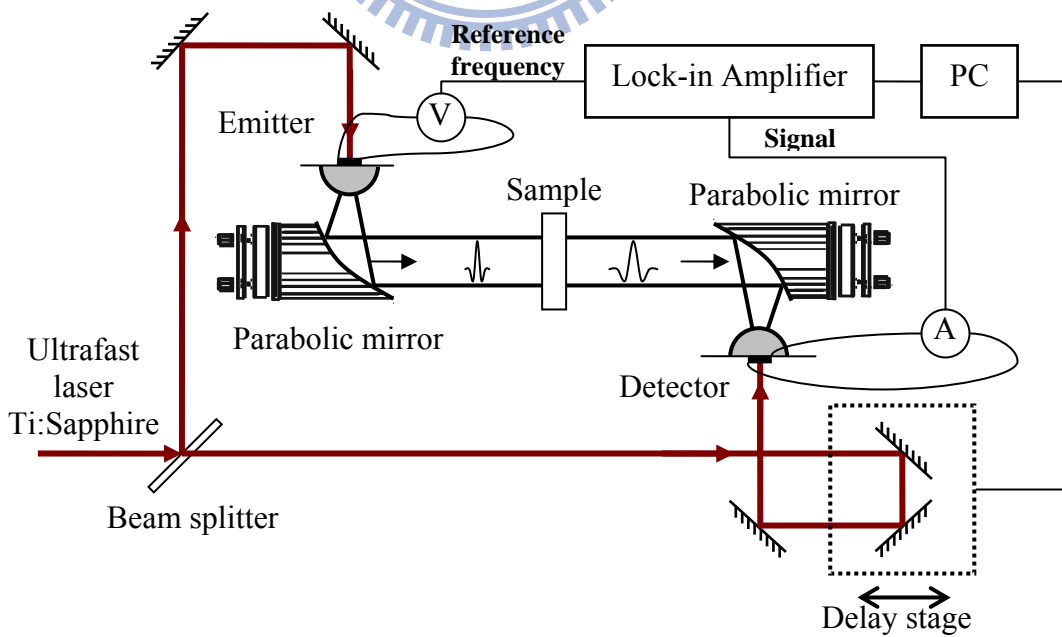
Figure 4-4 Scheme of the terahertz time-domain spectroscopy system.
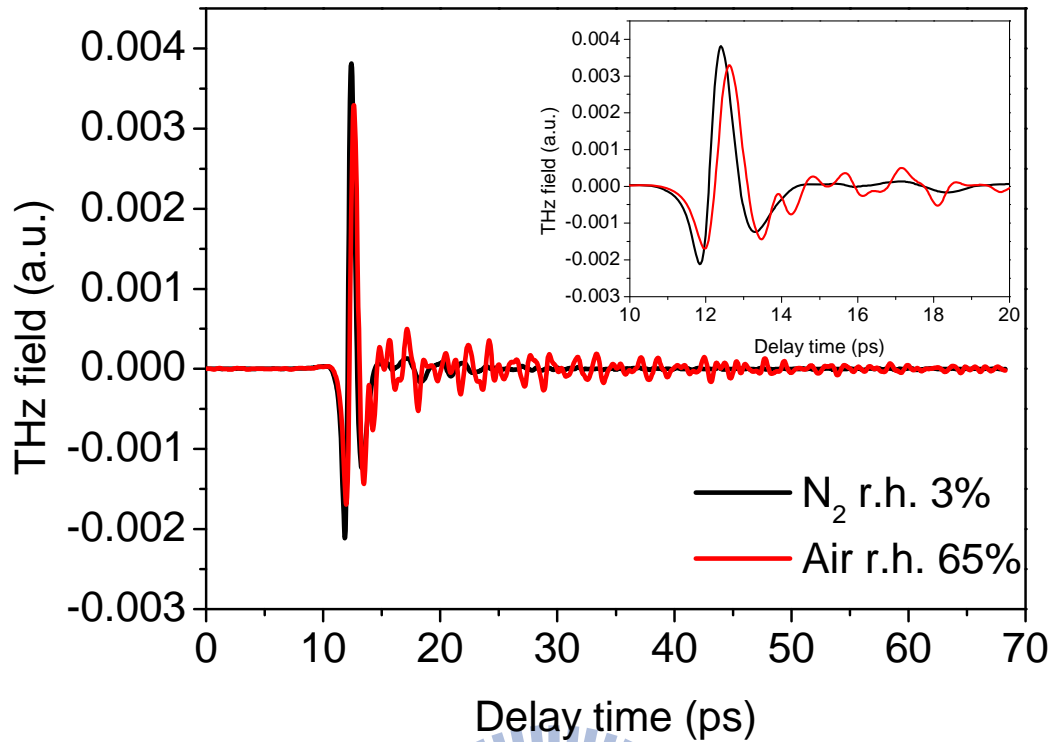
Figure 4-5 THz field signal measured by using THz-TDS system. The red line is the atmosphere signal (r.h.~65%). The black line is the atmosphere signal with N_2 purged (r.h.~3%).
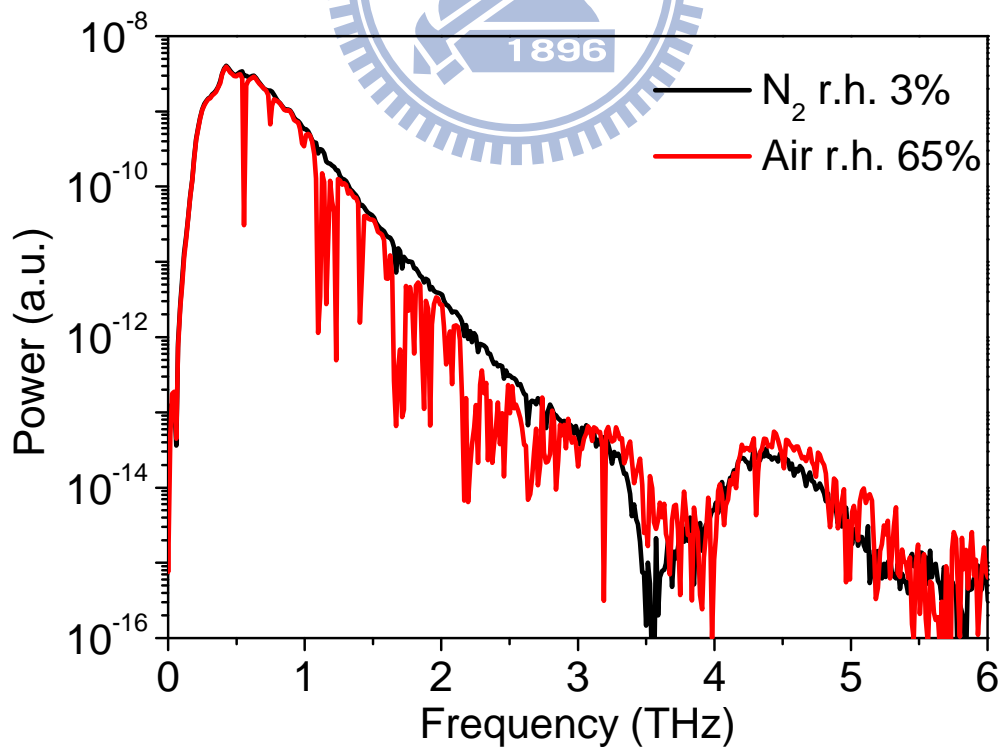
Figure 4-6 Power spectrum of the THz signal in frequency domain. The red line is the atmosphere signal (r.h.~65%). The black line is the atmosphere signal with N_2 purged (r.h.~3%).
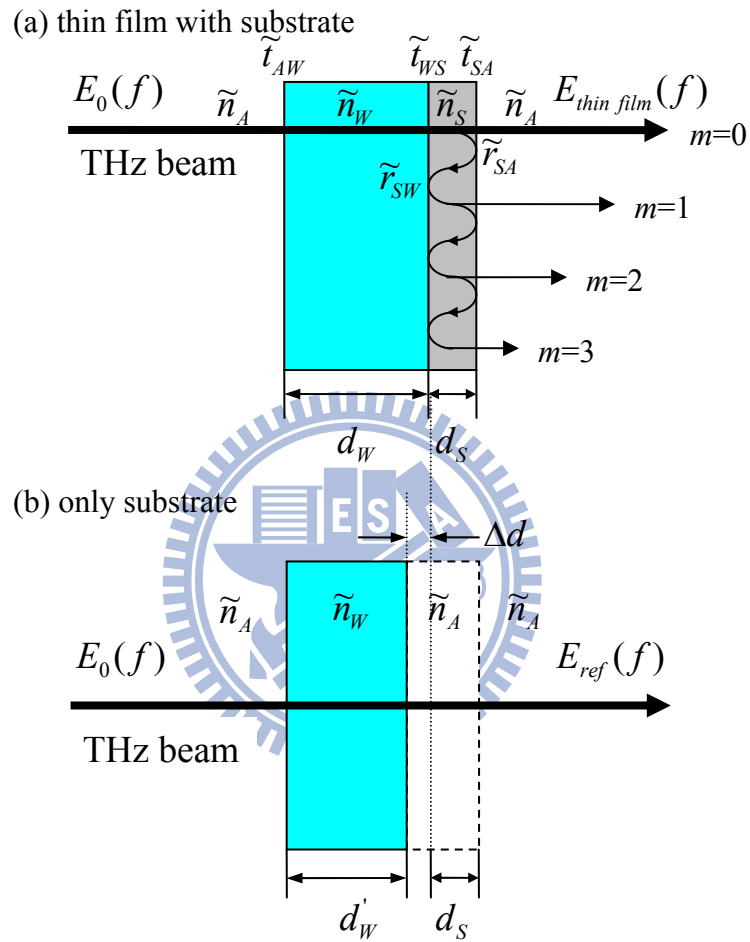
Figure 4-7 Scheme of the THz wave pathway near the sample. (a) the THz wave pass through a sample thin film with substrate. (b) the THz wave pass through only substrate.

(a) cell with two substrates

$\tilde{t}_{AW}$ $\tilde{t}_{WS}$ $\tilde{t}_{SW}$ $\tilde{t}_{WA}$

$E_0(f)$ $\tilde{n}_A$ $\tilde{n}_W$ $\tilde{n}_S$ $\tilde{n}_W$ $\tilde{n}_A$ $E_{LC}(f)$ $m=0$

THz beam

$\tilde{r}_{SW}$ $\tilde{r}_{SW}$ $m=1$

$m=2$

$m=3$

d_{W1} d_S d_{W2} $d_W = d_{W1} + d_{W2}$

(b) only two substrates

Δd

$\tilde{n}_A$ $\tilde{n}_W$ $\tilde{n}_W$ $\tilde{n}_A$

$E_0(f)$ $E_{ref}(f)$

THz beam

d_{W3} d_{W4} d_S $d_W' = d_{W3} + d_{W4}$
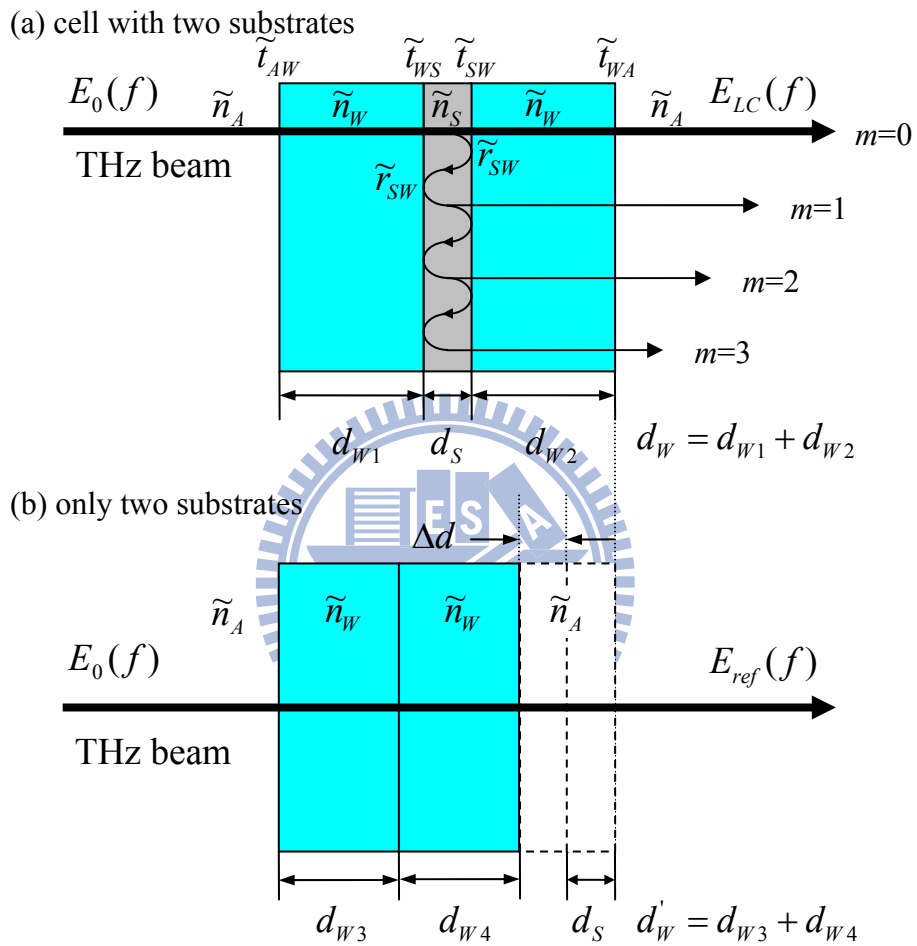
Figure 4-8 Scheme of the THz wave pathway near the sample. (a) the THz wave pass through a cell with two substrates. (b) the THz wave pass through only two substrates.
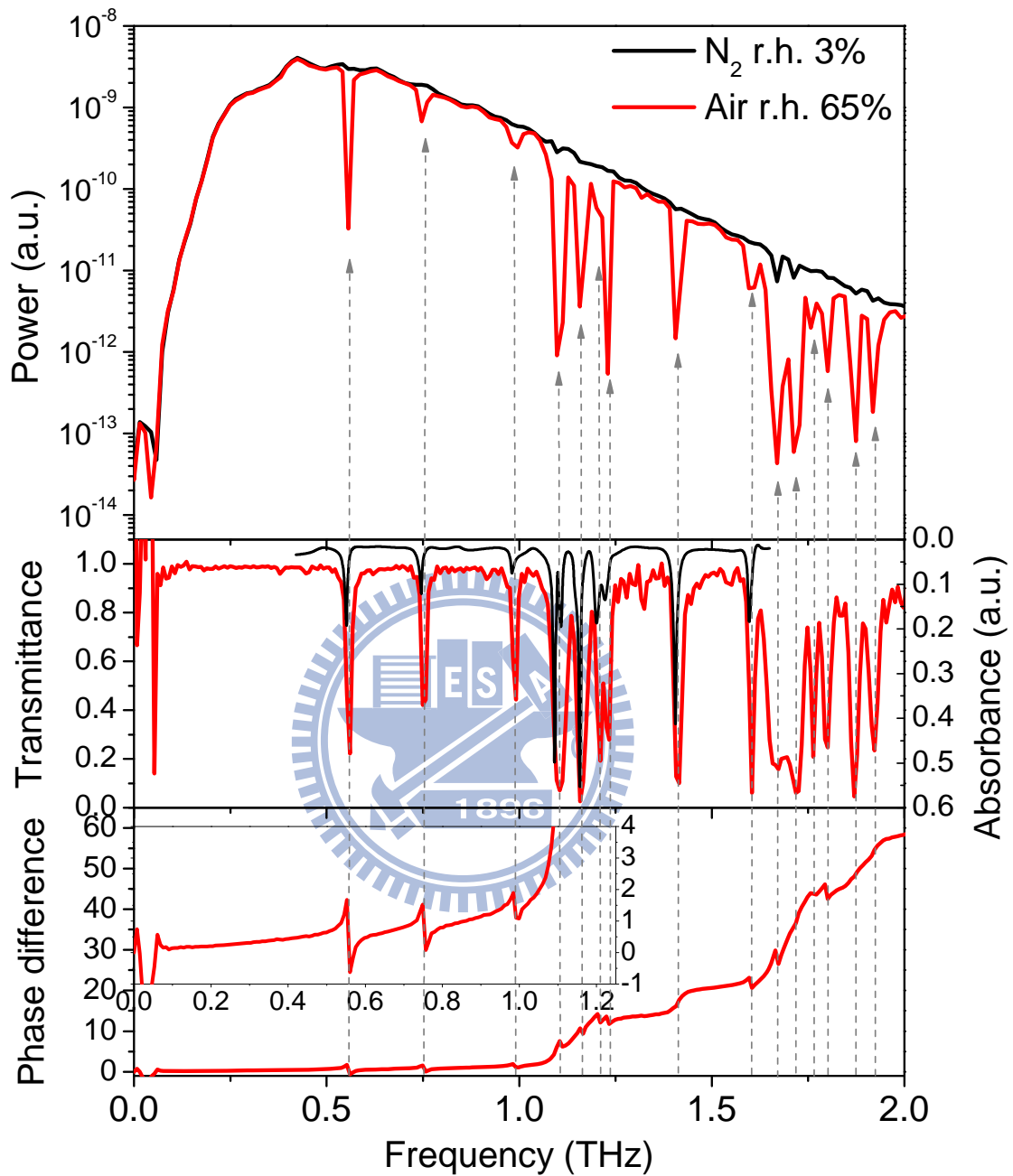
Figure 4-9 Spectrum of the water vapor absorption peak in THz region. The upper graph is the power spectrum (black line: r.h.~3%, red line: r.h.~65%). The middle and lower graph is the transmittance and the phase difference by using the N₂ purged spectrum as a reference, respectively. The black line in the middle graph is the water vapor absorbance spectrum in Ref. [12].
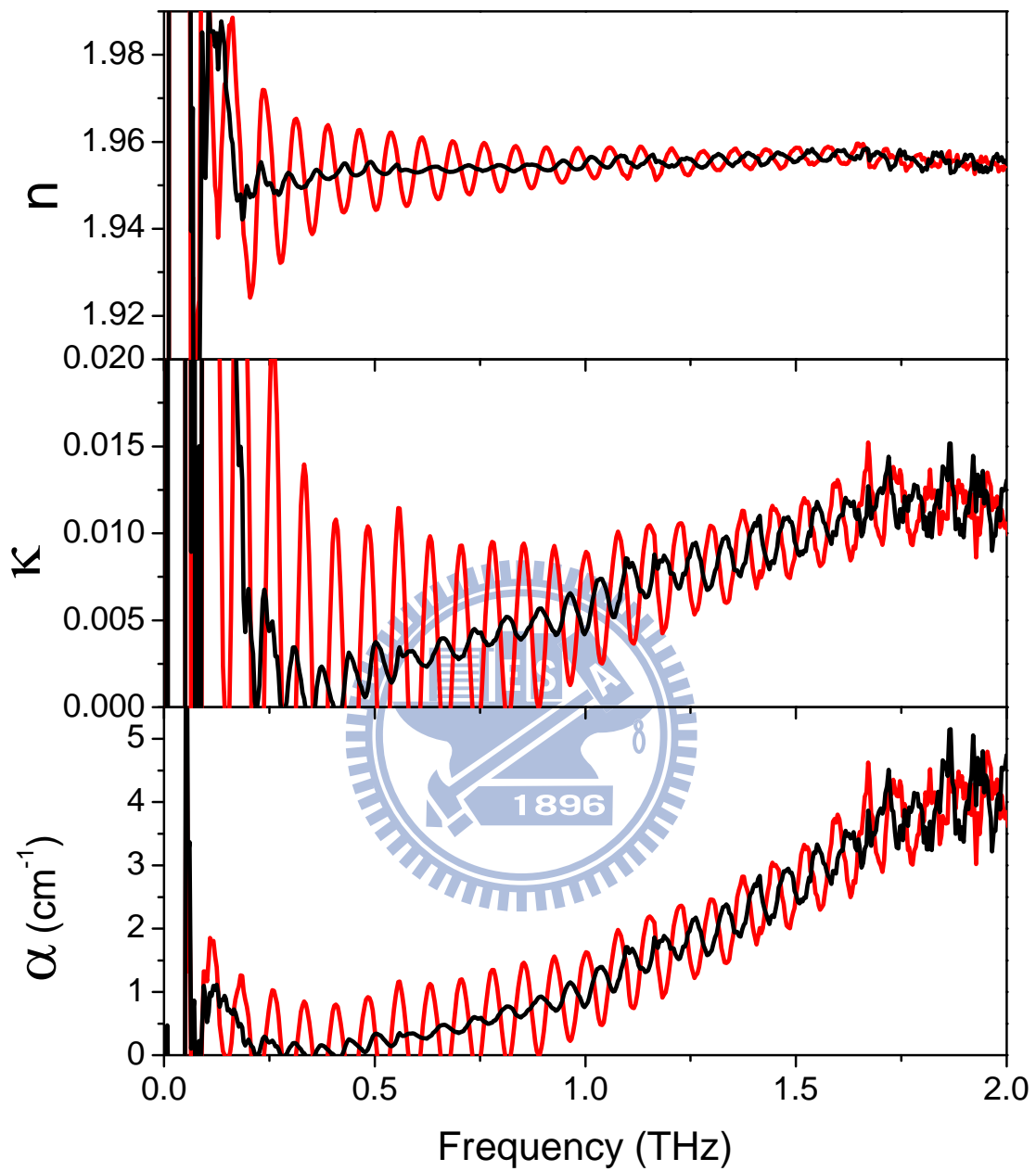
Figure 4-10 Optical constants of 1 mm fused silica substrate. The red line is the spectrum without considering the multiple reflections. The black line is the spectrum with considering the multiple reflections.
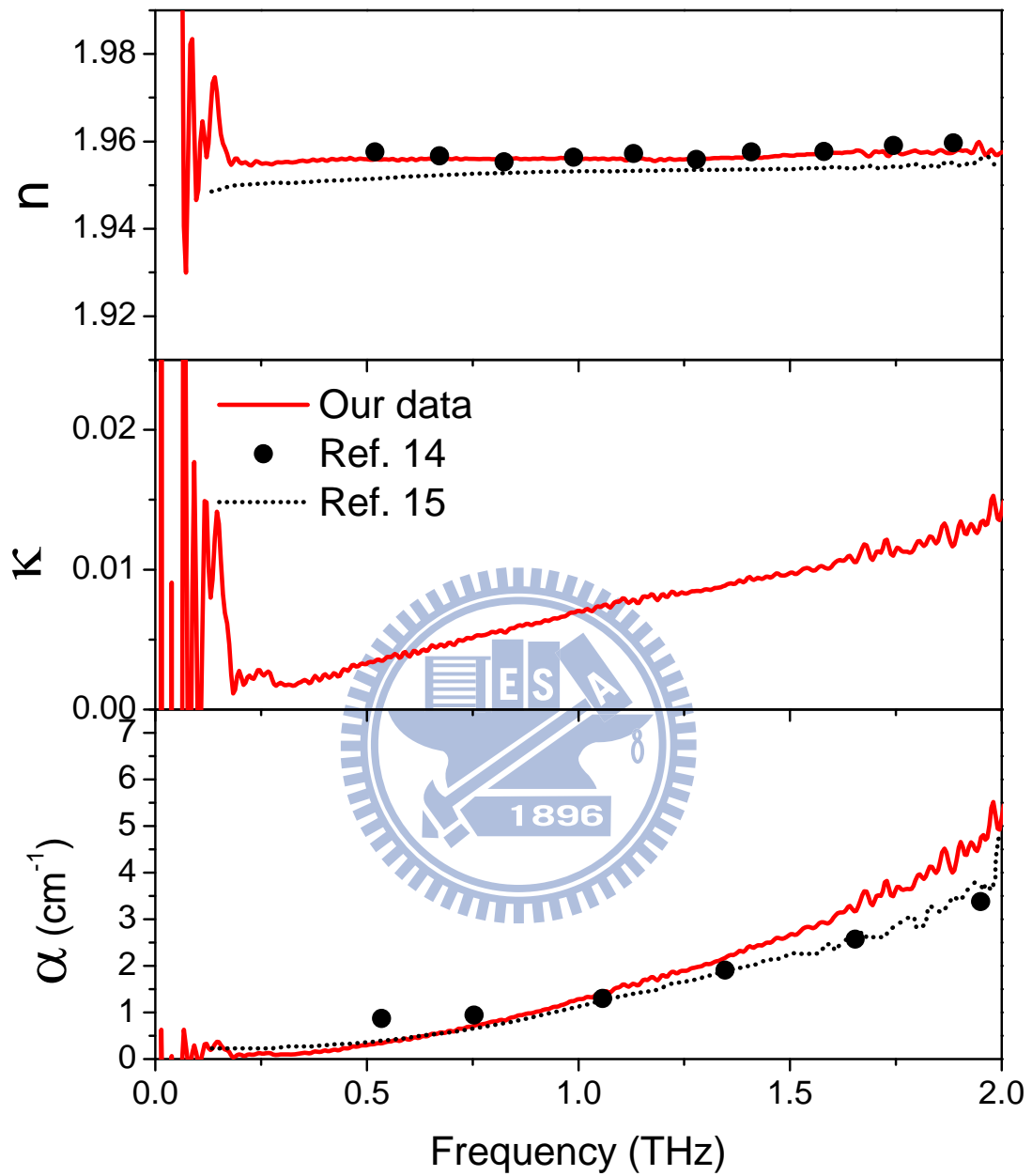
Figure 4-11 Optical constants of 3 mm fused silica substrate in THz region. The solid circles are the data in Ref. [13]. The dashed line is the date in Ref. [14].
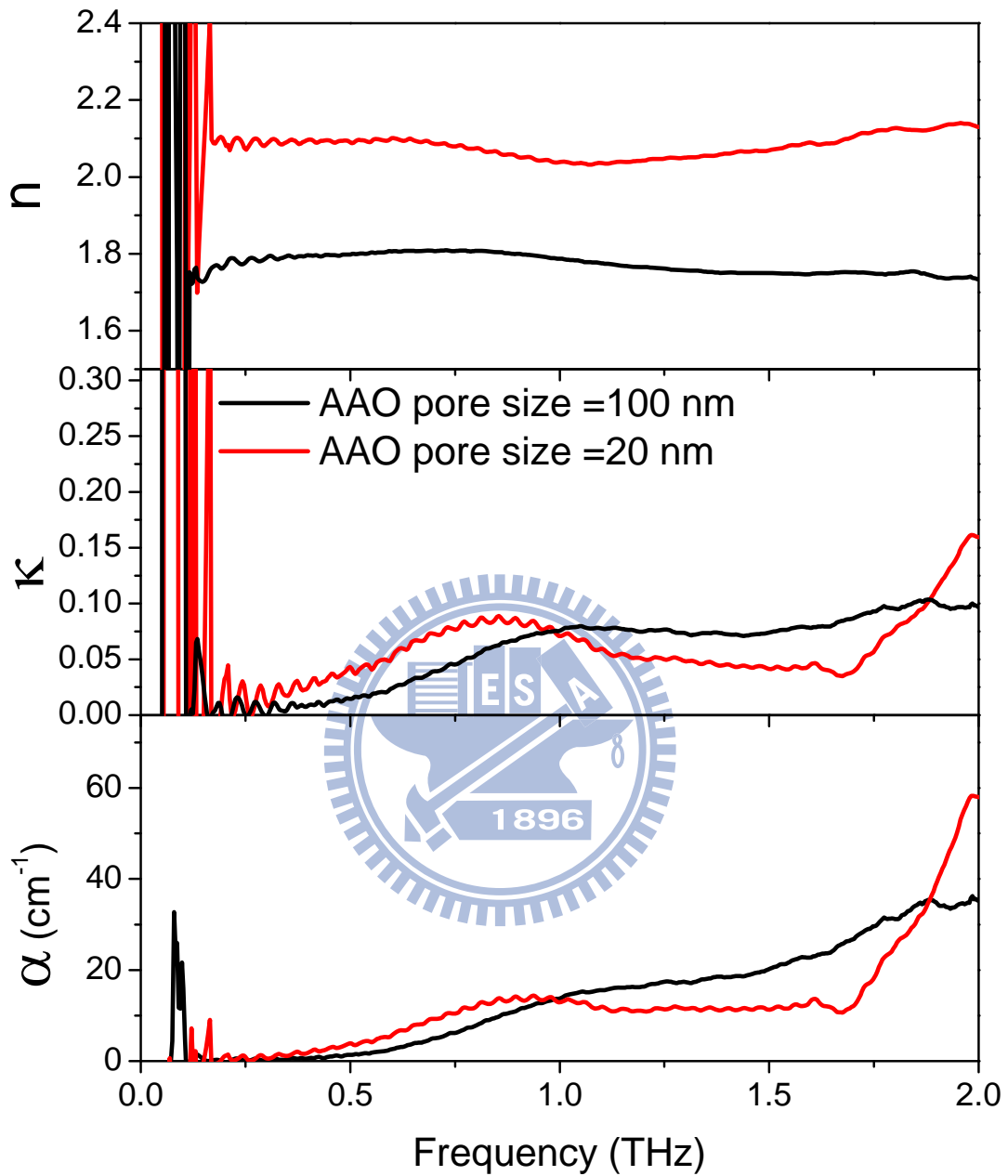
Figure 4-12 Optical constants of the commercial AAO substrate. The black line is the spectrum of the AAO substrate with 100 nm pores. The red line is the spectrum of the AAO substrate with 20 nm pores.
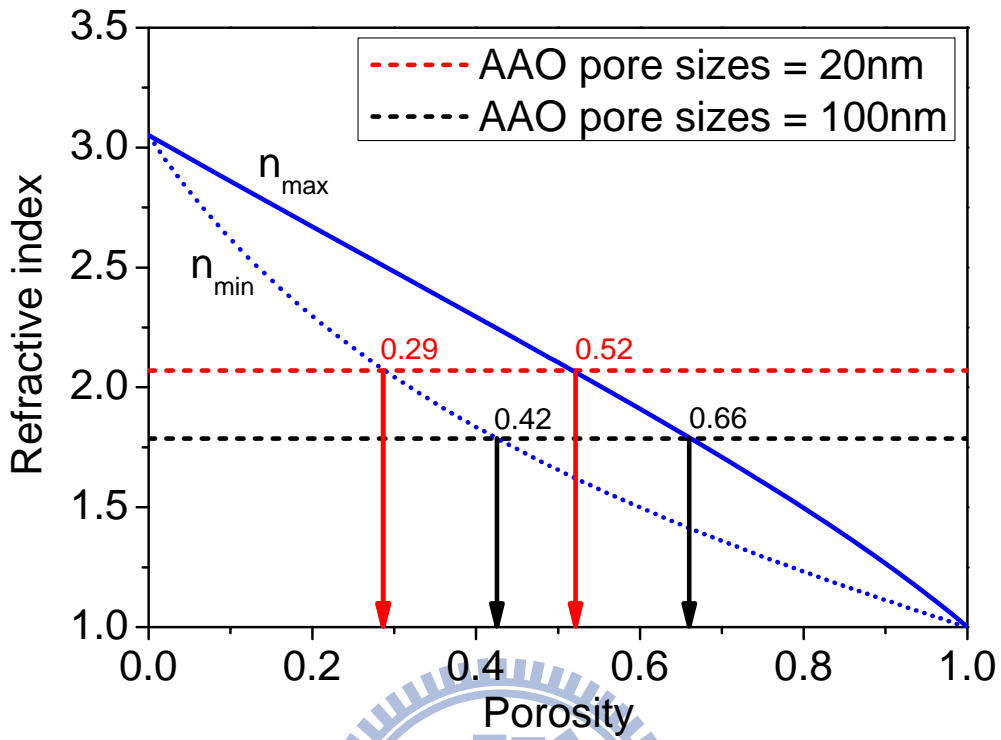
Figure 4-13 Relationship between the refractive index and the porosity.
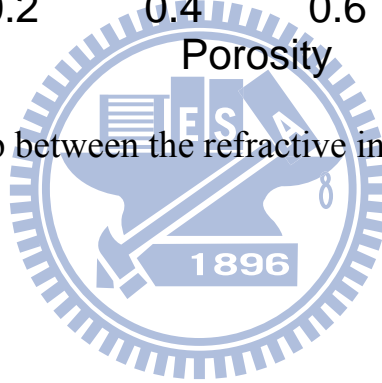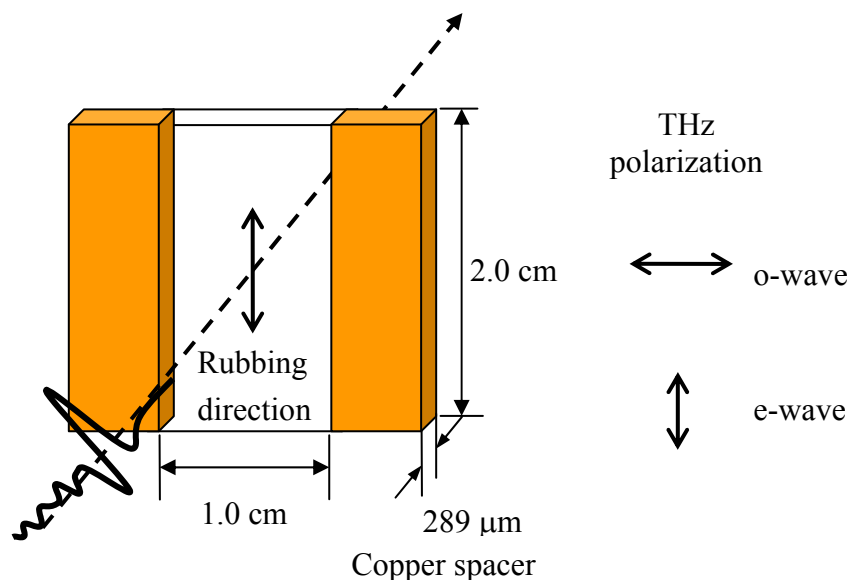
Figure 4-14 Configuration of the FLC cell and its geometry with respect to the incident terahertz wave
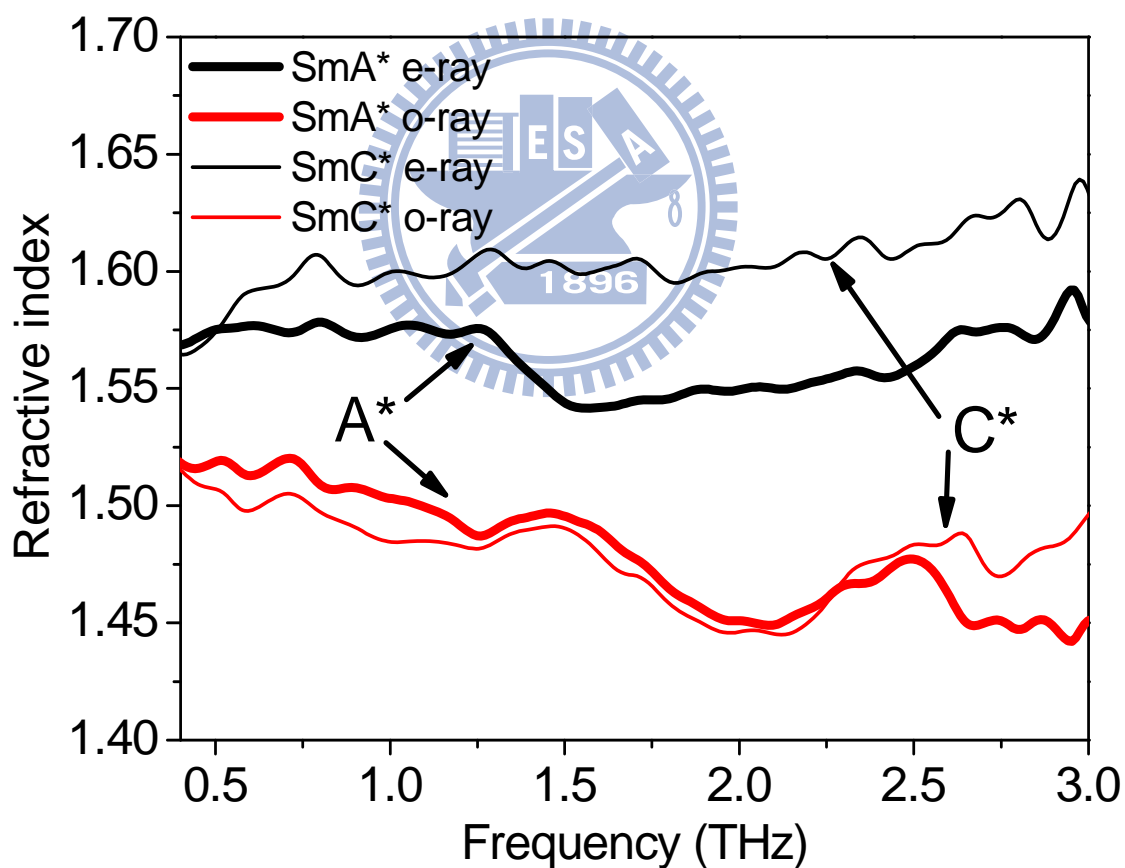
Figure 4-15 The THz-band real extraordinary and ordinary indices of refraction of the FLC in the SmA* phase (67.9 °C) and SmC* phase (58.1°C).
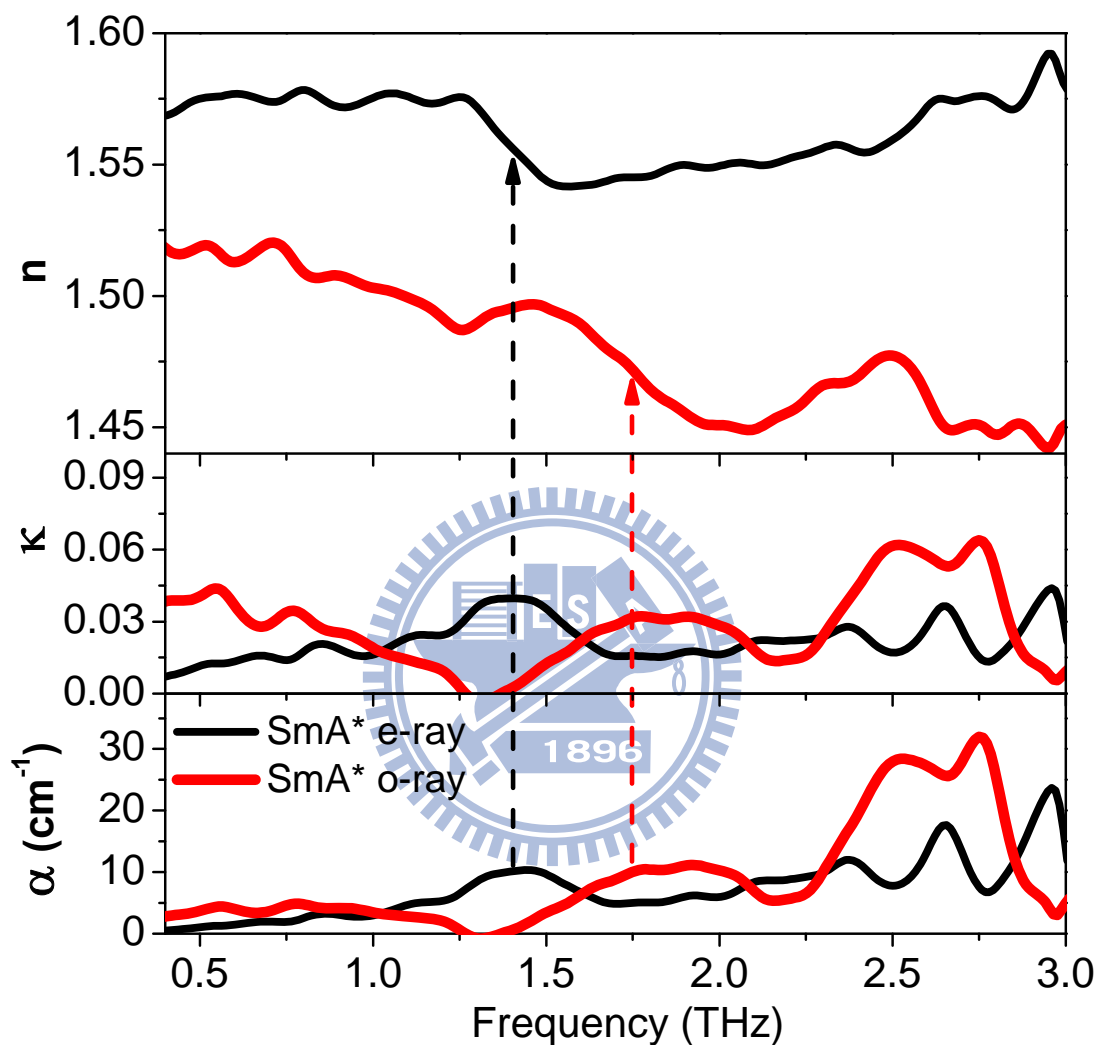
Figure 4-16 Frequency dependence of the THz-band extraordinary and ordinary absorption coefficients of the FLC in the SmA* phase (67.9°C). To compare, both real and imaginary indices of refraction are also shown. The dashed lines indicate possible positions of the absorption bands.
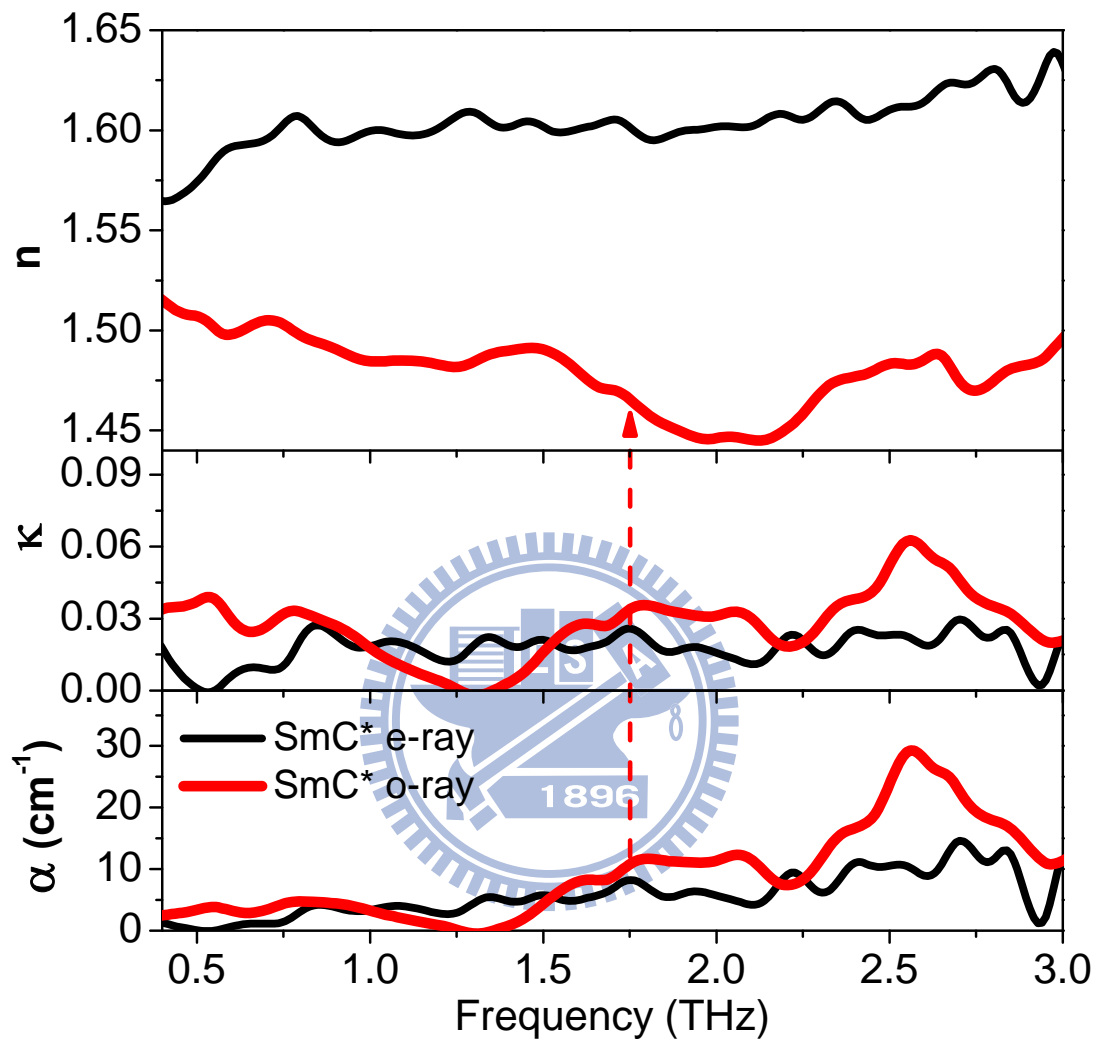
Figure 4-17 Frequency dependence of the THz-band extraordinary and ordinary absorption coefficients of the FLC in the SmC* phase (58.1°C). To compare, both real and imaginary indices of refraction are also shown. The dashed line indicates possible position of the absorption band.

Chapter 5
Homogenous alignment
on the grooved PDMS substrate fabricated
by the nanoimprinting technology

5.1 Overview

According to the preliminary studies in our group, the U-shaped microgrooves can align the liquid crystal molecules homogenously.[1] However, there are some drawbacks about this alignment method. The U-shaped microgrooves are manufactured by using the photolithography technology and the reactive ion etching (RIE) technology. The minimum period of the microgroove is limited by the optical limitation of the photolithography technology. By using the RIE technology, every substrate needs to apply one etching process. It is difficult to manufacture a lot of microgroove substrates by the traditional method.

Recently, the nanoimprinting technology is developed dramatically for manufacturing the components with the structure size in micrometer or nanometer. Because the size of the microgrooves that can align the liquid crystal molecules is around 1~5 μm, it is easy to manufacture by using the nanoimprinting technology.

5.2 Polydimethylsiloxane (PDMS)

Polydimethylsiloxane (PDMS) is the most widely used silicon-based organic polymer. Its applications range from contact lenses and medical devices to elastomers. PDMS is optically clear, and is generally considered to be inert, non-toxic and non-flammable. The chemical formula and the chemical structure are shown in Figure 5-1. The chemical formula for PDMS is $(H_3C)_3$-SiO-$[Si(CH_3)_2O]$n-$Si(CH_3)_3$, where n is the number of repeating monomer

[SiO(CH$_3$)$_2$] units.

PDMS molecules have quite flexible polymer backbones due to their siloxane linkages. Such flexible chains become loosely entangled when molecular weight is high, which results in PDMS having an unusually high level of viscoelasticity. After polymerization and cross-linking, the solid PDMS samples will present an external hydrophobic surface.[2] Because of the property of hydrophobic surface, the polar solvents, such as water, are difficult to wet the PDMS surface. But these hydrophobic surfaces are easier to adsorb the contaminants with hydrophobic property. The O$_2$ plasma treatment can be used to modify the surface property by adding silanol (SiOH) groups to the PDMS surface.[3] The modified PDMS surfaces are hydrophilic and allow water to wet. For the water-based micro-fluidics applications, the O$_2$ plasma treatment is required. The hydrophilic property of the oxidized PDMS surfaces can remain around 30 minutes in air. Even if the oxidized PDMS substrates are stored in vacuum, air or water, the recovery of hydrophobic property is unavoidable.[4] The PDMS substrate is an excellent candidate for optical applications. It is because the PDMS substrate is almost transparent in visible region.

In this thesis, the PDMS kit we used is Sylgard® 184 Silicone Elastomer Kit from DOW CORNING Inc. The Sylgard® 184 kit are supplied as two-part liquid component kits comprised of one bottle of base (Part A) and one bottle of curing agent (Part B). The best mix ratio of base and curing agent is 10:1 by weight or volume. When these two liquid components are totally mixed, the mixture is a viscoid liquid which is good for the nanoimprinting application. According to the datasheet from Dow Corning Inc., the curing time depend on the curing temperature. For heat curing, it takes 10 minutes at 150 °C, 20 minutes at 125 °C, or 45 minutes at 100 °C. If the curing process is done in room temperature, it needs to take more than 24 hours. After the curing process, the PDMS becomes a flexible elastomer, which is suited for the flexible applications.

5.3 Nanoimprinting technology [5]-[8]

In 1995, the nanoimprinting technology is developed by the NanoStructure laboratory in Minnesota University. Stephen Y. Chou et al. demonstrated the nanoimprint lithography which is based on a principle fundamentally different from that for conventional lithographies.[5] The nanoimprint lithography creates the pattern on the photoresist by deforming the physical shape of the resist with embossing, rather than by modifying the resist chemical structure with radiation, such as UV radiation and electron beam. The nanoimprint lithography is capable of producing sub-10 nm features over a large area with a high throughput and low cost. Stephen Y. Chou et al. have achieved 25 nm features size and 100 nm pitch and excellent uniformity over an area of 16 mm by 18 mm. In 1996, J. Haisma et al. develop the UV nanoimprint lithography technology which is imprinting the nanostructure on the photosensitive resist. Then, the imprinted nanostructure can be cured by irradiating the UV light. Figure 5-2 shows the schematic process of the thermo-imprinting technology and the UV-imprinting technology. The differences between thermo- and UV-imprinting technologies are the polymer and the curing method. In Figure 5-2, the first step is spin-coating the thermo or UV curable polymer and aligning the mold to the substrate. Second step is mechanical structuring followed by thermo-cured or UV-induced solidification. Then, the third step is removal of the mold carefully. Finally, the resulting surface is a patterned layer on substrate.

In this work, we use the nanoimprinting technology to manufacture the U-shape grooved substrate on the flexible PDMS substrate. By using the imprinted PDMS substrate as the alignment substrate, the preliminary alignment characteristic has been investigated.

5.4 Results and discussions

5.4.1 Morphology of the imprinted PDMS substrate

The morphology of the imprinted PDMS substrate has been investigated by Atomic Force Microscopy (AFM). In the nanoimprinting technology, the mold can be used several times. But the groove on the mold could be filled by the residual PDMS after each imprinting process. Figure 5-3 shows the AFM analysis report of the imprinted PDMS substrate with 5 μm groove. Figure 5-3 (a) shows the first imprinted PDMS substrate and (b) shows the second imprinted PDMS substrate. According to the AFM report, the groove structure with 5 μm period could be transferred perfectly. Both the first and the second imprinted PDMS substrate show the perfect transferred groove structure. Therefore, the nanoimprinting technology can be used to manufacture the microgroove structure on the PDMS substrate.

5.4.2 Contact angles of the imprinted PDMS substrate

According to the PDMS properties, PDMS is a highly hydrophobic material. The contact angle on the flat PDMS surface is usually 90°~120° for water. In order to investigate the surface properties on the patterned PDMS surface, the water contact angle is measured. Table 5-1 shows the water contact angle on the grooved PDMS surface before O_2 plasma treatment. Regardless of the period of the groove, the water contact angle on the PDMS surface is between 102° and 113°. The contact angle measured perpendicular to the groove is smaller than that measured parallel to the groove. It shows the water will tend to flow along the groove. Because the PDMS surface is highly hydrophobic, water and liquid crystal are difficult to attach on the surface. By using the O_2 plasma treatment, the PDMS substrate property can be modified and become hydrophilic. [4]

Table 5-2 shows the water contact angle on the grooved PDMS substrate after O_2 plasma treatment. The water contact angles are much smaller than those before O_2 plasma treatment. That means the PDMS surface has been modified as the hydrophilic surface. After O_2 plasma treatment, the same behavior is shown. The contact angle measured perpendicular to the groove is smaller than that

measured parallel to the groove for each period. The shorter period has the larger water contact angle. It is understandable that water is difficult to fill into the smaller groove because of the surface tension of water. Hydrophilic surface indicates the surface with smaller contact angle and higher surface energy. The liquid crystal molecules on the hydrophilic surface tend to align at in-plane direction. Therefore, liquid crystal and water will be easier to attach on the PDMS surface with O_2 plasma treatment. All of the PDMS substrates are treated by O_2 plasma before constructing the liquid crystal cells.

5.4.3 Alignment characterization of the imprinted PDMS substrate

By using the grooved PDMS substrate with O_2 plasma treatment, the liquid crystal cell can be constructed and observed in a pair of polarizers. The cell gap of the liquid crystal cell is 23 μm. The liquid crystal filled into the cell at isotropic state (T > 36°C) is 5CB (from Merck co.). Figure 5-4 shows the polarizing image of the liquid crystal cell with the O_2 plasma treated PDMS substrate. The power of O_2 plasma are 70 W and 114 W. The treating time are between 0.1 min. and 1.1 min.. The micrographs are taken in two orientations of the cell, 45° with respect to each other. Considering the same power and treating time, the liquid crystal cell with smaller period groove has higher contrast. If we make the power of O_2 plasma to be constant, the cell with longer treating time has higher contrast. The higher contrast means the liquid crystal molecules align more uniformly.

5.5 Summaries

In this chapter, we have demonstrated the liquid crystal alignment on the flexible PDMS substrate with microgroove structure and O_2 plasma treatment. For this alignment method, there are some advantages and disadvantages. The PDMS substrate is an excellent flexible and transparent substrate. It is easy to

manufacture the alignment structure by using the nanoimprinting technology. The imprinted PDMS surface can be easily modified by O_2 plasma with different power and treating time. The modified PDMS surface with micro groove can align the liquid crystal molecules homogenously. The liquid crystal cell with short period groove has better contrast and the PDMS surface with short period groove has higher alignment ability. There are some drawbacks about this alignment method. Because of the hydrophobic property of the PDMS material, the PDMS surface is difficult to attach each other. Therefore, it is hard to seal off the liquid crystal cell by the thermo- or UV-curing glue. For larger liquid crystal cell, the PDMS substrate is flexible resulting in the cell gap of the cell is difficult to control. The substrate of the cell in the center area is without the spacer and is deformed by gravity. Otherwise, the imprinted PDMS substrate is a good alignment substrate for the flexible liquid crystal display applications.

References

[1] Y. F. Lin, M. C. Tsou, and R. P. Pan, "Alignment of liquid crystals by ion etched grooved glass surfaces," *Chinese J. Phys.* **43**, 1066 (2005).

[2] J. C. McDonald, D. C. Duffy, J. R. Anderson, D. T. Chiu, H. Wu, O. J. A. Schueller, and G. M. Whitesides, "Fabrication of microfluidic systems in poly(dimethylsiloxane)," *Electrophoresis* **21**, 27 (2000).

[3] S. Bhattacharya, A. Datta, J. M. Berg, and S. Gangopadhyay, "Studies on surface wettability of poly(dimethyl)siloxane (PDMS) and glass under oxygen-plasma treatment and correlation with bond strength," *Journal of Microelectromechanical systems* **14**, 590 (2005).

[4] H. Hillborg, J. F. Ankner, U. W. Gedde, G. D. Smith, H. K. Yasuda, and K. Wikstrom, "Crosslinked polydimethylsiloxane exposed to oxygen plasma studied by neutron reflectometry and other surface specific techniques," *Polymer* **41**, 6851 (2000).

[5] S. Y Chou, P. R. Krauss, and P. J. Renstrom, "Imprint of sub-25 nm vias and trenches in polymers," *Appl. Phys. Lett.* **67**, 3114 (1995).

[6] S. Y Chou, P. R. Krauss, and P. J. Renstrom, "Imprint lithography with 25-nanometer resolution," *Science* **272**, 85 (1996).

[7] S. Y Chou, P. R. Krauss, and P. J. Renstrom, "Nanoimprint lithography," *J. Vac. Sci. Technol. B* **14**, 4129 (1996).

[8] S. Y. Chou, P. R. Krauss, W. Zhang, L. Guo, and L. Zhuang, "Sub-10 nm imprint lithography and applications," *J. Vac. Sci. Technol. B* **15**, 2897 (1997).

[9] J. Haisma, M. Verheijen, K. van den Heuvel, and J. van den Berg, "Mold-assisted nanolithography: A process for reliable pattern replication," *J. Vac. Sci. Technol. B* **14**, 4124 (1996).

Tables

before O₂ plasma treatment		
	water contact angle observed parallel to groove(deg.)	water contact angle observed perpendicular to groove(deg.)
no groove	105.60	
2u	112.52	103.29
3u	107.98	102.08
4u	110.26	106.98
5u	108.11	102.81

Table 5-1 Contact angles of water on the grooved PDMS substrate before O_2 plasma treatment.

after O₂ plasma treatment		
	water contact angle observed parallel to groove(deg.)	water contact angle observed perpendicular to groove(deg.)
2u	36.52	29.91
3u	16.88	14.68
4u	14.76	10.24
5u	6.96	5.84

Table 5-2 Contact angles of water on the grooved PDMS substrate after O_2 plasma treatment.

Figures
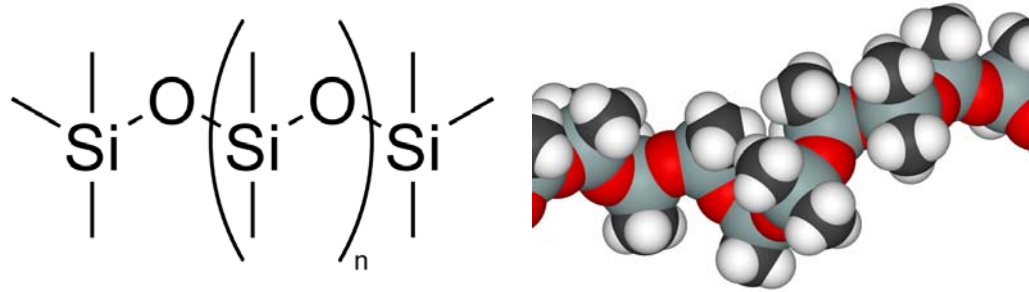
Figure 5-1 Chemical formula and the chemical structure of PDMS (from wiki).
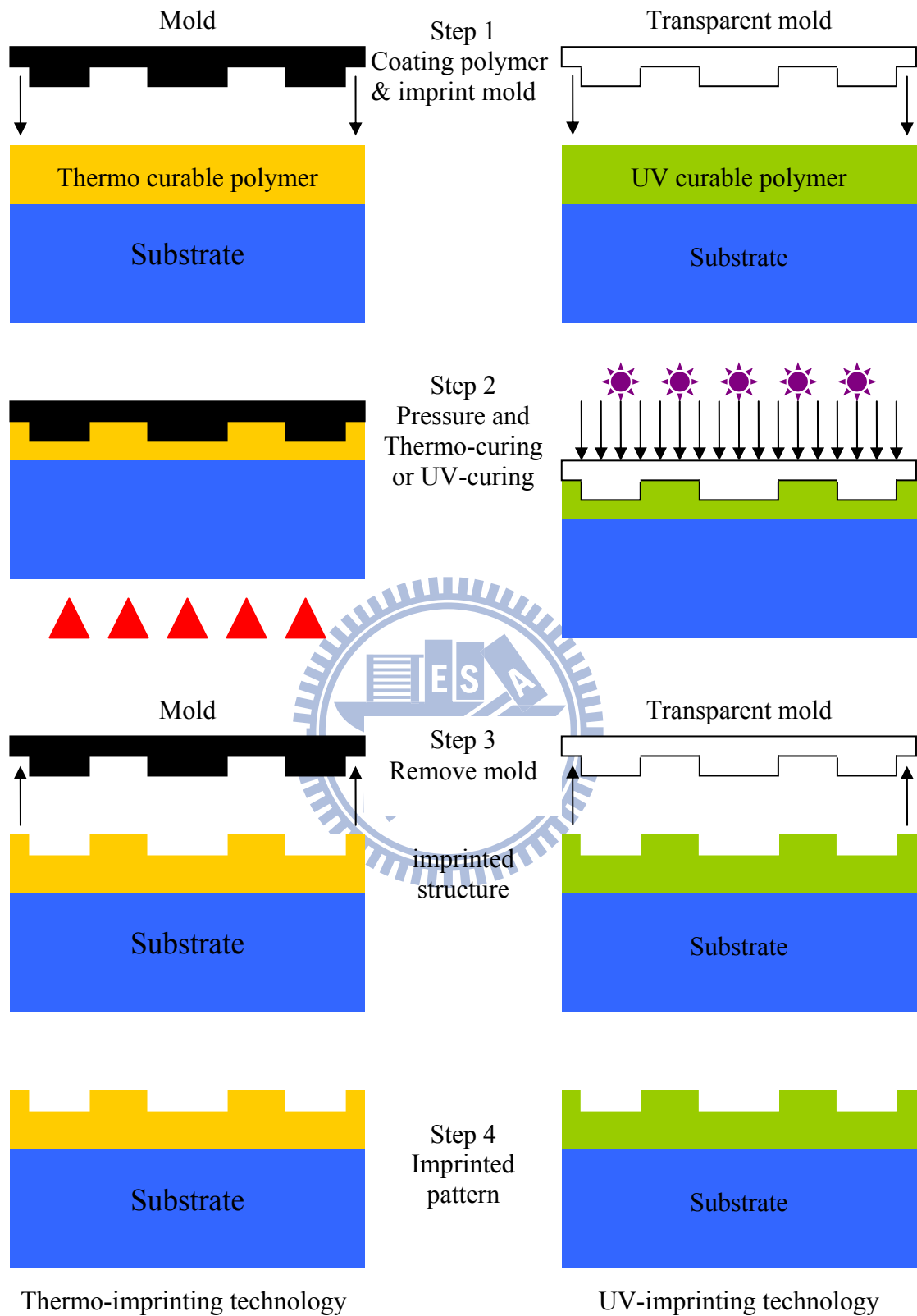
Figure 5-2 Schematic process of the thermo-imprinting technology and the UV-imprinting technology.

(a)
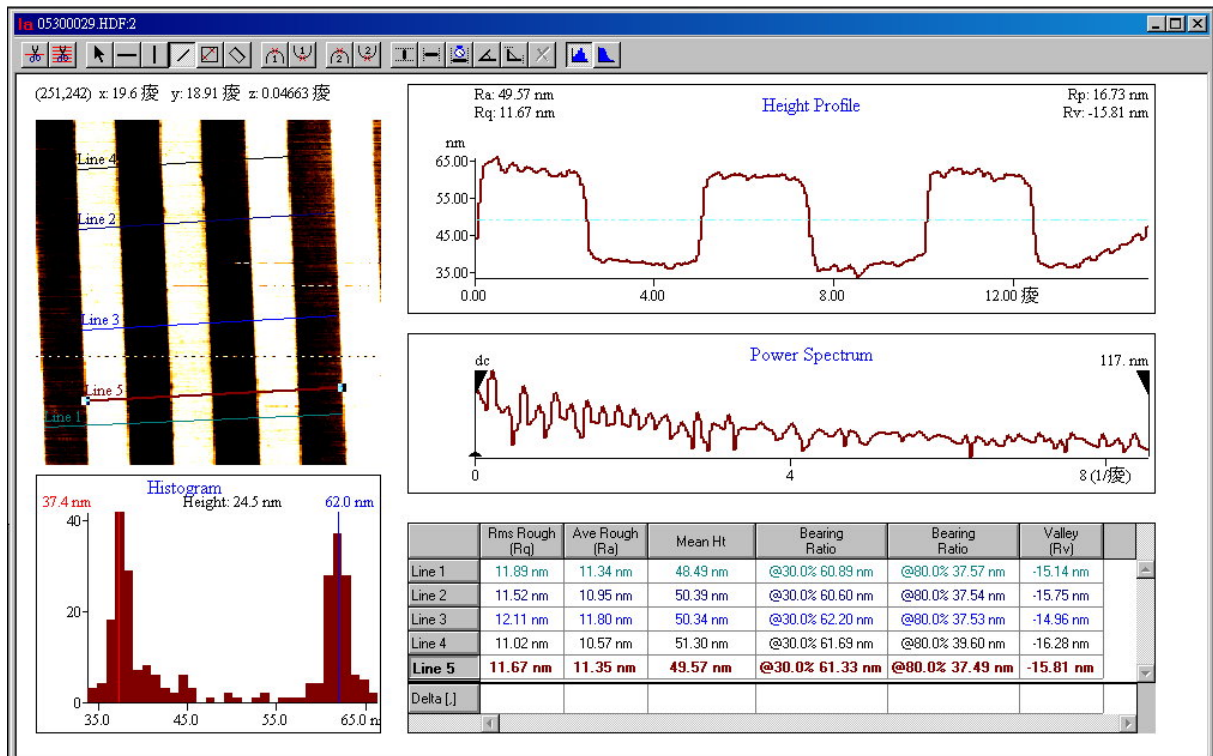
(b)
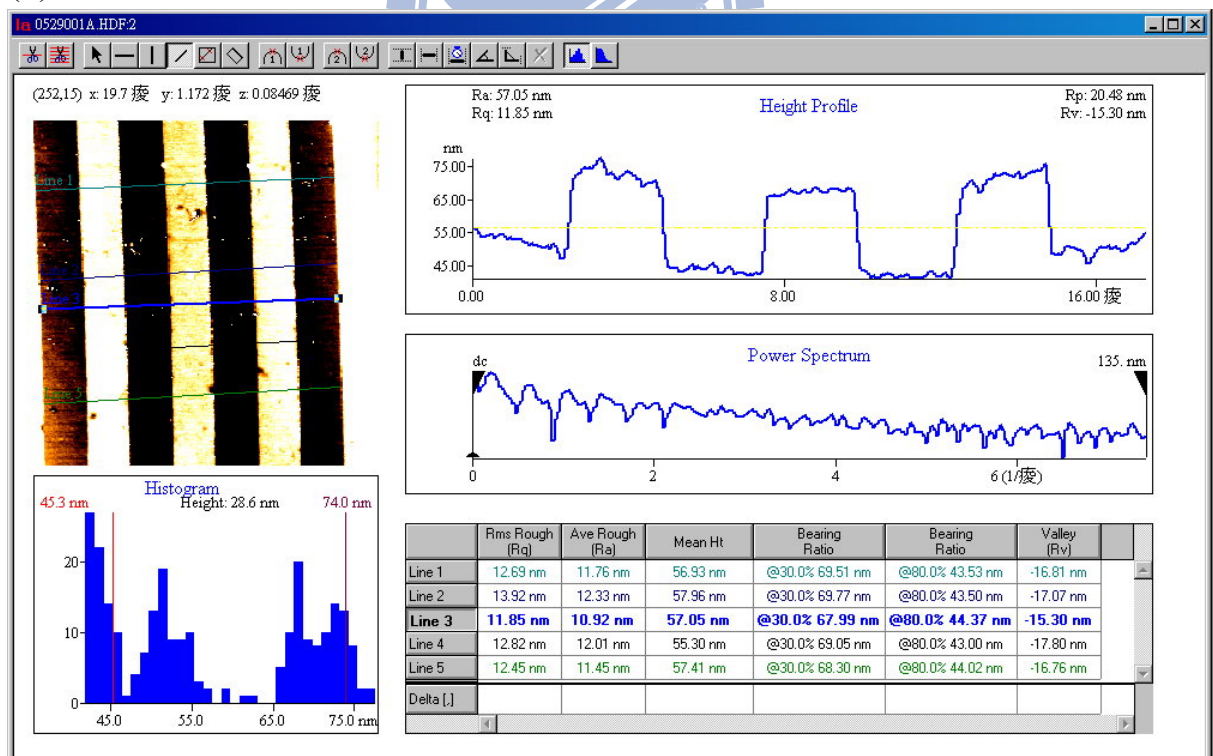
Figure 5-3 AFM report of the imprinted PDMS substrate with 5 μm groove. (a) the first imprinted groove PDMS substrate, (b) the second imprinted groove PDMS substrate.

	0.1 min @ 0°	0.1 min @ 45°	0.3 min @ 0°	0.3 min @ 45°
70W 2μ				
70W 3μ				
70W 4μ				
70W 5μ				
114W 2μ				
114W 3μ				
114W 4μ				
114W 5μ				
	0.1 min @ 0°	0.1 min @ 45°	0.3 min @ 0°	0.3 min @ 45°

Figure 5-4 The polarizing images of the liquid crystal cell with the grooved PDMS substrates as the alignment substrate in a pair of cross polarizers. The power of O_2 plasma is 70W and 114W. The treating time is 0.1 min. and 0.3 min.

	0.5 min @ 0°	0.5 min @ 45°	0.7 min @ 0°	0.7 min @ 45°
70W 2µ				
70W 3µ				
70W 4µ				
70W 5µ				
114W 2µ				
114W 3µ				
114W 4µ				
114W 5µ				
	0.5 min @ 0°	0.5 min @ 45°	0.7 min @ 0°	0.7 min @ 45°

Figure 5-4 (cont'd) The polarizing images of the liquid crystal cell with the grooved PDMS substrates as the alignment substrate in a pair of cross polarizers. The power of O₂ plasma is 70W and 114W. The treating time is 0.1 min. and 0.3 min.

	0.9 min @ 0°	**0.9 min @ 45°**	**1.1 min @ 0°**	**1.1 min @ 45°**
70W 2μ				
70W 3μ				
70W 4μ				
70W 5μ				
114W 2μ				
114W 3μ				
114W 4μ				
114W 5μ				
	0.9 min @ 0°	**0.9 min @ 45°**	**1.1 min @ 0°**	**1.1 min @ 45°**

Figure 5-4 (cont'd)The polarizing images of the liquid crystal cell with the grooved PDMS substrates as the alignment substrate in a pair of cross polarizers. The power of O_2 plasma is 70W and 114W. The treating time is 0.1 min. and 0.3 min.

Chapter 6
Optical method for measuring the azimuthal anchoring strength of liquid crystals using pitch values determined in imperfect sample

6.1 Overview

In order to investigate the homogenous alignment ability of the novel alignment method, such as the grooved PDMS substrate, the measurement of the azimuthal anchoring strength is necessary. In this chapter, we demonstrate an improved simple method for measuring the pitch, regardless of any imperfection of the wedge. When a typical sample is placed between a pair of polarizers, many bright and dark fringes are observed because of the birefringence of liquid crystal. The pitch value is determined by counting the number of fringes directly. Furthermore, we will show that the accuracy of the azimuthal anchoring strength determination can be increased by applying the pitch value that is determined by this way, because the principle for determining the twist angle θ is the same as that which is used to determine the pitch value.

6.2 What is the azimuthal anchoring strength

In the technology of liquid crystal displays, the anchoring strength at the liquid crystal-substrate interface is an important index of the alignment property in the development of new alignment methods. There are two types of anchoring strength for nematic liquid crystals: polar anchoring strength and azimuthal anchoring strength. The polar anchoring strength defines the surface energy of liquid crystal molecules and is related to the orientation out of the substrate plane. On the other hand, the azimuthal anchoring strength describes the in-plane surface

energy. Various methods for measuring the azimuthal anchoring strength have been demonstrated. Most of these methods involve optical measurement of the polarization state by measuring the transmission of light through the liquid crystal cell and polarizers. [1]-[4] In all of these methods, a known torque, induced by the application of an external field, [5],[6] the mixing of liquid crystal with a chiral dopant, [7] or the gliding of one substrate, is applied to the liquid crystal and the resulting rotation of the liquid crystal director (which is the unit vector describing the molecular orientation) at the surface is measured.

The test liquid crystal cells with anti-parallel surface alignment and filled with a chiral doped nematic liquid crystal are often used to measure the azimuthal anchoring strength. [7] When the azimuthal anchoring strength is weak, the surface orientation of liquid crystal molecules will deviate from the alignment direction. It is because of a spontaneous twisting power caused by doping with chiral dopant in the nematic liquid crystal. The deviation angle is determined from the balance between the twisting power and the azimuthal anchoring strength. From this deviation angle, the azimuthal anchoring strength can be calculated by using the elastic theory. When the nematic liquid crystal doped with chiral dopant is filled into a anti-parallel liquid crystal cell, the free energy per unit area is obtained as the sum of the elastic energy F_b and the azimuthal anchoring energy F_s as follows,

$$F = F_b + 2F_s ,\qquad (6\text{-}1)$$

where

$$F_b = \frac{1}{2} K_{22} \left(\frac{2\pi}{P} - \frac{\theta}{d} \right) \times d ,\qquad (6\text{-}2)$$

$$F_s = \frac{1}{2} A \sin^2 \frac{\theta}{2} .\qquad (6\text{-}3)$$

Here, K_{22} is the twist elastic constant, P is the natural pitch of the filled chiral nematic liquid crystal, d is the thickness of the liquid crystal layer or the cell gap,

A is the azimuthal anchoring strength, and θ is the twist angle of the director in the liquid crystal cell. According to the minimum energy or $\partial F / \partial \theta = 0$, the azimuthal anchoring strength A can be expressed as

$$A = \frac{2K_{22}}{\sin\theta}\left(\frac{2\pi}{P} - \frac{\theta}{d}\right). \tag{6-4}$$

In this method, the values of P and θ are important. Their uncertainty affects the accuracy of azimuthal anchoring strength A.

6.3 Method for pitch measurement in imperfect sample

The conventional method to determine the pitch is the Grandjean-Cano wedge method, [8] which employs a wedge-shaped cell filled with the chiral nematic liquid crystal. Domains with twist angles that are multiples of π are formed. The disclination lines are formed between two neighboring domains and can be seen both by the naked eye and under a microscope. The difference between the thicknesses of the liquid crystal layer at the adjacent disclination lines is half of the pitch. With a known wedge angle, the pitch can be determined by measuring the spacing between the adjacent disclination lines. However, the wedge is not perfect in reality, as the angles and the spacing between disclination lines are not uniform, because of bending or stress in the glass substrate. An uncertainty as large as 10% is common.

Here, we demonstrate an improved simple method for measuring the pitch, regardless of any imperfection of the wedge. The sample we use to determine the pitch is a typical wedge-shaped sample, which is the same as the one used in the Grandjean-Cano method. The cell is constructed using two indium tin oxide (ITO) glass substrate, the surfaces of which are coated with polyimide SE-130B (from Nissan Co.) and rubbed with nylon fabric. The rubbing directions of the two substrates are anti-parallel to each other. The wedged cell is formed with a piece

of Mylar space at one end and the filled with nematic liquid crystal E7 (from Merck Co.) that is doped with chiral material ZLI-811 (from Merck Co.). A pair of crossed polarizers (the polarizer and the analyzer) is used and the cell is put in between with the rubbing direction having an angle ψ_0 from the polarizer transmission axis. By using an extended white light source such as the common film viewer and a narrow color filter (λ=546 nm), the sample between crossed polarizers shows many bright and dark fringes between two adjacent disclination lines. Both of the fringes and disclination lines can be observed with bare eyes. The pitch value is determined by counting the number of fringes directly. The measuring arrangement is shown in Figure 6-1.The photographs of three samples using different wedge angles, using spacers of different thicknesses, are shown in Figure 6-2. Furthermore, we will show that the accuracy of the azimuthal anchoring strength determination can be increased by applying the pitch value that is determined by this new method.

6.4 Theory and simulation for pitch measurement in imperfect sample

By using Jones matrix method, the optical transmittance T of a twist nematic liquid crystal cell between a pair of polarizers can be written as [9]

$$T = \left[\frac{1}{\sqrt{1+u^2}} \sin\left(\sqrt{1+u^2}\,\theta\right)\sin\left(\theta-\psi_{pol}\right) + \cos\left(\sqrt{1+u^2}\,\theta\right)\cos\left(\theta-\psi_{pol}\right) \right]^2$$
$$+ \frac{u^2}{1+u^2}\sin^2\left(\sqrt{1+u^2}\,\theta\right)\cos^2\left(\theta+2\psi_0-\psi_{pol}\right)$$
(6-5)

where θ is the twist angle of liquid crystal, ψ_{pol} is the angle between the transmission axes of the analyzer and the polarizer, $u = \pi\Delta n d / \lambda\theta$ with Δn being the birefringence of chiral nematic liquid crystal and λ is the wavelength of the light and d the thickness of liquid crystal layer.

In this method, we use a pair of crossed polarizers, so ψ_{pol} is fixed as 90°.

u can be replaced by $\Gamma/2\theta$, where the phase retardation Γ of the wedge sample is $2\pi\Delta nd/\lambda$. The transmittance T can be replaced by

$$T = \frac{1}{\Gamma^2 + 4\theta^2} \left\{ \left[\sqrt{\Gamma^2 + 4\theta^2} \cos\left(\frac{\sqrt{\Gamma^2 + 4\theta^2}}{2}\right) \sin(\theta) \right.\right.$$
$$\left.\left. - 2\theta \cos(\theta)\sin\left(\frac{\sqrt{\Gamma^2 + 4\theta^2}}{2}\right) \right]^2 \right.$$
$$\left. + \Gamma^2 \sin^2\left(\frac{\sqrt{\Gamma^2 + 4\theta^2}}{2}\right) \sin^2(\theta - 2\psi_0) \right\} \tag{6-6}$$

Within each domain in the wedged cell the twist angle θ is fixed, however, the cell gap changes monotonically with position, the phase retardation Γ also changes accordingly with position and the fringe patterns are then resulted in each domain.

Grandjean realized that cholesteric liquid crystal prepared under planar alignment conditions in a wedged cell exhibits disclination lines whenever the twist angle changes by π [8]. When it is between N-th and $(N+1)$-th disclination lines, the twist angle θ is $N\pi$, where $N = 0,1,2$, etc. By substituting $\sin(\theta) = 0$, $\cos^2(\theta) = 1$, $\sin^2(\theta - 2\psi_0) = \sin^2(2\psi_0)$ and $\sin^2\left(\frac{\sqrt{\Gamma^2 + 4\theta^2}}{2}\right) = \frac{1}{2}\left(1 - \cos\left(\sqrt{\Gamma^2 + 4\theta^2}\right)\right)$ into Eq.(6-6), the optical transmittance T can be further simplified as

$$T = \frac{1}{\Gamma^2 + 4\theta^2}\left[4\theta^2 \sin^2\left(\frac{\sqrt{\Gamma^2 + 4\theta^2}}{2}\right) + \Gamma^2 \sin^2\left(\frac{\sqrt{\Gamma^2 + 4\theta^2}}{2}\right) \sin^2(2\psi_0) \right]$$
$$= \frac{1}{2}\left(\frac{\Gamma^2 \sin^2(2\psi_0) + 4\theta^2}{\Gamma^2 + 4\theta^2}\right)\left(1 - \cos\left(\sqrt{\Gamma^2 + 4\theta^2}\right)\right) \tag{6-7}$$

For the domain between N-th and $(N+1)$-th disclination lines the cell gap is between $(2N-1)P/4$ and $(2N+1)P/4$, where P is the pitch value. For

λ =546 nm, Δn =0.243 and P =56 µm, the ratio θ/Γ is about 0.04, i.e., the twist angle θ is much smaller than the phase retardation Γ. We rewrite Eq. (6-7) by the factor of θ/Γ and $(\theta/\Gamma)^2$ which are both much smaller than 1, the equation will be modified as

$$
T = \frac{1}{2} \left(\frac{\sin^2(2\psi_0) + 4\dfrac{\theta^2}{\Gamma^2}}{1 + 4\dfrac{\theta^2}{\Gamma^2}} \right) \left(1 - \cos\left(\Gamma\sqrt{1 + 4\dfrac{\theta^2}{\Gamma^2}} \right) \right)
$$
$$
= \frac{1}{2} \left(\sin^2(2\psi_0) + 4\dfrac{\theta^2}{\Gamma^2} \right) \left(1 - \cos\left(\Gamma\left(1 + 2\dfrac{\theta^2}{\Gamma^2} \right) \right) \right)
$$
(6-8)

This transmittance is a product of two terms. The first term contributes the transmittance amplitude, which increases with the domain order N. The second term is roughly a cosine function of Γ. The fringe patterns are resulted from this term. Because $2\theta^2/\Gamma^2$ is much smaller 1, its effect on the number of fringes is negligible.

At ψ_0 =45°, the first term is close to the constant 1 and the peak of transmittance is almost the same. In Figure 6-3, we show a simulated result for T by applying Eq. (6-8) with λ =546 nm, Δn =0.243, P =56 µm (For E7 with 1% ZLI-811), and ψ_0 =45°. Because the twist angle is discontinuous at each disclination line, the simulated transmittance shows the discontinuity. All the peaks of transmittance are 100% and it is difficult to identify the location of disclination line. If ψ_0 is small, however, an abrupt change of this amplitude is resulted at the positions of disclination lines. Figure 6-4 shows the simulated transmittance at the same chiral nematic liquid crystal cell at ψ_0 =3°. Overall, the transmittance is relatively smaller than the cell at ψ_0 =45°, and the discontinuities at the disclination lines exist in both cases. The number of fringes between two adjacent disclination lines keeps the same regardless of the value for angle ψ_0. Notably, the intensity difference between domains is much prominent for small

ψ_0. Therefore, it is much easier to distinguish the disclination lines if a small ψ_0 is used.

The fringes in each domain is caused by the change of phase retardation Γ within each domain as expressed by the second term in Eq. (6-8). The change of phase retardation between two adjacent bright (dark) lines is 2π, which corresponds to a cell thickness change of $\lambda/\Delta n$. On the other hand, the gap difference between two adjacent disclination lines, which can also be clearly distinguished with bare eyes, is $P/2$. Therefore, the pitch P can be determined by simply counting the fringe number N_f in each domain and using the relation of

$$P = 2N_f \lambda / \Delta n.$$

(6-9)

6.5 Effect on the azimuthal anchoring strength

As mentioned, this is a simple method for measuring the pitch of chiral nematic liquid crystal, which is used in an anti-parallel cell to measure the azimuthal anchoring strength. As described in section 6.2 and by Eq. (6-4), the determination of the twist angle θ is the main part of the measurement of the azimuthal anchoring strength. This angle can be measured using an optical method that is based on the transmittance relation as Eq. (6-5). Varying the angles of the sample and polarizer and determining the minimum transmittance enable the twist angle θ to be determined. Both Eq. (6-5) and Eq. (6-6) are based on the same principle, only that the thickness of the nematic liquid crystal cell is a constant and the angle ψ_{pol} is allowed to vary in the azimuthal anchoring strength measurement. Knowledge of Δn is also required to determine the twist angle.

Since birefringence Δn is used in determining both the value P and the twist angle θ to obtain the azimuthal anchoring strength according to Eq. (6-4),

the error in the azimuthal anchoring strength caused by any error in birefringence Δn is now considered. If the same error of Δn is introduced in measuring both the pitch and the twist angle, then what is the resulting error ΔA in the final measurement of the anchoring strength? Consider a hypothetic cell with an LC thickness of 11.5μm, a true pitch P of 61 μm, a twist elastic constant K_{22} of 6.1×10^{-12} N and a Δn of 0.223. Suppose that the surface has a true azimuthal anchoring strength A whose value lies anywhere between 10^{-3} J/m^2 and 10^{-6} J/m^2. With this A value, the cell has a definite twist angle θ, according to Eq. (6-4). Hence, the angle ψ_{pol} that minimizes the intensity can be determined from Eq. (6-5). Experimentally, the angle ψ_{pol} is measured to deduce θ. However, if an error Δn_{error} applies to Δn, then the deduced value θ' and the pitch value P' that is determined by the presented method differ from the true θ and P, respectively. Then, the azimuthal anchoring strength A' that was calculated using Eq. (6-4) differs from the true value of A, but with an error of ΔA or $A'-A$. Figure 6-5 shows the calculated $\Delta A/A$ against Δn_{error} for four values of A with a wavelength of 0.6328 μm. The azimuthal anchoring strengths A' of the solid curves are calculated using Eq. (6-4) with the deduced twist angle θ' and the true pitch P. The error in A can exceed 5% if Δn_{error} is 0.01 (or 4%). The pitch value P' measured by the presented method was substituted into Eq. (6-4) to yield the calculated error $\Delta A/A$ that is also plotted in Figure 6-5 with dashed curves. The error is negligible for $\Delta n_{error} \leq 0.01$. For $A > 10^{-3}$J/m^2, the curves of $\Delta A/A$ almost overlap that for $A = 10^{-4}$ J/m^2. At $\Delta n_{error} \cong \pm 0.015$, the values of $d\Delta n/\lambda$ are close to half integers. This is a condition of singularity in the measurement, which should be avoided. [9]

Now, the cause of the drastic reduction in error is analytically examined using the measured P' value to deduce the anchoring strength. By differentiating

Eq. (6-4), we obtain

$$\Delta A = \left(-A\theta\cot\theta - \frac{2K_{22}}{\sin\theta}\frac{\theta}{d} \right)\frac{\Delta\theta}{\theta} + \left(-\frac{4\pi K_{22}}{P\sin\theta} \right)\frac{\Delta P}{p}. \qquad (6\text{-}10)$$

Dividing Eq. (6-10) by A in Eq. (6-4) yields,

$$\frac{\Delta A}{A} = \left(-\theta\cot\theta - \frac{\theta/d}{\left(2\pi/P - \theta/d\right)} \right)\frac{\Delta\theta}{\theta} + \left(-1 - \frac{\theta/d}{\left(2\pi/P - \theta/d\right)} \right)\frac{\Delta P}{p}. \qquad (6\text{-}11)$$

The two errors $\Delta\theta/\theta$ and $\Delta P/P$ were caused by Δn_{error} using Eqs. (6-4), (6-5), and (6-9). The results are plotted in Figure 6-6. The solid curves are $\Delta\theta/\theta$ for several A values and the dashed curve is for $\Delta P/P$. The $\Delta\theta/\theta$ values depend only weakly on A. Figure 6-6 shows that approximately,

$$\frac{\Delta P}{P} = -\frac{\Delta\theta}{\theta}. \qquad (6\text{-}12)$$

Substituting the approximation Eq. (6-12) into Eq. (6-11) cancels out most parts of Eq. (6-11). Equation (6-11) can be rewritten as

$$\frac{\Delta A}{A} = (1 - \theta\cot\theta)\frac{\Delta\theta}{\theta}. \qquad (6\text{-}13)$$

The relationships among θ, $\theta\cot\theta$, and the anchoring strength are plotted in Figure 6-7. When the anchoring strength exceeds 10^{-5} J/m^2, the product of θ and $\cot\theta$ is almost equal to one and $\Delta A/A$ in Eq. (6-13) is roughly equal to zero.

However, if the true pitch is used in determining the anchoring strength, ΔP is zero and the second term of Eq. (6-11) does not exist. In this case,

$$\frac{\Delta A}{A} = \left(-\theta\cot\theta - \frac{\theta/d}{2\pi/P - \theta/d} \right)\frac{\Delta\theta}{\theta}. \qquad (6\text{-}14)$$

Figure 6-8 plots relationship between the second term in parentheses, $X = (\theta/d)/(2\pi/P - \theta/d)$, and the anchoring strength A. This value is almost zero when $A > 10^{-5}$ J/m^2. Then $|\Delta A/A|$ becomes $|\Delta\theta/\theta|$. For $A \leq 10^{-6}$ J/m^2, the

X value significantly exceeds $\theta \cot \theta$. Hence, $\left|\Delta A/A\right|$ is roughly equal to $X\left|\Delta\theta/\theta\right|$, which exceeds $\left|\Delta\theta/\theta\right|$. In any case, the error here is much larger than that calculated using the measured pitch value. When the anchoring strength is smaller, this effect is more prominent.

6.6 Summaries

This method for determining the pitch value is simple and accurate. Even if the wedge cell is imperfect, the number of fringes between two adjacent disclination lines remains unchanged. By counting the number of the fringes, the pitch value can be determined. The sensitivity of this new method is $\pm\lambda/2\Delta n$. This method is useful for pitch values that exceed several tens of micrometers, which values for pitch are commonly used to measure the azimuthal anchoring strength. This method does not require the knowledge of the wedge angle of the cells, but rather requires the birefringence value of nematic liquid crystal. This fact seems to be a drawback of this method. However, the principle of measuring the twist angle in determining the azimuthal anchoring strength is the same as that used here, the accuracy of azimuthal anchoring strength is further improved with this method than that can be obtained the true pitch value. According to the simulation based on the calculations herein, the error in the anchoring strength determination can be reduced by a factor of about 10.

References

[1] Y. Iimura, M. Kobayashi, and S. Kobayashi, "A New Method for Measuring the Azimuthal Anchoring Energy of a Nematic Liquid Crystal," *Jpn. J. Appl. Phys. Part 2* **33**, L434 (1994).

[2] T. Akahane, H. Kaneko, and M. Kimura, "Novel Method of Measuring Surface Torsional Anchoring Strength of Nematic Liquid Crystals," *Jpn. J. Appl. Phys. Part 1* **35**, 4434 (1996).

[3] J. G. Fonseca and Y. Galerne, "Simple method for measuring the azimuthal anchoring strength of nematic liquid crystals," *Appl. Phys. Lett.* **79**, 2910 (2001).

[4] M. Kawamura, Y. Goto, and S. Sato, "Determination of Anchoring Energy in Nematic Liquid Crystal Cells with Controllable Twist Angles Using a Stokes Parameter Method," *Jpn. J. Appl. Phys. Part 1* **43**, 6239 (2004).

[5] T. Oh-ide, S. Kuniyasu, and S. Kobayashi, "Surface Coupling between Nematic Liquid Crystals and Rubbed Polyimide Substrates for Pure Twist Deformation: Dependence on Rubbing Strength," *Mol. Cryst. Liq. Cryst.* **164**, 91 (1988).

[6] S. Faetti and G. C. Mutinati, "Light transmission from a twisted nematic liquid crystal: Accurate methods to measure the azimuthal anchoring energy," *Phys. Rev. E* **68**, 026601 (2003).

[7] Y. Sato, K. Sato, and T. Uchida, "Relationship between Rubbing Strength and Surface Anchoring of Nematic Liquid Crystal," *Jpn. J. Appl. Phys. Part 2* **31**, L579 (1992).

[8] R. Cano, "An explanation of Grandjean discontinuities," *Bull. Soc. Fr. Mineral. Cristallogr.* **91**, 20 (1968).

[9] Y. Saitoh and A. Lien, "An Improved Azimuthal Anchoring Energy Measurement Method Using Liquid Crystals with Different Chiralities," *Jpn.*

J. Appl. Phys. Part 1 **39**, 1743 (2000).
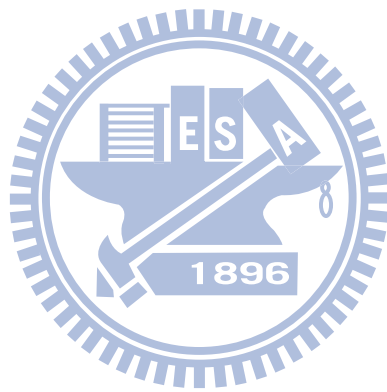
Figures
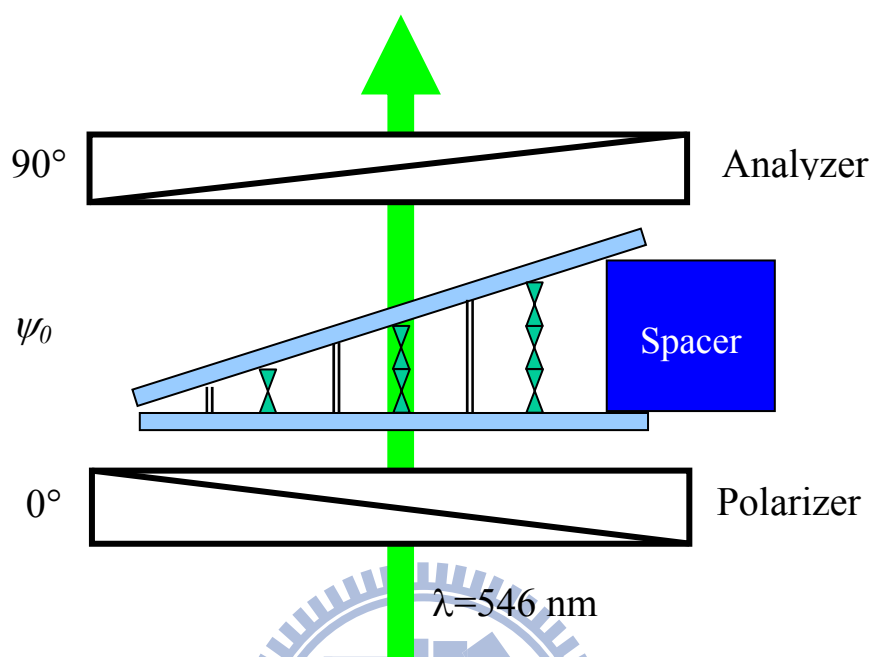
Figure 6-1 The setup of this new method. The incident light is monochromatic.
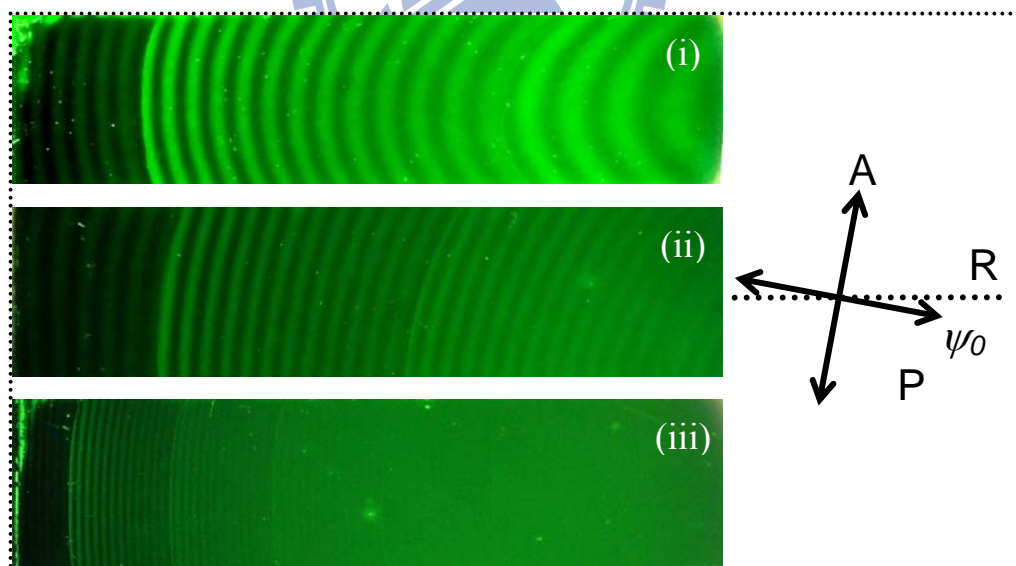
Figure 6-2 Photographs of the wedged samples with different spacers at the wider end: (a) 50 μm (b) 75 μm (c) 250 μm. P: polarizer axis, A: analyzer axis, and R: rubbing direction.
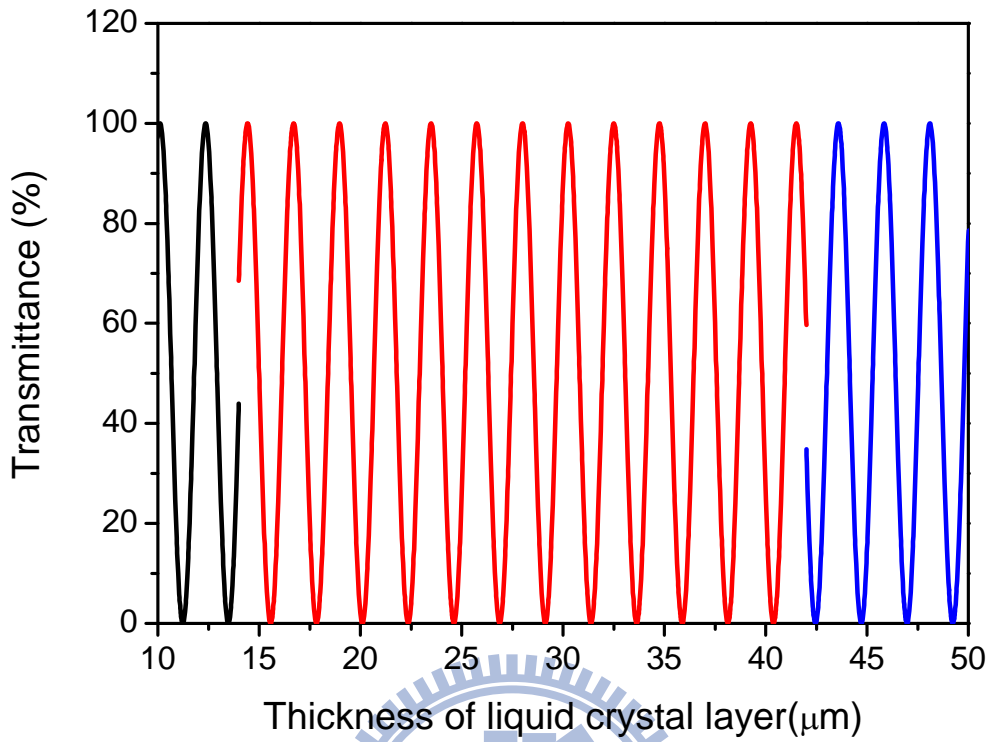
Figure 6-3 Transmittance simulation of the wedge cell with $\psi_0=45°$.
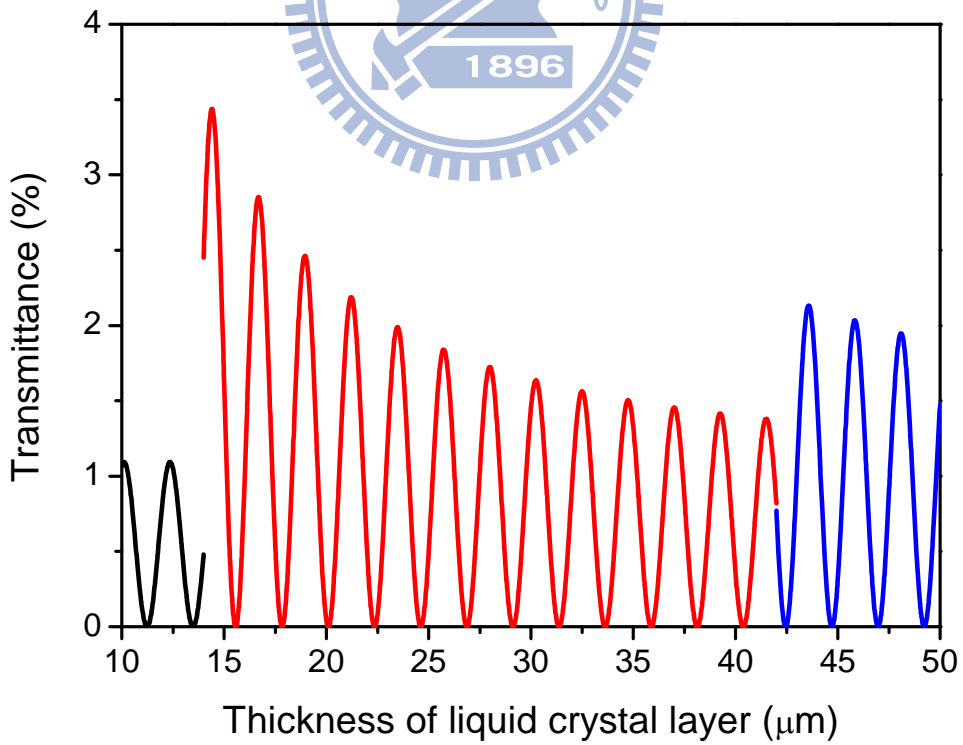
Figure 6-4 Transmittance simulation of the wedge cell with $\psi_0=3°$.
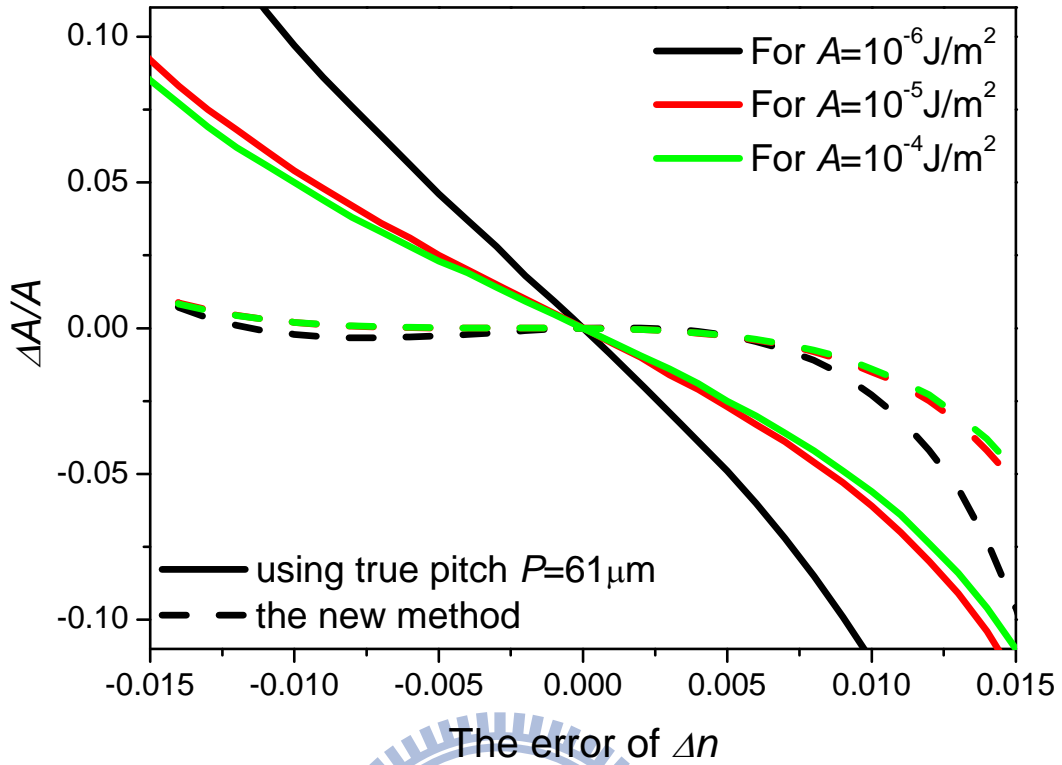
Figure 6-5 Analysis of error of anchoring strength, $\Delta A/A$, versus error in birefringence Δn. Solid curves are calculated using the true pitch value. Dashed curves are calculated using the pitch value measured with the presented method.
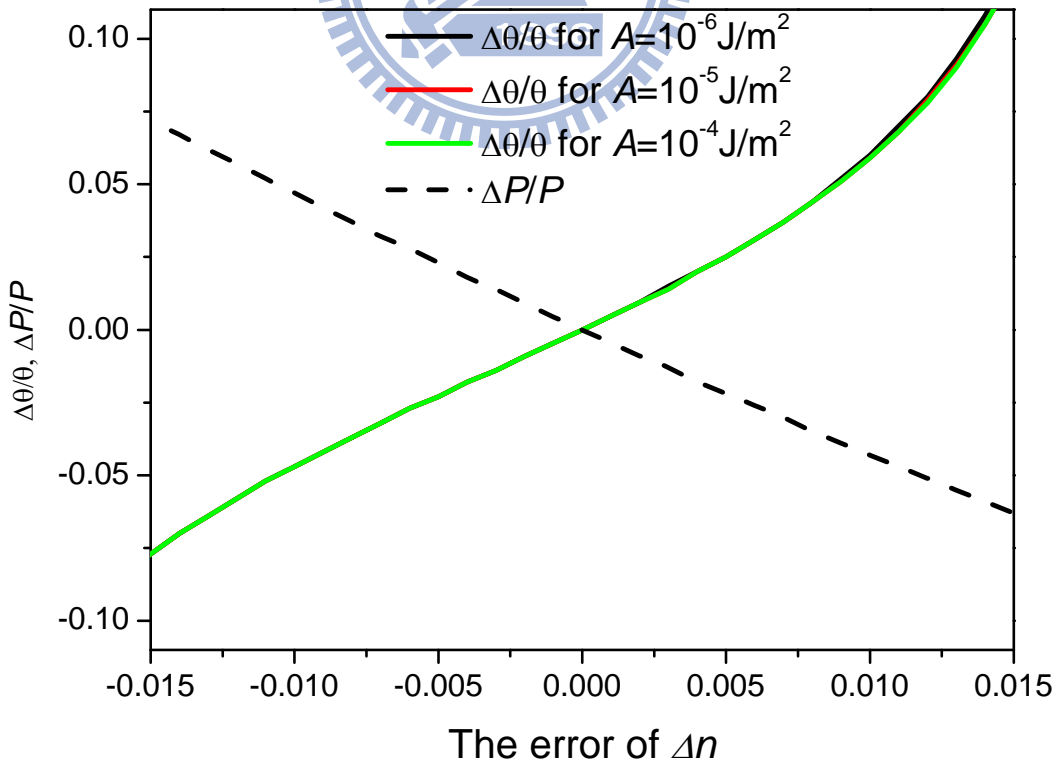
Figure 6-6 Solid curves plot the error ratio $\Delta\theta/\theta$ versus A. Dashed lines plot $\Delta P/P$ versus A.
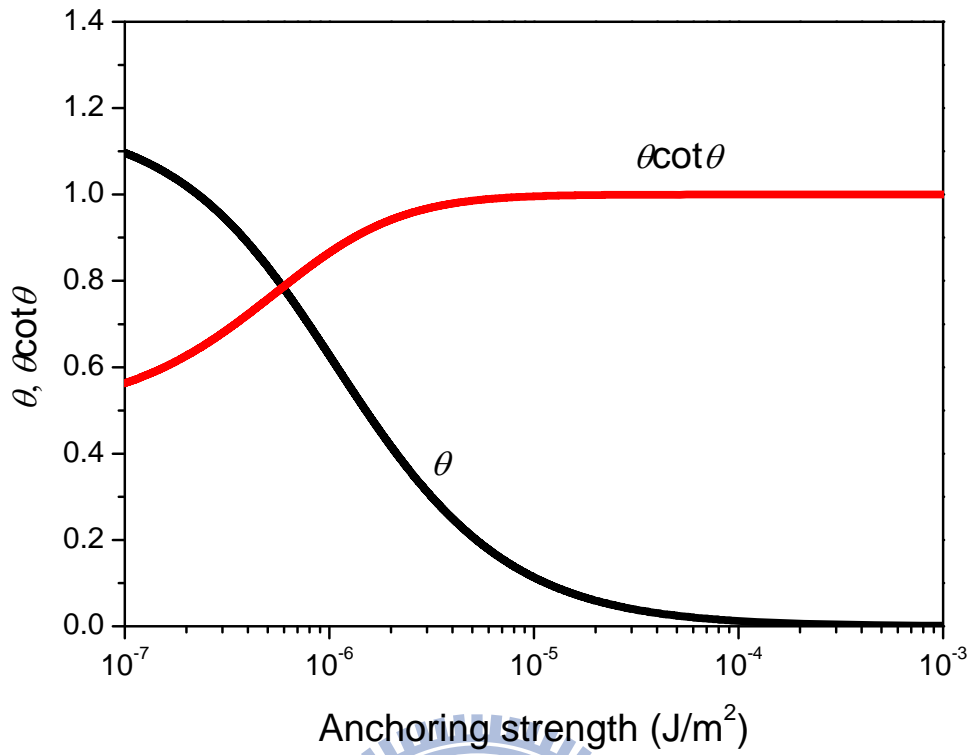
Figure 6-7 Relationships among twist angle θ, $\theta\cot\theta$ and anchoring strength.
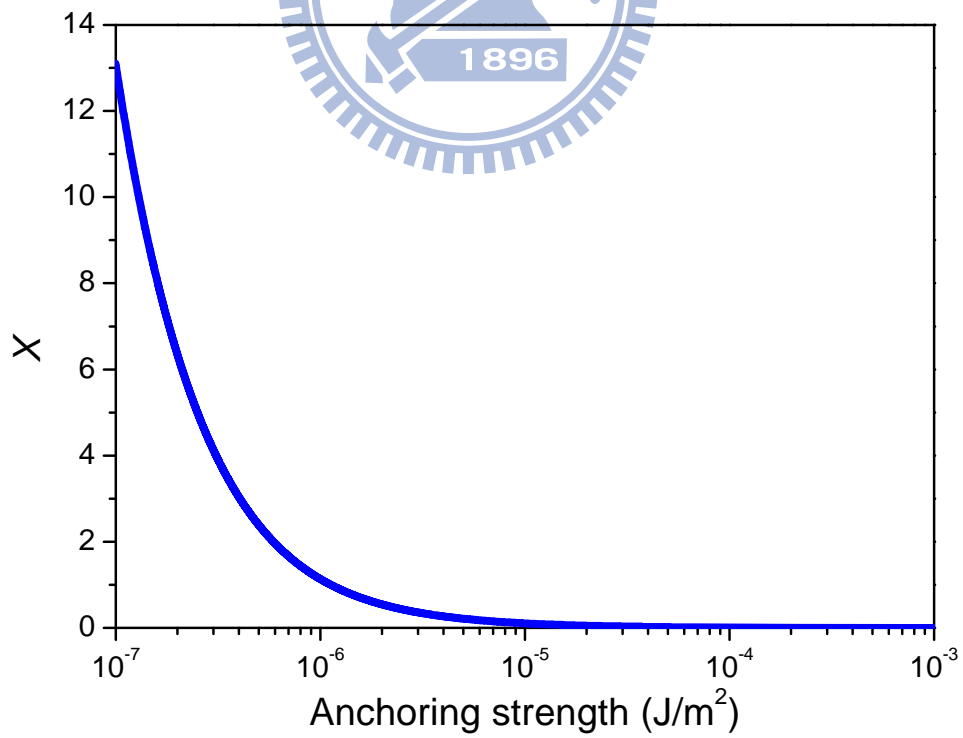
Figure 6-8 Relationship between $X=(\theta/d)/(2\pi/P-\theta/d)$ and anchoring strength.

Chapter 7
Future research topics about this thesis

7.1 The anodic aluminum oxide alignment method

In this thesis, we have successfully developed a novel alignment method by using the anodic aluminum oxide (AAO) thin film as the alignment layer. This AAO thin film can align the liquid crystal vertically. By modified the pore diameter, and the aspect ratio, the alignment ability is controllable. Because the AAO thin film can align the liquid crystal homogenously in some specific condition, the alignment mechanism of liquid crystal on the AAO thin film is not clear enough. Further researches about the alignment mechanism are progressing.

Recently, the phase of UV beam in the attosecond generation application can be modified by using a liquid crystal cell as a phase shifter.[1] However, the alignment layer of the liquid crystal cell is easily modified by the UV beam, and the phase modification is changed depending on the irradiative time. Because the AAO alignment layer is an inorganic material, the alignment property is hard to be modified by using the photoalignment method. Therefore, the AAO thin film can be a good alignment layer for the phase shifter in the attosecond generation system.

The other type of AAO thin film is the non-porous AAO thin film which is anodizing in the neutral electrolyte. Our group progress the research about the liquid crystal alignment on the non-porous AAO thin film. This research helps us to understand the liquid crystal molecules align by the pore array on the AAO surface or by the AAO material.

For the practical applications, our group collaborates with Prof. Fang's group in department of power mechanical engineering, National Tsing Hua University. We try to anodize the aluminum thin film on the Indium-Tin Oxide (ITO) glass substrate, and than make the electrically controllable liquid crystal

device with the AAO alignment layer. Because the acid electrolyte can anodize the aluminum thin film and etch the ITO electrode in the same time, it is difficult to anodize the aluminum thin film on the ITO thin film. By using a thin Titanium (Ti) thin film as the template layer, we have successfully anodized the aluminum thin film on ITO glass substrate. Figure 7-1 shows the FESEM image of the AAO thin film on the ITO glass substrate. The thickness of the ITO thin film and the Ti layer are round 200 nm and 20 nm, respectively. It clearly shows the ITO and Ti layers both remain under the porous AAO thin film in Figure 7-1 (a). Figure 7-1 (b) shows the top view of the AAO thin film. It still remains the hexagonal pores array. By using these AAO-ITO thin films, the prototypical cell has been constructed. The on-state and off-state are shown in Figure 7-2. It clearly shows the cell with AAO-ITO thin films as the alignment layers is controllable by the applied voltage.

According to this process, the polar anchoring strength of the AAO alignment layer can be measured by using the electric method. The other electric properties of the liquid crystal device with AAO alignment layer can be investigated. Further researches should be worked to understand the mechanism of the liquid crystal alignment on the AAO thin film which helps us controlling the alignment ability and the pretilt angle.

7.2 The optical constants analysis in terahertz region

The optical constants analysis program for the THz-TDS signal has been discussed in Chapter 4. We have considered the thickness difference between the sample substrate and the reference substrate, and the Febry-Perot effect in this program. It solves most of problems and gives the user the consistent optical constants, such as the complex refractive index and the attenuation coefficient. For the Febry-Perot modification, the constant sample thickness is used in this analysis program. Although most of the multiple reflective signals can be

canceled by the Febry-Perot term, there is still small fluctuation of the resulting optical constants. By using thicker substrate, such as several millimeters, the first reflective signal can be delayed away from the main signal. Then, the first reflective signal can be deleted manually, and the Febry-Perot effect can be totally neglected.

On the other hand, further modification can be done by considering the sample thickness is a variable. Instead of the sample thickness, the total optical path difference between the transmitted wave and the first reflective wave, $2\tilde{n}_S d_S$, is constant. After this modification, we believe it can cancel the small fluctuation of the resulting optical constants. In order to measure the thinner sample, this further modification is necessary.

References

[1] W. J. Chen, Z. M. Hsieh, S. W. Huang, H. Y. Su, T. T. Tang, R. P. Chao, C. L. Pan, C. K. Lee, and A. H. Kung, "Sub-Single-Cycle Optical Pulse Train with Constant Carrier Envelope Phase," *Phys. Rev. Lett.* **100**, 163906 (2008).
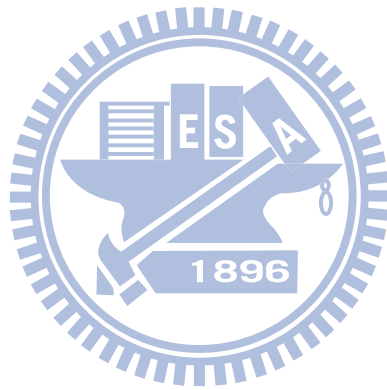
Figures

(a)
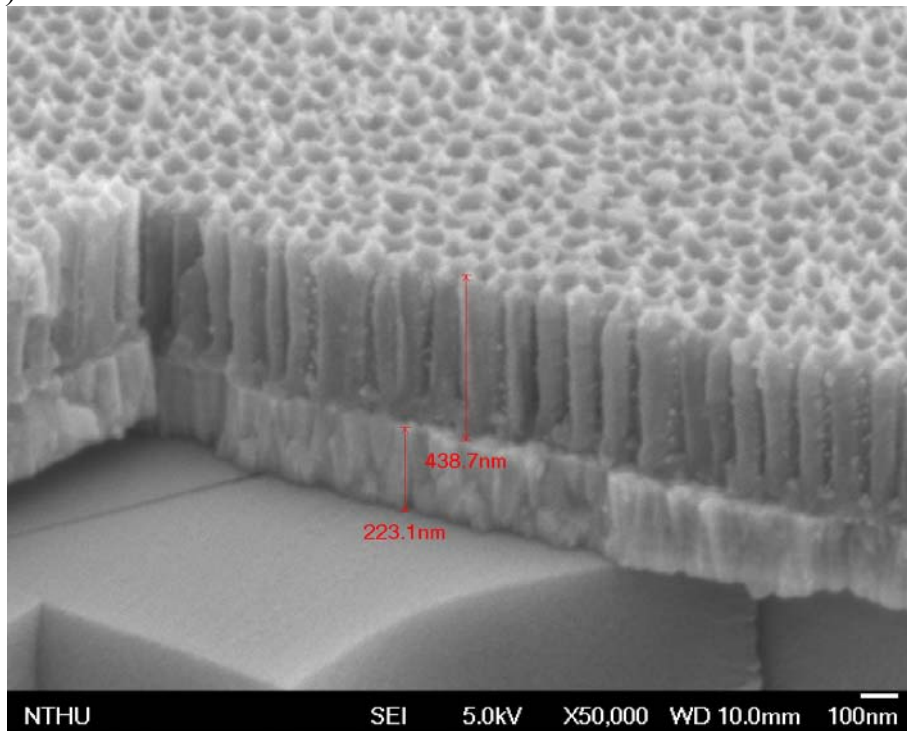
(b)
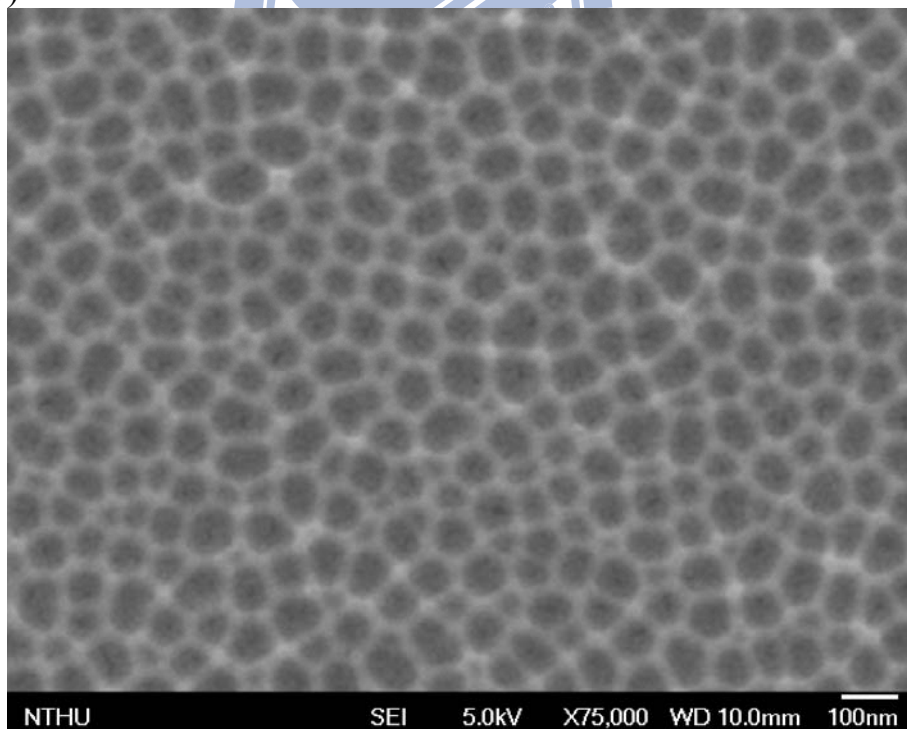
Figure 7-1 FESEM images of the AAO thin film on the ITO glass substrate. (a) the side view, (b) the top view.
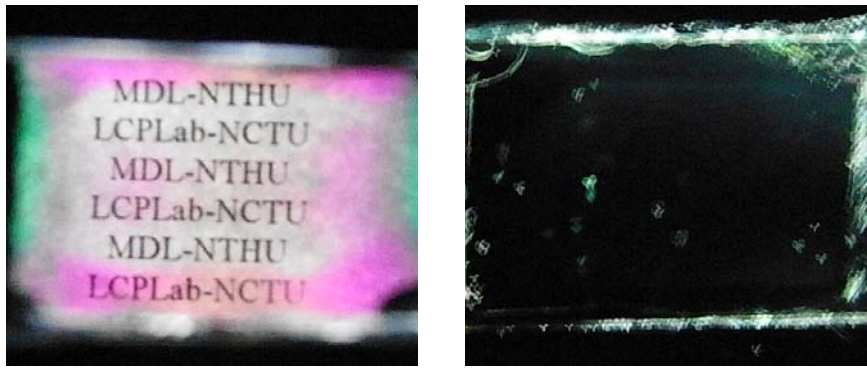
Figure 7-2 The on-state and off-state of the prototypical cell with the AAO-ITO thin films as the alignment layers.

Appendix A
Anodic Aluminum Oxide (AAO)

A.1 Overview

Anodic aluminum oxide (AAO) is a widely studied material that is used for corrosion protection of aluminum surface or as dielectric material in microelectronics application. AAO has been studied extensively over five decades. [1] There are two forms of AAO, the nonporous barrier oxide and the porous oxide. When aluminum (Al) is anodized in neutral or basic solutions (pH>5), a flat, nonporous, featureless insulating "barrier" oxide forms, the "barrier-type film". When Al is anodized in an acid, deep pores can form with diameters varying between 5 and 100 nm. The diameter of pores depends on the pH value of the electrolyte, the anodization voltage and the choice of the acid. This porous structure has been called "pore-type film". The pore-type film has been reported to be a typical self-assembled nanochannel material. [2],[3] It exhibits a homogenous morphology of parallel pores which grow perpendicular to the substrate with nanometer-scale diameters and interpore spacings. These films are usually formed through anodizing bulk aluminum plates or foils at constant voltage in various acidic electrolytes such as sulfuric, phosphoric, chromic, citric, oxalic acid, etc. [4]-[6] By using this method, it is easy to form an ordered array of hexagonal columnar structures. Each of the hexagonal columnar structures contains an elongated cylindrical pore normal to the aluminum surface. Such films present uniform pore sizes (between 10nm and several 100 nm), high pore densities (ranging from 10^9 to 10^{12} cm^{-2}), and high aspect ratios (>20). By using the porous AAO as templates, various nanometer sized materials, including metals, semiconductors, organics and polymers, have been reported. [7]-[9]

A.2 Manufacture procedures

In this thesis, we used display-grade glass substrates (Wintek Corporation, Taiwan) coated with indium tin oxide (ITO) on one side, and AAO films were fabricated on the side of the substrates without the ITO coating. First, a thermal coating system to evaporate a pure aluminum (99.99%) film on clean glass substrates. The thickness of the aluminum film was about 300nm or 500nm for different experiments. Then, the aluminum film was anodized under a constant voltage with 3 wt% oxalic acid ($H_2C_2O_4$) aqueous solution in a home-made electrochemical trough. The temperature of the anodic solution was controlled at 6.0±0.5°C. A platinum plate was used as the cathode. By using a voltage supply (Model 2410 sourcemeter, Keithley), the dc anodization voltage was varied between 20V and 70 V while the anodization current was monitored simultaneously. Figure A-1 shows the scheme of the anodizing system. The homemade system is constructed of a Pt cathode, an Al anode, a DC power supply and a water cooling system.

Fabrication process of the AAO thin film is carried out using the processes shown schematically in Figure A-2. The anodization processes in this thesis are two different processes, one-step process and two-step process. For the one-step process, the aluminum film was directly anodized until the anodization current became zero, where the whole aluminum film was anodized to become AAO, as shown in Figure A-2 (a). According to the thickness of aluminum film and the total anodization time of the one-step process, the anodization rate for AAO could be determined. The AAO thin film formed by one-step process had irregular pore configuration and the pores were usually not straight either.

In order to produce the highly ordered hexagonal pore arrays, we followed Masuda and Satoh [10] by employing a two-step process as shown schematically in Figure A-2 (b). The first step was an anodization process, same as one-step process, but the anodization time was determined by the required thickness of AAO film and the anodization rate. Then, the substrate with the first AAO thin layer was immersed in a mixture of chromic acid (1.5 wt% H_2CrO_4) and

phosphoric acid (6 wt% H_3PO_4) at 60°C for 40 min to remove the AAO film on top of the aluminum layer. Now, a textured pattern of concaves was obtained on the surface of the remaining aluminum layer (see Figure 4-2 (b)). Next, in the second anodization, the sample was anodized again using the identical parameters as those in the first anodization. In this step, each concave of the surface resulted in the ordered formation of the pores. The AAO thin films with regular cylindrical pores were created from the regularly spaced concaves.

A.3 Morphology

The nanostructure and the morphology of the AAO films were observed using a field emission scanning electron microscope (FESEM: S-4700i, Hitachi). In order to minimize the charge effect, we use the sputter to evaporate a thin platinum or gold layer on the AAO thin films. This thin platinum of gold layer will ground the charge from the AAO thin films. Figure A-3 (a) shows the SEM image of the AAO thin film formed by using the one-step process. There were some crack-like structures connecting the irregular small pores on the surface of the AAO thin film. By using the two-step process, the surface of the AAO thin film had regular pores as shown in Figure A-3 (b). The nanometer pores in the two-step AAO thin films were more obvious than those in the one-step AAO thin films. These pores were self-assembled into hexagons. Figure A-3 show the side view of the AAO thin films. For the one-step AAO thin film, Figure A-4 (a), the columnar pores were not obvious, and the alumina walls were larger than the pores. In the two-step process, the mixture of chromic acid and phosphoric acid not only remove the first AAO layer but also expend the diameter of the pores. Therefore, the pores were larger than the alumina walls, and the columnar pore structures of two-step AAO thin films were more obvious than those of one-step AAO thin films.

A.4 The theoretical mechanism of AAO formation [11]-[13]

When AAO is formed, the electric field and the hydrogen ions at the oxide/electrolyte interface play important roles. After depositing the Al thin film on the substrate, the Al substrates are stored in air. It will automatically form a thin oxide layer on the surface. There are a lot of nano-pits on the surface, and some of these pits can develop into pore nuclei. Because the air-formed oxide layer may be thin and non-uniform, it will support a large electric field gradient across the whole oxide layer. The electric field and the ionic current density should be larger at the pit bottoms and pore bottoms than between the pits and pores.

When we apply the anodization voltage, Al^{3+} ions form at the metal/oxide interface,

$$Al_{(solid)} \rightarrow Al^{3+}_{(oxide)} + 3e^-, \qquad (A-1)$$

and transfer into the oxide layer. The dissociation of oxalic acid will generate conjugate base anions,

$$HC_2O^-_{4(aq)} \rightarrow C_2O^{2-}_{4\ (oxide)} + H^+_{(aq)}, \qquad (A-2)$$

and the water-splitting reaction,

$$\frac{3}{2}H_2O_{(liquid)} \rightarrow 3H^+_{(aq)} + \frac{3}{2}O^{2-}_{(oxide)}, \qquad (A-3)$$
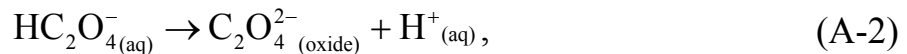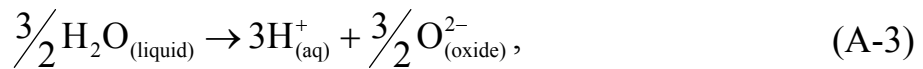
occurs at the oxide/electrolyte interface. Because of the applied electric field, the $O^{2-}_{(oxide)}$ ions transfer within the oxide from the oxide/solution interface toward the metal/oxide interface, to form Al_2O_3,

$$Al^{3+}_{(oxide)} + \frac{3}{2}O^{2-}_{(oxide)} \rightarrow \frac{1}{2}Al_2O_{3\,(oxide)}. \qquad (A-4)$$
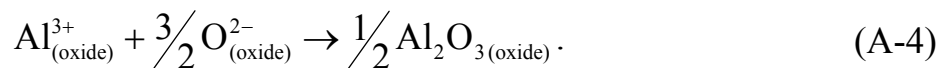
The protons H^+ from the dissociation of oxalic acid can locally dissolve more oxide,

$$\tfrac{1}{2}Al_2O_{3\,(solid)} + 3H^+_{(aq)} \rightarrow Al^{3+}_{(aq)} + \tfrac{3}{2}H_2O_{(liquid)}. \qquad\qquad (A\text{-}5)$$
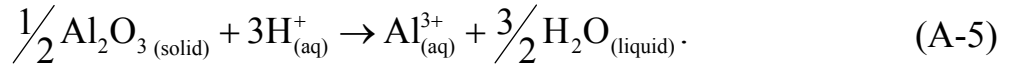
In neutral or basic electrolyte (pH>5), there is no or less protons H^+ from the dissociation of acid, and the Al_2O_3 dissolution process will not happen. It will let the Al film form the non-porous barrier-type film.

Most of the oxide produced by the water splitting reaction (A-3) constructs the sidewalls of the porous AAO film. According to the side view SEM image, Figure A-4, the pore walls are uniform through their length. Therefore, the key growth step must be near the pore bottom, probably very close to the circle of intersection between the cylinder of the pore wall and the spherical segment of the pore bottom. At the circle of intersection the water-splitting reaction (A-3) must also occur, but the Al_2O_3 dissolution process (A-5) should not occur. Thus the porous oxide can feed by Al^{3+} ions from the pore bottom, and from $O^{2-}_{(oxide)}$ ions from the sidewall of the pore. The hydronium ions can also transfer toward the platinum cathode, and combine with the electron e^-. Then, the combination will generate H_2 gas, completing the circuit:

$$3H^+_{(aq)} + 3e^- \rightarrow \tfrac{3}{2}H_{2\,(gas)}. \qquad\qquad (A\text{-}6)$$

Therefore, there are some H_2 bubbles producing at the platinum cathode.

The porous AAO structures usually start from some Al surface that is fairly smooth, but with some pits formed at lattice imperfections or electro-polishing. All of these Al pits will be covered by a thin air-formed oxide layer, so that both the metal/oxide and the oxide/electrolyte interfaces are locally curved. These pits will let the oxide thickness become uniform or irregular. The thin air-formed oxide layer incompletely covers the Al metal surface. As the anodization process starts, the native oxide layer is thicker in some parts of the surface, allowing the electric field to concentrate where the native oxide is thinner. As pore growth continues, a curved metal/oxide interface is maintained or reestablished at the pore bottom, to match the curved oxide/electrolyte interface. Once small pores have formed, the acid and electric potential penetrate into the pore, and the growth

becomes self-catalyzing. If the pores are not ordered, then a horizontal mobility of ions in the barrier layer allows for reordering the pores, until an equilibrium hexagonal ordering is reached. This is why the pore structures of the two-step AAO film are more uniform than which of the one-step AAO film.

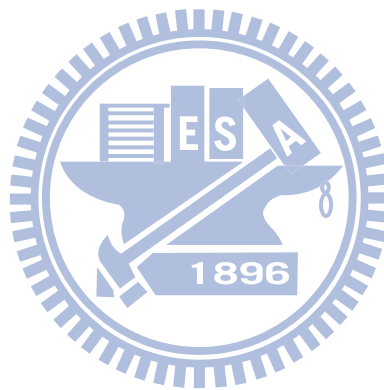Figure A-4 shows the possible elementary process involved in the porous AAO thin film growth. In the electrolyte, the water becomes H^+ and O^{2-}, and the oxalic acid dissociates resulting $C_2O_4^{2-}$ and H^+. The protons H+ dissolve Al_2O_3 in the bottom of pore. The dissolved Al^{3+} and the Al^{3+} from the metal/oxide interface combine with O^{2-}, and grow Al_2O_3 in the sidewall of the pore.

References

[1] F. Keller, M. S. Hunter, and D. L. Robinson, "Structural Features of Oxide Coatings on Aluminum," *J. Electrochem. Soc.* **100**, 411 (1953).

[2] H. Masuda and K. Fukuda, "Ordered Metal Nanohole Arrays Made by a Two-Step Replication of Honeycomb Structures of Anodic Alumina," *Science* **268**, 1466 (1995).

[3] H. Masuda, F. Hasegawa, and S. Ono, "Self-Ordering of Cell Arrangement of Anodic Porous Alumina Formed in Sulfuric Acid Solution," *J. Electrochem. Soc.* **144**, L127 (1997).

[4] O. Jessensky, F. Müller, and U. Gösele, "Self-organized formation of hexagonal pore arrays in anodic alumina," *Appl. Phys. Lett.* **72**, 1173 (1998).

[5] A. P. Li, F. Müller, A. Bimer, K. Nielsch, and U. Gösele, "Hexagonal pore arrays with a 50–420 nm interpore distance formed by self-organization in anodic alumina," *J. Appl. Phys.* **84**, 6023 (1998).

[6] A. P. Li, F. Müller, A. Bimer, K. Nielsch, and U. Gösele, "Polycrystalline nanopore arrays with hexagonal ordering on aluminum," *J. Vac. Sci. Technol. A* **17**, 1428 (1999).

[7] T. Kyotani, L. F. Tsai, and A. Tomita, "Preparation of ultrafine carbon tubes in nanochannels of an anodic aluminum oxide film," *Chem. Mater.* **8**, 2109 (1996).

[8] D. Routkevitch, T. Bigioni, M. Moskovits, and J. M. Xu, "Electrochemical fabrication of CdS nanowire arrays in porous anodic aluminum oxide templates," *J. Phys. Chem.* **100**, 14037 (1996).

[9] D. Al-Mawlawi, C.Z. Liu, and M. Moskovits, "Nanowires formed in anodic oxide nanotemplates," *J. Mater. Res.* **9**, 1014 (1994).

[10] H. Masuda, and M. Satoh, "Fabrication of gold nanodot array using anodic

porous alumina as an evaporation mask," *Jpn. J. Appl. Phys.* **35**, L126 (1996).

[11]J. P. O'Sullivan, and G. C. Wood, "The morphology and mechanism of formation of porous anodic films on aluminum," *Proc. Roy. Soc. Lond. A.* **317**, 511 (1970).

[12]V. P. Parkhutik, and V. I. Shershulsky, "Theoretical modeling of porous oxide growth on aluminum," *J. Phys. D: Appl. Phys.* **25**, 1258 (1992).

[13]F. Li, L. Zhang, and R. M. Metzger, "On the growth of highly ordered pores in anodized aluminum oxide," *Chem. Mater.* **10**, 2470 (1998).

Figures
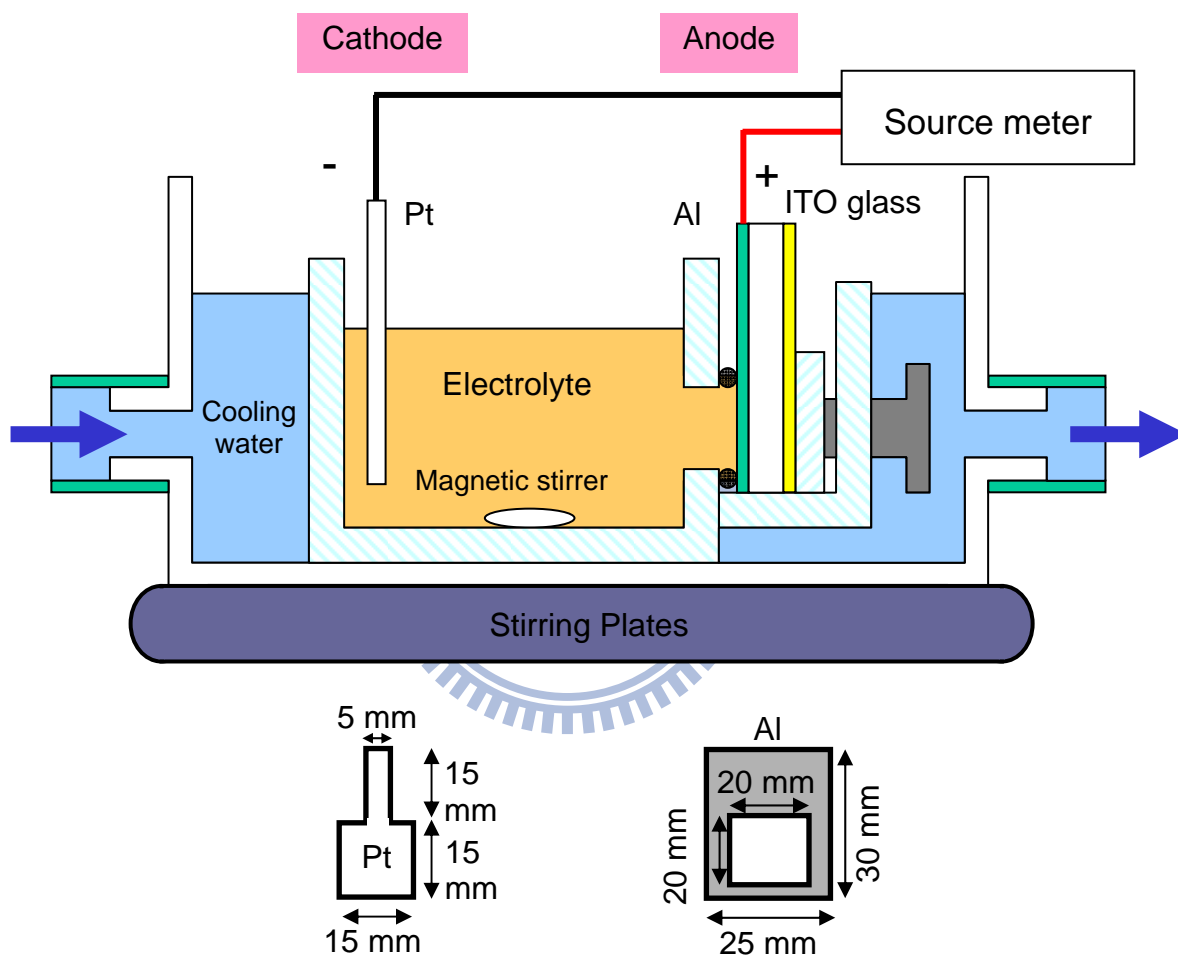
Figure A-1 Scheme of the anodizing system.

(a)

Al

Glass

Only 1st anodization →

Al_2O_3

Glass

(b)

Al

Glass

1st anodization →

Al_2O_3

Al

Glass

Al_2O_3 removal

Al_2O_3

Glass

← 2nd anodization

Al

Glass

Figure A-2 Processes of forming anodic aluminum oxide films: (a) the one-step process, and (b) the two-step process.
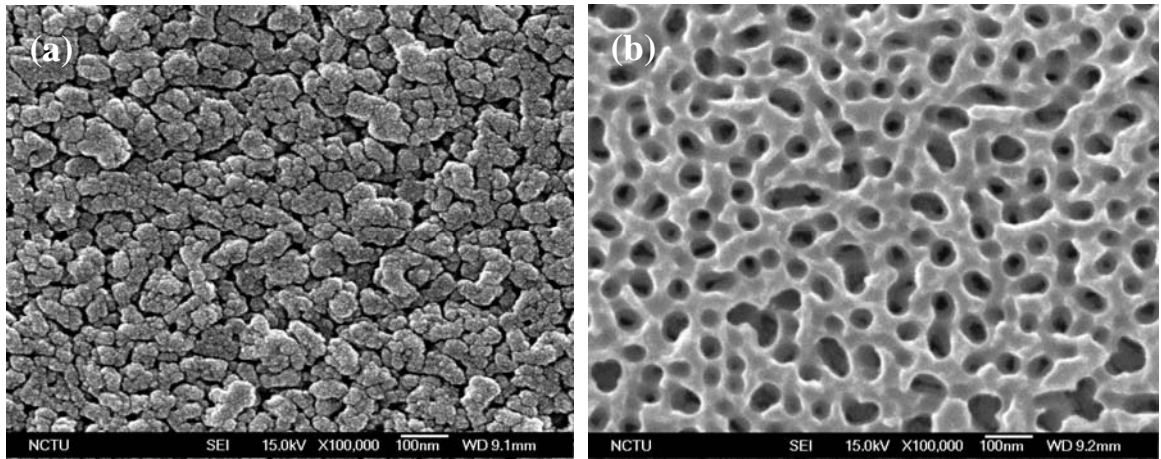
Figure A-3 FESEM images of the AAO thin film. (Top view) (a) one-step AAO thin film, (b) two-step AAO thin film.
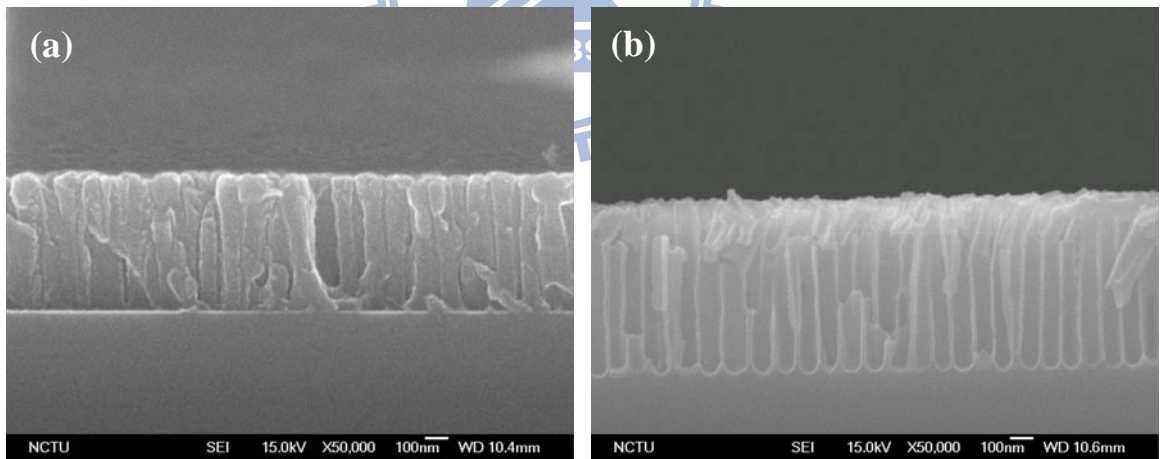
Figure A-4 FESEM images of the AAO thin film. (side view) (a) one-step AAO thin film, (b) two-step AAO thin film.
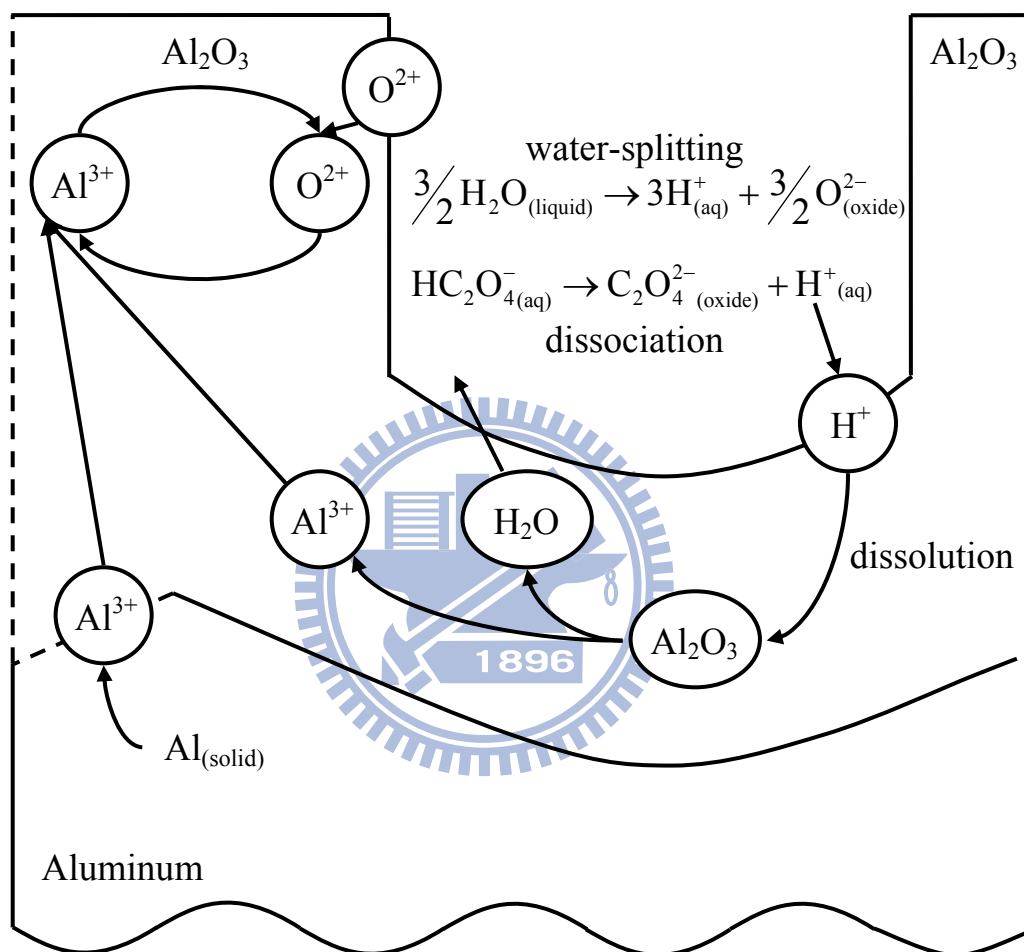
Figure A-5 Scheme of the elementary process involved in the porous AAO thin film growth.

Appendix B
The polar anchoring strength measurement

B.1 Overview

The liquid crystal displays have been widely used in the high technology field, such as personal computer, home theater, and mobile PDA. In the technology of liquid crystal displays, the surface alignment layer has been widely used to obtain a uniform director configuration without any external field. The anchoring strength has been a critical index that helps us to characterize the surface alignment ability quantitatively. There are two types of anchoring strength for nematic liquid crystals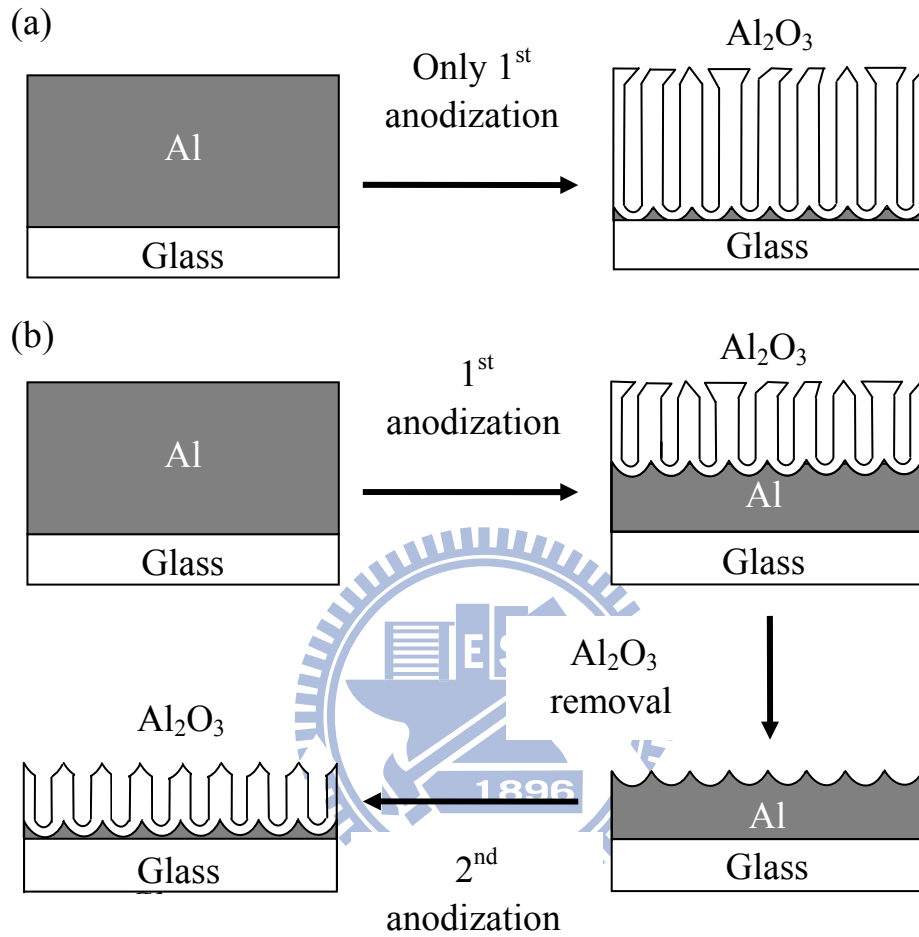: polar anchoring strength and azimuthal anchoring strength. The approximation for surface energy F_s of the liquid crystal on the alignment layer can be written as

$$F_s = \frac{1}{2}\left(A_a \sin^2\theta_a + A_p \sin^2\theta_p\right).$$ (B-1)

Here, A_a and A_p are defined as the azimuthal anchoring strength and the olar anchoring strength, respectively. θ_a and θ_b are the small deviated angle in the azimuthal and polar direction, respectively. Figure B-1 presents the relationship between the liquid crystal director and the Cartesian coordinate.

About the azimuthal anchoring strength, we have discussed in Chapter 6. Here, we just discuss the polar anchoring strength. The polar anchoring strength defines the surface energy of liquid crystal molecules and is related to the orientation out of the substrate plane. At the interface between the liquid crystal and the alignment layer, the interaction has usually been characterized by two parameters, the easy axis of the liquid crystal director at the interface and an polar anchoring anisotropy having a cosine-square dependence on the polar angle with respect to the easy axis. There are several methods to measure the polar anchoring anisotropy. [1]-[5] Most of these methods are performed near the threshold field

region of the Freedericksz transition. Yang and Rosenblatt proposed a method to measure the polar anchoring by applying the magnetic field. [5] In this method, we measure the transmittance of a vertically aligned cell as a function of the applied magnetic field above the threshold magnetic field.

B.2 The theoretical expressions

In a vertically aligned cell, the liquid crystal molecules are aligned nearly perpendicular to the substrate surface. Consider a nematic layer of thickness d confined between two vertically aligned substrates located at $z = 0$ and $z = d$. Figure B-2 shows the scheme of the liquid crystal molecules distribution in a vertically aligned cell. Consider a nematic liquid crystal layer of the thickness d confined between two vertical alignment substrate at $z = 0$ and $z = d$ of the Cartesian coordinate system. An external magnetic field H is applied to the liquid crystal layer along the x axis. Here, we assume the liquid crystal molecules always lie in the x-z plane. Without the external magnetic field, the liquid crystal molecule directors are approximately parallel to the z-axis. The tilt angle between the liquid crystal director and the x-axis at (x, z) position is denoted by $\theta_p(z)$, a function of the position z. If the polar anchoring strength of the vertical alignment surface is the same for both substrates, the director distribution of the entire liquid crystal layer is symmetric with respect to the $z = d/2$ plane. Based on the Oseen and Frank elastic continuum theory of the nematic liquid crystal layer with applying an external magnetic field along the x-axis, the relative free energy of this system per unit area in the x-y plane can be written as

$$F = \int_0^d f(z) dz.$$
(B-2)

The function $f(z)$ can be expressed as

$$f(z) = f_d + f_M + 2f_s,$$
(B-3)

where f_d, f_M, and f_s are the distortion energy density, the magnetic energy

density, and the surface energy density, respectively. According to the Oseen-Frank elastic continuum theory, the entire function $f(z)$ can be presented as

$$f(z) = \frac{1}{2}\left(k_{11}\cos^2\theta_p + k_{33}\sin^2\theta_p\right)\left(\frac{\partial\theta_p}{\partial z}\right)^2 - \frac{1}{2}\chi_a H^2\sin^2\theta_p$$
$$- A_p\sin^2\theta_p\left[\delta(z) + \delta(z-d)\right] \tag{B-4}$$

where k_{11} and k_{33} are the splay and bend elastic constants of the liquid crystal, respectively. χ_a is the magnetic anisotropy of the liquid crystal. $\delta(z)$ is the Dirac delta function. A_p is the polar anchoring strength.

According to the Euler-Lagrange equation,

$$\frac{\partial f}{\partial \theta} = \frac{d}{dz}\frac{\partial f}{(\partial\theta/\partial z)}, \tag{B-5}$$

the boundary condition due to the balance of torque at $z = 0$ is,

$$\frac{d}{dz}\left[\left(k_{11}\cos^2\theta_p + k_{33}\sin^2\theta_p\left(\frac{\partial\theta_p}{\partial z}\right)^2 - \chi_a H^2\sin^2\theta_p\right)\right] = 0. \tag{B-6}$$

When $z = 0$, $\theta = \theta_0$,

$$\frac{df_s(\theta_0)}{d\theta_0} = \left(k_{11}\cos^2\theta_0 + k_{33}\sin^2\theta_0\right)\left(\frac{\partial\theta_p}{\partial z}\right)_0.$$

$$f_s(\theta_0) = \frac{1}{2}A_p\sin^2(\theta_0 - \theta_p) \tag{B-7}$$

The equation (B-7) can be rewritten as

$$\left(\frac{\partial\theta}{\partial z}\right)_0 = \frac{A_p\sin(\theta_0-\theta_p)\cos(\theta_0-\theta_p)}{k_{11}\cos^2\theta_0 + k_{33}\sin^2\theta_0}. \tag{B-8}$$

When $z = d/2$, $\theta = \theta_m$, and $\dfrac{\partial\theta}{\partial z} = 0$,

$$\int_0^{d/2} \left[\left(\left(k_{11} \cos^2 \theta + k_{33} \sin^2 \theta \right) \left(\frac{\partial \theta}{\partial z} \right)^2 - \chi_a H^2 \sin^2 \theta \right) \right] dz = 0 . \tag{B-9}$$

$$\left(\frac{\partial \theta}{\partial z} \right)_0^2 = \frac{\chi_a H^2 (\sin^2 \theta_0 - \sin^2 \theta_m)}{k_{11} \cos^2 \theta_0 + k_{33} \sin^2 \theta_0}$$

$$H = \frac{1}{\sqrt{\chi_a}} \sqrt{\frac{k_{11} \cos^2 \theta_0 + k_{33} \sin^2 \theta_0}{\sin^2 \theta_0 - \sin^2 \theta_m}} \left(\frac{\partial \theta}{\partial z} \right)_0 \tag{B-10}$$

When the applied magnetic field H is larger than the threshold magnetic field H_{th},

$$H = \frac{2}{d} \frac{1}{\sqrt{\chi_a}} \int_{\theta_0}^{\theta_m} \sqrt{\frac{k_{11} \cos^2 \theta + k_{33} \sin^2 \theta}{\sin^2 \theta - \sin^2 \theta}} d\theta . \tag{B-11}$$

By combining Equation (B-10), (B-11), and (B-8), the relationship between θ_0 and θ_m can be figured out.

By fitting the experimental phase difference and the theoretical phase difference, the polar anchoring strength can be determined.
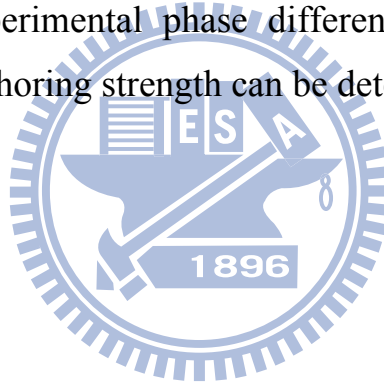
References

[1] D. riviere, Y. Levy, and E. Guyon, "Determination of anchoring energies from surface tilt angle measurements in a nematic liquid crystal," *J. Physique Lett.* **40**, 215 (1979).

[2] S. Naemura, "Measurement of anisotropic interfacial interactions between a nematic liquid crystal and various substrates," *Appl. Phys. Lett.* **33**, 1 (1978).

[3] S. Naemura, "Polar and nonpolar contributions to liquid-crystal orientations on substrates," *J. Appl. Phys.* **51**, 6149 (1980).

[4] K. H. Yang, "On the determination of liquid crystal-to-wall anchoring anisotropy by the surface-plasmon polariton technique," *J. Appl. Phys.* **53**, 6742 (1982).

[5] K. H. Yang, and C. Rosenblatt, "Determination of the anisotropic potential at the nematic liquid crystal-to-wall interface," *Appl. Phys. Lett.* **43**, 62 (1983).
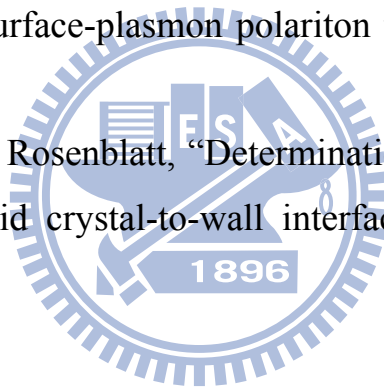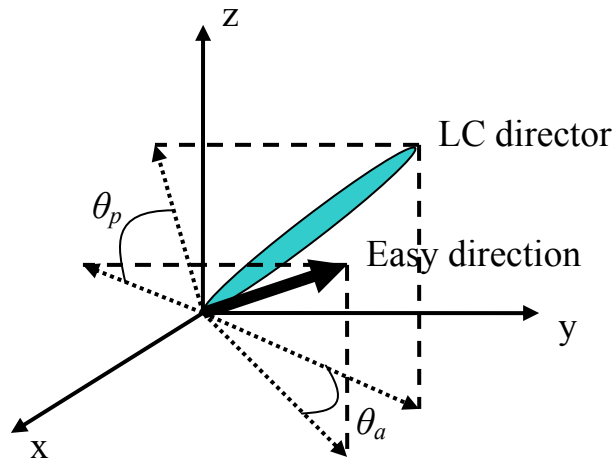
Figures

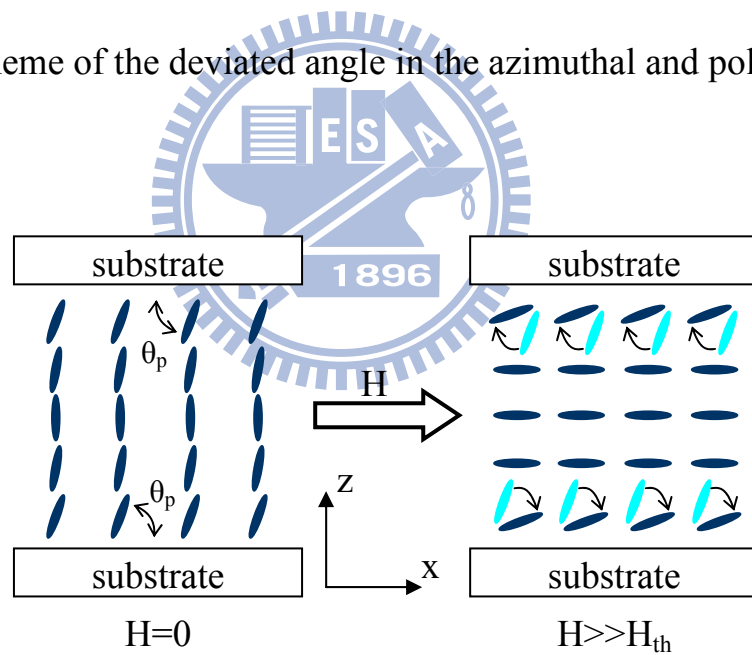Figure B-1 Scheme of the deviated angle in the azimuthal and polar direction.

Figure B-2 Scheme of the liquid crystal distribution in a vertically aligned cell.

Appendix C
The image processing program - ImageJ

C.1 Overview

ImageJ [1] is a powerful Java image processing program. It is developed by National Institutes of Health (NIH), and designed with an open architecture as a freeware. It is available to use in Windows, Mac OS, Mac OS X, and Linux system. ImageJ can easily edit, display, analyze, process, save, and print 8-bit, 16-bit, and 32-bit images. Users can easily extend the functions of ImageJ via Java plugins and recordable maros. Custom acquisition, analysis and image processing plugins can be designed by using ImageJ's built-in editor and a Java compiler. The whole source code of ImageJ can be downloaded from the developer resources section of the ImageJ website. [2]

C.2 The plugins or functions used in this thesis

C.2.1 Threshold (Image->Adjust->Threshold)

By using this function, it is easy to set lower and upper threshold values. Then we can segment the image into features of interest and background. Pixels with brightness values between the lower threshold and the upper threshold are displayed in red. In the threshold window, the upper and lower slider can adjust the minimum and maximum threshold value, respectively. If we hold the "Alt" key down while adjusting the minimum threshold value, it will move a fixed-width thresholding window across the range of gray values. The "Auto" button automatically sets the threshold levels based on an analysis of the histogram of the current image or selection. The "Apply" button sets thresholded pixels to black and all other pixels to white. The "Reset" button disables thresholding and update the histogram. The "B&W" button switches to a mode

where features are displayed in black and background in white. The "Set" button allows user to manually enter new threshold levels into a dialog box. Figure C-1 shows the threshold dialog window and the thresholded image. The red parts are the thresholded parts and the pores of AAO image.

C.2.2 Smooth (Process->Smooth)

The smooth function will blur the active image or selection. This filter replaces each pixel with the average of its 3x3 neighborhood. In this work, we use this function several times to smooth the porous structure and reduce the crack-like structure. Figure C-2 shows the difference before and after smooth treatment. Figure C-2 (a) is the AAO SEM image just after threshold selection. The red parts show the AAO pore structures. Figure C-2 (b) is the same AAO SEM image after 10 times smooth. It clearly shows the porous structures become smoother, and there is less crack-like structure. After smoothing the image, it is easy to use the particle analyzer to get the average pore sizes and the density.

C.2.3 Analyze particles (Analyze->Analyze particles)

By using this command, we easily counts and measures the objects in binary or thresholded images. It works by scanning the image or selection until finding the edge of an object, then outlines the object using the wand tool. This command also measures all objects by using the Measure command, fills it to make it invisible, then resumes scanning until it reaches the end of the image or selection.

The dialog window (Figure C-3) can configure the particle analyzer. If the particles outside the range specified in the "Size" are ignored. If we just enter a single value in size, the particles smaller than that value are ignored. If the particles with circularity values outside the range specified in the "Circularity" are also ignored. The formula for circularity is $4*\pi(\text{area}/\text{perimeter}^2)$. A value of 1.0 indicates a perfect circle. The "Show:" will let user select how to show the

particle analyzer result. "Outlines" opens a window containing numbered outlines of the measured particles. "Masks" displays filled outlines of the measured particles, and "Ellipses" displays the best fit ellipse of each measured particles. Figure C-4 shows the different layout after analyzing particles.

In our AAO image analyzing, we need to check "Display Results" to have the measurements for each particle displayed in the "Results" window, check "Clear Results" to erase any previous measurement results, and check "Summarize" to display the particle count, total particle area, average particle size, and area fraction. Figure C-5 shows the actual AAO SEM image analysis result by using the outlines layout.
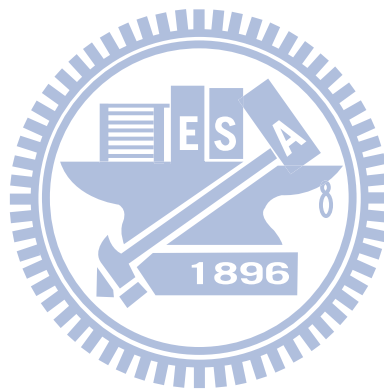
C.3 The algorithm of analysis process

Here is the algorithm of the AAO SEM image analysis process.

```
┌─────────────────────┐
│       Take          │
│  the FESEM image    │
└─────────────────────┘
          │
          ▼
┌─────────────────────┐
│     Threshold       │
│     analyzing       │
└─────────────────────┘
          │
          ▼
┌─────────────────────┐
│      Smooth         │◄──────┐
│  thresholded image  │       │
└─────────────────────┘       │
          │                   │
          ▼                   │
      ◇ Pore structure ◇  No  │
      ◇ clear or not?  ◇──────┘
          │
          │ Yes
          ▼
┌─────────────────────┐
│     Particles       │
│     Analyzing       │
└─────────────────────┘
          │
          ▼
    ╭─────────────────────╮
    │    Pore count,      │
    │  Total pore area,   │
    │  Average pore size  │
    ╰─────────────────────╯
```
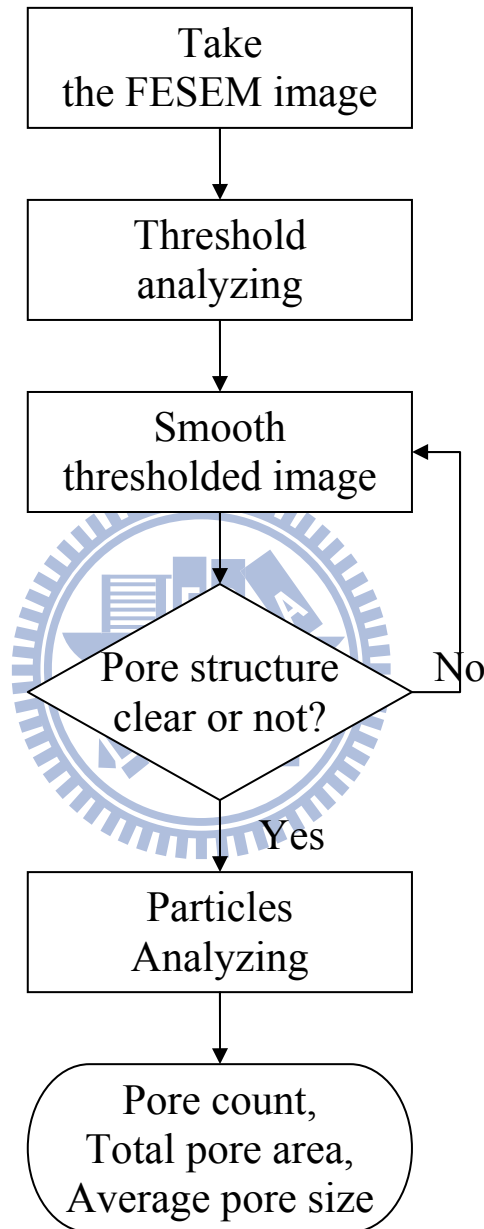
References

[1] ImageJ official website: http://rsbweb.nih.gov/ij/

[2] ImageJ developer resources: http://rsb.info.nih.gov/ij/developer/index.html
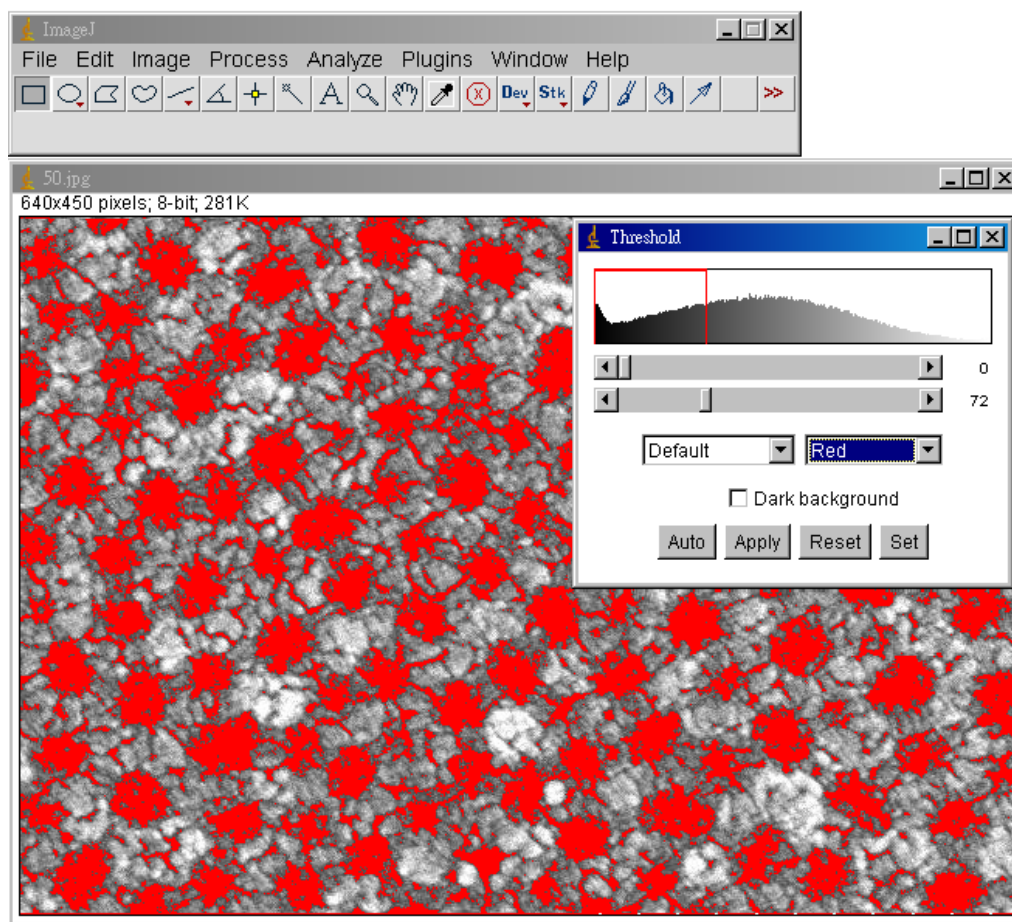
Figures

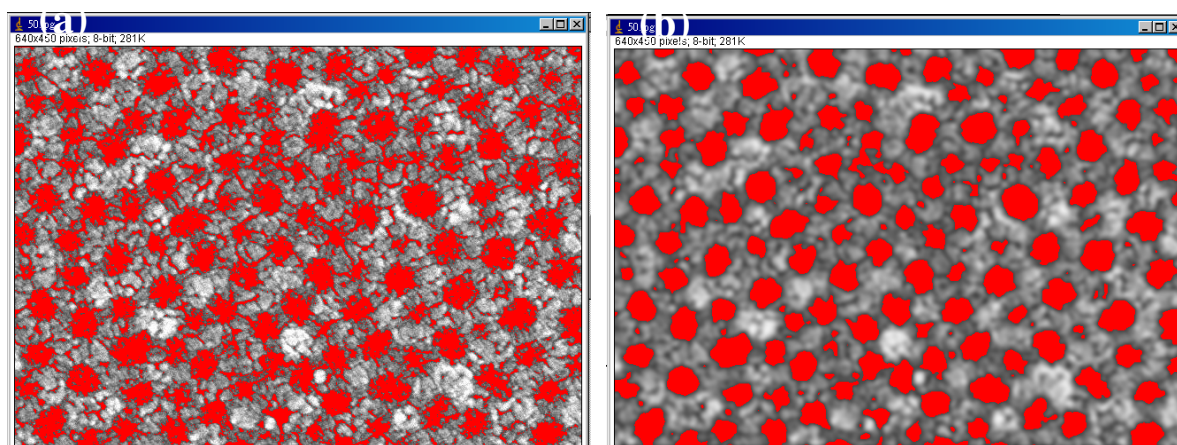Figure C-1 Screenshot is shown the threshold function and the dialog window.

Figure C-2 (a) the AAO SEM image after threshold selection (b) the AAO SEM image after 10 times smooth.
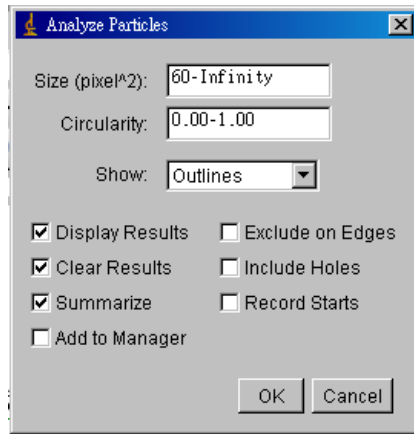
Figure C-3 Dialog window of analyze particles.

Original image   Thresholded using   "Outlines"   "Masks"   "Ellipses"
                  Image>Adjust>Threshold
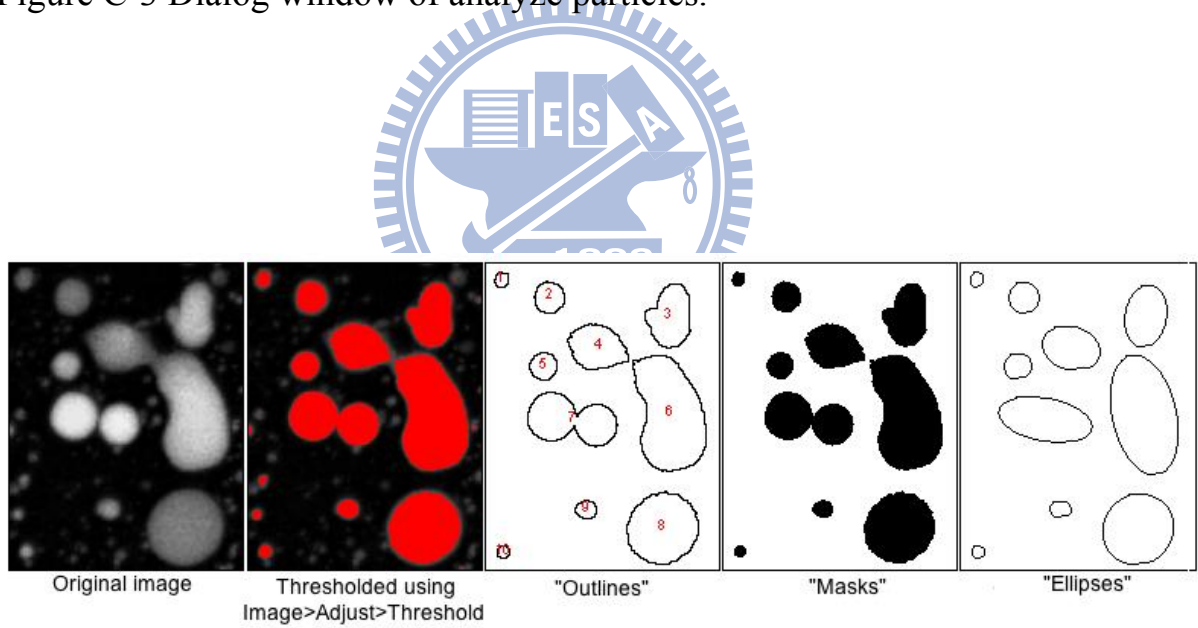
Figure C-4 Different layout after analyzing particles. (The documents of ImageJ)
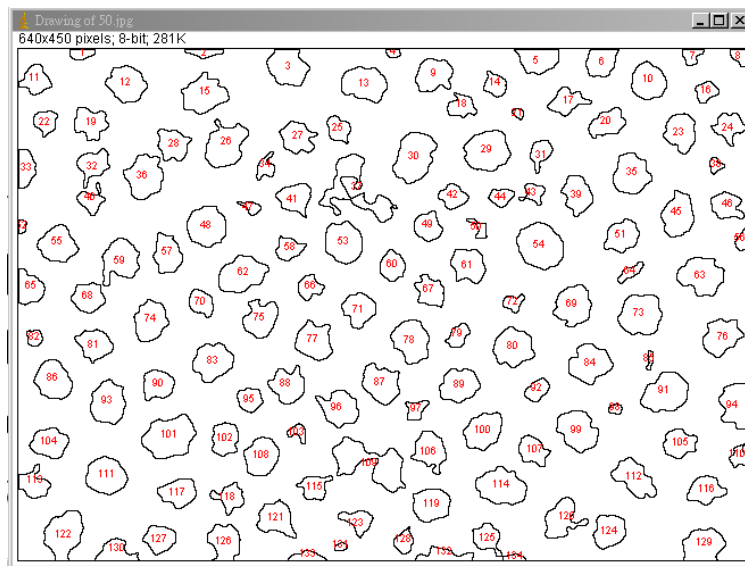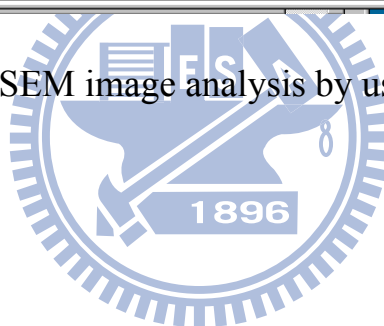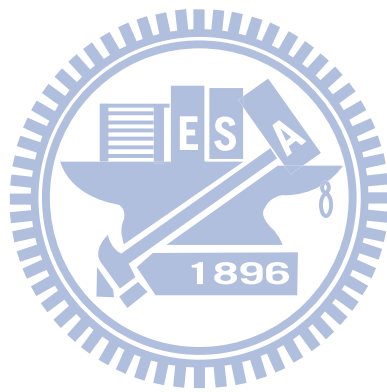
Figure C-5 Actual AAO SEM image analysis by using the outlines layout.

Tsung-Ta Tang

Contact Information:

Phone: 886-3-5131560, 1-800-409-9811 ext. 31560 (calling from USA)

Address: EF553B, Engineering Building VI,

     1001 University Road, Hsinchu, Taiwan 300, ROC

E-mail: tang.eo92g@nctu.edu.tw

Education:

- National Chiao Tung University, Ph.D. in Department of Photonics and Institute of Electro-Optical Engineering

  Thesis: *Study on the Alignment Properties of Liquid Crystalon the Substrate with Anodic Aluminum Oxide Films*.

  Advisor: *Dr. Ci-Ling Pan and Dr. Ru-Pin Pan*

  2003-2009

- National Chiao Tung University, M.Sc. in Department of Electrophysics
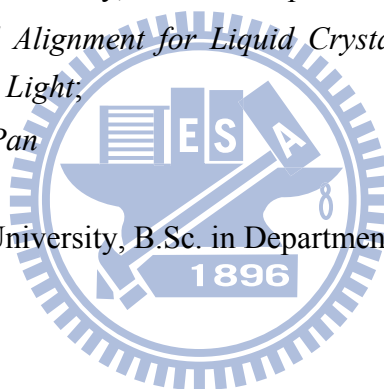
  Thesis: *Photo-induced Alignment for Liquid Crystal with UV-light and Multi-photon Absorption of IR Laser Light*;

  Advisors: *Dr. Ru-Pin Pan*

  2001-2003.

- National Chiao Tung University, B.Sc. in Department of Electrophysics

  1997-2001.

Honors:

- *The first poster award*, 27th Symposium on Spectroscopic Technologies and Surface Sciences, NanTou, Taiwan, July 13-15 (2009)
- *Fellowship (ranked top 3%)*, Institute of Electro-Optical Engineering, National Chiao Tung University, Taiwan, 2003-2004.

Research and Teaching Experience:

- University of California, Berkeley, Department of Physics, Visiting Student, *Shen's Group and Feng's Group*, April 2008-March 2009.
- National Chiao Tung University, Department of Photonics, Research Assistant, *Liquid Crystal Physics Laboratory and Ci-Ling Pan Laboratory*, 2003-2009.
- Tze Chiang Foundation of Science and Technology, Lecturer, *Introduction of Liquid Crystal Display*, 2003-2004.
- National Chiao Tung University, Department of Electrophysics, Teaching Assistant, *Introduction of Liquid Crystal*, 2002-2003.
- National Chiao Tung University, Department of Electrophysics, Research Assistant, *Liquid Crystal Physics Laboratory*, 2001-2002.

Publications:

- **Tsung-Ta Tang**, Cheng-Ying Kuo, Ru-Pin Pan, Jia-Min Shieh, and Ci-Ling Pan," Strong Vertical Alignment of Liquid Crystal on Porous Anodic Aluminum Oxide Film", *IEEE J. Dis. Tech.* **5**, 350 (2009).
- Ching-Wei Chen, **Tsung-Ta Tang**, Sung-Hui Lin, Jung Y. Huang, Chen-Shiung Chang, Pei-Kang Chung, Shun-Tung Yen, and Ci-Ling Pan, "Optical properties and potential applications of ε-GaSe at terahertz frequencies", *J. Opt. Soc. Am. B* **26**, A58 (2009).
- Yuanbo Zhang, **Tsung-Ta Tang**, Caglar Girit, Zhao Hao, Michael C. Martin, Alex Zettl1, Michael F. Crommie, Y. Ron Shen, and Feng Wang, "Direct observation of a widely tunable bandgap in bilayer graphene", *Nature* **459**, 820 (2009).
- **Tsung-Ta Tang**, Ru-Pin Pan, Yi-Chao Wang, Ci-Ling Pan, "THz time-domain spectroscopic studies of a ferroelectric liquid crystal in the SmA* and SmC* phases", *Ferroelectrics* **364**, 72 (2008).
- Wei-Jan Chen, Zhi-Ming Hsieh, Shu Wei Huang, Hao-Yu Su, **Tsung-Ta Tang**, Ru-Pin Chao, Ci-Ling Pan, Chao-Kuei Lee, and A. H. Kung, "Sub-Single-Cycle Optical Pulse Train with Constant Carrier Envelope Phase", *Phys. Rev. Lett.* **100**, 163906 (2008).
- **Tsung-Ta Tang**, Hsin-Ying Wu, Chia-Jen Lin, Ru-Pin Pan, " Optical method for measuring the azimuthal anchoring strength of liquid crystals using pitch values determined in imperfect samples", *J. Appl. Phys.* **102**, 063108 (2007).
- **Tsung-Ta Tang**, Hsin-Ying Wu, Chia-Jen Lin, and Ru-Pin Pan, "A simple method of determining the pitch of a chiral nematic liquid crystal", *Mol. Cryst. Lig. Cryst.,* **478**, 143 (2007).
- Hsin-Ying Wu, **Tsung-Ta Tang**, Chih-Chieh Wang, Ru-Pin Pan, Shao-Ju Chang, and Jenn-Chang Hwang, "Controllable alignment modes of nematic liquid crystal on argon ion beam bombarded polyimide films", *Mol. Cryst. Liq. Cryst.* **475**, 45 (2007).
- Hsin-Ying Wu, Cho-Fan Hsieh, **Tsung-Ta Tang**, Ru-Pin Pan, and Ci-Ling Pan, "Electrically Tunable Room-Temperature Liquid Crystal Terahertz Phase Shifter", *IEEE Photon. Technol. Lett.,* **18**, 1488 (2006).
- Cho-Fan Hsieh, **Tsung-Ta Tang**, Hung-Lung Chen, Ru-Pin Pan, and Ci-Ling Pan, "Voltage-controlled liquid crystal terahertz phase shifter and quarter wave plate." *Opt. Lett.,* **31**, 1112 (2006).

Conference Presentations:

- Yuanbo Zhang, **Tsung-Ta Tang**, Caglar Girit, Zhao Hao, Michael C. Martin, Alex Zettl, Michael F. Crommie, Y. Ron Shen and Feng Wang, "Direct Observation of a Widely Tunable Bandgap in Bilayer Graphene", 27th Symposium on Spectroscopic Technologies and Surface Sciences, NanTou, Taiwan, July 13-15 (2009).
- **Tsung-Ta Tang**, Ru-Pin Pan, Yi-Chao Wang, Ci-Ling Pan, "THz time-domain spectroscopic studies of a ferroelectric liquid crystal in the SmA* and SmC* phases", 11th Ferroelectric Liquid Crystal Conference, Sapporo, Hokkaido, Japan, September 3-8 (2007).
- Cho-Fan Hsieh, Hsin-Ying Wu, Ru-Pin Pan, **Tsung-Ta Tang** and Ci-Ling Pan, "Tunable 2π Terahertz Phase Shifter Using a Sandwiched Nematic Liquid Crystal Cell", 1st Asian-Pacific THz Photonics Workshop, Hsin-Chu, Taiwan, 14 December

(2006).

- **Tsung-Ta Tang**, Hsin-Ying Wu, Chia-Jen Lin, Ru-Pin Pan, "A simple method to determine the pitch of chiral nematic liquid crystal", 21st International Liquid Crystal Conference, Keystone, Colorado, U.S.A., July 2-7, OPTIP-2 (2006).
- Cho-Fan Hsieh, Ru-Pin Pan, Hsin-Ying Wu, **Tsung-Ta Tang**, Ci-Ling Pan, "Electrically controlled liquid crystal 2π terahertz phase shifter", 21st International Liquid Crystal Conference, Keystone, Colorado, U.S.A., July 2-7, OPTIP-42 (2006)
- Hsin-Ying Wu, **Tsung-Ta Tang**, Chih-Chieh Wang, Ru-Pin Pan, Shao-Ju Chang, and Jenn-Chang Hwang, "Controllable alignment modes of nematic liquid crystal on argon ion beam bombarded polyimide films", 21st International Liquid Crystal Conference, Keystone, Colorado, U.S.A., July 2-7, ALGNP-26 (2006)
- **Tsung-Ta Tang**, Ru-Pin Pan, Alexei K. Zaitsev, Ci-Ling Pan, and L.-C. Chien, "Photon-Induced Alignment for Liquid Crystal with UV-light and Two-Photon Absorption of IR Laser Light", The International Display Manufacturing Conference 2003 (IDMC'03), Taipei, Taiwan, February 18-21, pp.673-675 (2003)
- **Tsung-Ta Tang**, Hsin-Ying Wu, Chia-Jen Lin, and Ru-Pin Pan, "Precision improvement for azimuthal anchoring strength determination of liquid crystal surface", Optics and Photonics Taiwan, Taiwan, GO-22, December 15-16 (2006).
- Cho-Fan Hsieh, **Tsung-Ta Tang**, Hung-Lung Chen, Ru-Pin Pan and Ci-Ling Pan, "Voltage Controlled Liquid-Crystal-Based Quarter Wave Plate for THz wave", Optics and Photonics Taiwan, Taiwan, December 30 (2005).
- Cho-Fan Hsieh, **Tsung-Ta Tang**, Hung-Lung Chen, Ru-Pin Pan and Ci-Ling Pan, "Electrically Controlled Liquid-Crystal-Based Terahertz Phase Shifter and Quarter Wave Plate", The Annual Meeting of ROC Taiwan Liquid Crystal Society, Hsinchu, Taiwan, December 30 (2005).
- Chia-Jen Lin, **Tsung-Ta Tang**, and Ru-Pin Pan, "Photo-induced Alignment of Polyimide with UV-Laser and Xenon Arc Lamp", The Annual Meeting of The Physics Society of Republic of China, Kaohsiung, February 1-3 (2005).
- Chia-Jen Lin, **Tsung-Ta Tang**, and Ru-Pin Pan, "Photo-induced Alignment of Low-Molecular-Weight Photo-Cross-Linkable Composites with UV-light", The Annual Meeting of The Physics Society of Republic of China, Taiwan, February (2004).
- Chia-Jen Lin, **Tsung-Ta Tang**, and Ru-Pin Pan, "Photo-induced Alignment of Low-Molecular-Weight Photo-Cross-Linkable Composites with UV-light", The Annual Meeting of Taiwan Liquid Crystal Society, Hsin-chu, Taiwan, December 19 (2003).
- 郭政穎, 湯宗達, 林家任, 趙如蘋, "陽極處理氧化鋁薄膜基板對液晶配向之研究", 2006 中國液態晶體學會年會暨研討會, PP-12, Deccember 22 (2006).
- 張佳瑩, 湯宗達, 林家任, 趙如蘋, "摩刷配向與紫外光配向之聚亞醯胺薄膜其相位延遲研究及與表面錨定強度之關係", 2006 中國液態晶體學會年會暨研討會, PP-13, December 22 (2006).